

ABSTRACT

LOSEGO, MARK DANIEL. *The Chemical Solution Deposition of Lead Zirconate Titanate (PZT) Thin Films Directly on Copper Surfaces.* (Advisor: Jon-Paul Maria).

Traditionally, multifunctional complex oxide thin films, like the common ferroelectric materials lead zirconate titanate (PZT) and barium titanate (BaTiO_3) have been limited to substrates with noble metal or conductive oxide bottom electrodes. This constraint originates from the vulnerability of base metals to oxidation when traditional ceramic processing parameters—high temperatures and oxygen rich atmospheres—are used to synthesize ferroelectric films. With current technology, ferroelectric thin films have demonstrated vast applicability as tunable capacitors, sensors, piezoelectric actuators, and non-volatile memories. By integrating ferroelectric thin films with base metals, the barrier to mass production is lowered through reduced expense and simplified electrode patternability. Moreover, base metals have higher conductivities and offer the possibility for increased functionality by incorporation of ferromagnetic or shape memory alloys.

Recent research efforts have adapted 1970s thick film multilayer capacitor technology to process thin films of the $(\text{Ba,Sr})\text{TiO}_3$ family directly on nickel and copper substrates. This methodology relies on processing these materials within a window of temperature and oxygen partial pressure ($p\text{O}_2$) that affords thermodynamic equilibrium between the oxidized perovskite film and unoxidized base metal substrate. Although the family of $(\text{Ba,Sr})\text{TiO}_3$ materials offers excellent dielectric properties, the material PZT

could provide a complementary set of functionality to satisfy applications that require an enhanced ferroelectric or piezoelectric response. Unfortunately, fundamental materials differences—particularly PbO volatility and a narrow thermodynamic stability window—make equilibrium processing impractical for PZT / base metal systems.

In this thesis, integration of PZT directly on copper surfaces via a chemical solution deposition (CSD) route is investigated. Using this platform a new methodology is developed for achieving perovskite / base metal compatibility. Unlike the traditional equilibrium approach, this new method focuses on using a knowledge of sol-gel science to design a process window that is compatible with the copper substrate while maintaining the integrity of the PZT film. Using this approach, the chelating ligands (organic molecules that impart stability to the metal cations in solution) have been identified as a critical process parameter. If these chelating species cannot provide sufficient gel consolidation and volatilization prior to crystallization within a processing window compatible with the copper substrate, then various complications can result such as substrate oxidation, non-perovskite phase development, or film cracking.

By proper chelating agent selection and a unique composite gel architecture, this thesis demonstrates that PZT films can be processed directly on copper substrates with dielectric and ferroelectric properties comparable to films deposited on conventional platinized silicon. Dielectric constants in excess of 800 with $\tan\delta$ values below 0.02 have been achieved as well as remanent polarization of $33 \mu\text{C}/\text{cm}^2$. C-V and P-E loops exhibit classical ferroelectric shapes with well-saturated intrinsic regimes. Electrical fatigue experiments show a classic response with loss of P-E loop squareness and a recoverable

remanent polarization upon annealing above the Curie point. Hence, this work demonstrates a methodology for obtaining PZT thin films on copper substrates with remarkable dielectric and ferroelectric properties that are competitive with current noble metal / conductive oxide bottom metal electrode technologies.

**THE CHEMICAL SOLUTION DEPOSITION OF LEAD ZIRCONATE TITANATE
(PZT) THIN FILMS DIRECTLY ON COPPER SURFACES**

by

MARK DANIEL LOSEGO

Submitted to the Graduate Faculty of
North Carolina State University
in partial fulfillment of the
requirements for the Degree of
Master of Science

MATERIALS SCIENCE AND ENGINEERING

Raleigh

2005

APPROVED BY:



Jon-Paul Maria
Assistant Professor of Materials Science and Engineering
Chair of Advisory Committee



Mark Johnson
Assistant Professor of Materials Science and Engineering



Gerald Lucovsky
Professor of Physics

Vita

Mark Daniel Losego was born on December 16, 1980. He grew up in the small town of Heidelberg, Pennsylvania, a suburb of Pittsburgh. Devoted to French fry laden sandwiches, Terrible Towels, and Heinz Ketchup, Mark was reluctant to leave his Burgh roots—but scientific curiosity soon got the best of him. In 1999, Mark graduated from Chartiers Valley School District as valedictorian of his high school class. Leaving his fellow classmates with the quote “Suck it up and tough it out to be the best you can,” Mark ventured to Happy Valley to pursue a Bachelor of Science degree in Materials Science and Engineering with an option in Electronic and Photonic Materials. During his four years at Penn State, Mark did some work, made some friends, and learned to bleed blue and white. In 2003, Mark completed his B. S. thesis entitled “The Mist Deposition of Micron-Thick Lead Zirconate Titanate Sol-Gel Films on Silicon and Ceramic Substrates” and graduated with honors as Student Marshal of the College of Earth and Mineral Sciences. Following the advise of his friend and mentor, Susan Trolier-McKinstry, Mark traveled to North Carolina State University to pursue graduate studies under the direction of Jon-Paul Maria, director of the Electroceramic Thin Film Group. Along with his ever-deepening fascination for ferroelectric materials, Mark also brought a National Science Foundation Graduate Research Fellowship. In 2005, Mark earned his Master of Science degree in Materials Science and Engineering at North Carolina State University. Afterwards, he remained with the Electroceramic Thin Film Group to pursue his Ph. D. degree, continuing to investigate the compatibility between functional oxide films and unconventional substrate materials.

Acknowledgments

My most sincere gratitude belongs to Professor Jon-Paul Maria for his continuous support and advice in my research efforts; without his guidance I would still be mapping out all of the process parameters of water thermolysis...in triplicate. Moreover, besides expanding my breadth of ferroelectric knowledge, Jon-Paul has made working at NC State and living in Raleigh a true pleasure.

I would also like to express my appreciation to the rest of the Electroceramic Thin Film Group including Brian Laughlin, Dipankar Ghosh, and Spalding Craft for their daily help and sincere friendship. Special thanks goes to Jon Ihlefeld for his valued input and continual patience, especially with my incessant ranting of sol-gel theories.

I'd also like to acknowledge Leslie Jimison, who began investigating PZT on copper in 2003 and helped establish the scientific kernel and intrigue for completing this current work. Thanks goes to Tom Blair for helping with collecting the PFM data for this study. Also, I would be remiss not to recognize Edna Deas for her persistent help in overcoming the bureaucracy that impeded my completion of this M. S. degree en route to my Ph. D. I also appreciate the time and efforts of my other committee members, Dr. Gerry Lucovsky and Dr. Mark Johnson.

A special acknowledgment is extended to Dr. Robert Schwartz for his detailed and exquisitely written scientific papers on the theory and implementation of CSD perovskite thin film processing. Without the guidance of this previous work, much of what has been accomplished in this thesis would not have been possible.

Finally, I would like to thank my family, especially Mom, Dad, my sister Rachel, and my girlfriend Jessica, for their continual love and support as well as their forbearance of my scientific babble. Without this link to family, I would become totally consumed by science, which would be a sad life indeed.

This material is based upon work supported under a National Science Foundation Graduate Research Fellowship.

Table of Contents

List of Figures	viii
List of Tables.....	xiii
List of Common Abbreviations.....	xiv
Preface.....	xvi
1. An Introduction to Ferroelectric Materials and Their Properties	1
1.1 A Historical Perspective of Ferroelectric Materials.....	1
1.2 A Description of Ferroelectricity	2
1.2.1 A Description of the Ferroelectric Phase Transition.....	4
1.2.2 Ferroelectricity in Perovskite Crystals.....	5
1.3 Ferroelectric Domains.....	7
1.3.1 Domain Walls.....	9
1.3.2 The Extrinsic Contribution to Ferroelectric Properties.....	10
1.4 Ferroelectrics for Commercial Applications.....	12
1.4.1 Applications of Ferroelectrics	12
1.4.2 PZT and BaTiO ₃ – Complementary Ferroelectrics	14
1.5 PZT Thin Films.....	15
1.5.1 Effects of Stress in PZT Thin Films.....	17
1.5.2 Effects of Crystalline Orientation on PZT Thin Films.....	18
1.6 Ferroelectric Aging.....	19
1.7 Ferroelectric Fatigue.....	22
1.7.1 General Discussion of Fatigue Mechanisms	24
1.7.2 Fatigue – Domain Wall Pinning Hypothesis.....	25
1.7.3 Fatigue – Seed Inhibition Hypothesis	26
1.8 Oxide Dielectric / Base Metal Electrode Compatibility.....	29
1.8.1 (Ba,Sr)TiO ₃ Thin Films on Base Metal Substrates	31
1.8.2 PZT Thin Films on Base Metal Substrates.....	33
1.9 Statement of Purpose.....	35

2. A Review of Chemical Solution Deposited Ceramic Thin Films	37
2.1 A General Outline for Processing CSD Thin Films	37
2.2 Solution Chemistry.....	38
2.2.1 Precursors and Ligands	39
2.2.2 Methods for Solution Preparation	41
2.3 Film Deposition.....	44
2.4 Gellation	45
2.5 Drying of Gels.....	47
2.5.1 Drying Stresses and Cracking in Bulk Sol-Gel Systems.....	49
2.5.2 Drying in Thin Film Sol-Gel Systems.....	50
2.6 Organic Removal from Gelled Thin Films.....	52
2.7 Crystallization of Gels.....	54
2.7.1 The Application of Classical Nucleation Theory to Sol-Gel Systems	55
2.7.2 Competition Between Sintering and Crystallization	56
2.8 Examples of Applying Sol-Gel Science to Real Thin Film Systems	58
2.8.1 Influence of Precursor Chemistry on ZrO ₂ and TiO ₂ Films.....	59
2.8.2 Densification vs. Crystallization Kinetics in TiO ₂ Films.....	60
2.9 The Chemical Solution Deposition of PZT Thin Films	61
2.9.1 Nucleation Behavior in CSD PZT Films.....	62
2.9.2 Evolution of the Perovskite Structure in CSD PZT Films	63
3. Investigation of Organic Extraction in CSD PZT Films on Copper Substrates	66
3.1 Solution Preparation.....	66
3.1.1 Alkanolamine Chelated PZT Solution	66
3.1.2 Acetylacetone (Acac) Chelated PZT Solution	67
3.2 Procedures for PZT Thin Film Preparation.....	68
3.3 Organic Removal in Dry Atmospheres	70

3.3.1 Organic Removal in Air	70
3.3.2 Organic Removal in Nitrogen	71
3.4 Water Vapor Hydrolysis of EC Derived PZT Films	76
3.4.1 Previous Research on Water Vapor Thermolysis.....	76
3.4.2 Effects of WVT Temperature and Crystallization Atmosphere.....	76
3.4.3 Effects of Oxygen Partial Pressure on Crystallization Behavior	80
3.4.4 Dependence on Solution Molarity.....	82
3.4.5 Improved Phase Assemblage with Sample Containment During Crystallization	82
3.4.6 Implications of WVT Investigation.....	84
3.5 Implementation of Acac Solution Chemistry	85
3.5.1 Phase Analysis of PZT Films Derived from Acac Solution.....	85
3.5.2 Electrical Data from Acac Derived PZT Films on Copper Foils	89
3.5.3 Implications of Acac Solution Chemistry Investigation	90
4. Development of a CSD Process for Synthesizing Device Quality PZT Films on Copper Surfaces	92
4.1 The Inverted Mixing Order PZT Solution Chemistry.....	92
4.1.1 Previous Characterization of IMO Derived PZT Thin Films.....	92
4.1.2 IMO Solution Preparation	95
4.2 Procedures for PZT Thin Film Preparation.....	96
4.3 Investigation of Process Parameters.....	97
4.3.1 Drying Temperature	97
4.3.2 Crystallization Atmosphere.....	98
4.3.3 Investigation of Thermolysis Conditions	102
4.4 The 2 + 3 Composite Gel Architecture	104
4.4.1 Implementation of 2 + 3 Method.....	105
4.4.2 Electrical Data from 2 + 3 Processed PZT Films on Copper Foils	108
4.4.3 Reproducibility and Attempts to Expand Processing Window	111
4.5 Incorporation of Acac into IMO Solutions	114
4.5.1 Samples Prepared for Acac Investigation	114
4.5.2 Microstructural Comparison	115
4.5.3 Dielectric Comparison.....	118
4.5.4 Ferroelectric Comparison.....	120

4.5.5 Investigation of Leakage Current in Acac-Modified PZT Films on Copper	121
4.5.6 Investigation of Ferroelectric Fatigue in Acac-Modified PZT Films on Copper	122
4.6 Evaluation of Crystallographic Orientation, Film Stresses, and Domain Structure in PZT Films	125
4.6.1 Texturing of PZT Films Deposited on Copper Foils.....	125
4.6.2 Existence of Stress in PZT Films Deposited on Copper Foils	126
4.6.3 Domain Structure in PZT Films Deposited on Copper Foils	127
4.7 Hypotheses for the Success of the 2 + 3 Layer Process	129
4.7.1 Re-evaluating Oxidation During Crystallization.....	129
4.7.2 Investigation of the 2 + 3 Process's Success in Avoiding Copper Oxidation	130
4.7.3 Discussion of Hypotheses for Cu ₂ O Reduction in 2 + 3 Layer Processed Films.....	133
5. Conclusions and Future Work.....	134
5.1 Conclusions	134
5.1.1 Investigations of Organic Removal.....	134
5.1.2 Technological Importance of PZT Thin Films on Copper.....	135
5.2 Possibilities for Future Investigations	136
6. Appendix	138
6.1 Procedures for Data Collection	138
6.2 Powder Diffraction Cards.....	139
6.3 Pb-Cu Phase Diagram	140
7. References	141

List of Figures

Chapter 1

FIG 1-1: Depiction of the Hysteretic Polarization Response in Ferroelectric Materials.....	3
FIG 1-2: Soft Mode Description of the Ferroelectric Phase Transition.....	5
FIG 1-3: Illustration of the Perovskite Unit Cell.....	6
FIG 1-4: Formation of 180° Ferroelectric Domain Walls.....	9
FIG 1-5: Strain Energy Relief by 90° Domain Wall Motion.....	10
FIG 1-6: Illustration of Dielectric Tunability in Ferroelectric Materials.....	11
FIG 1-7: Phase Diagram of the PbZrO ₃ / PbTiO ₃ Solid Solution System.....	16
FIG 1-8: Illustration of Stress Induced Domain Structure in PZT Thin Films.....	18
FIG 1-9: Aging in Poled Ferroelectric Materials.....	21
FIG 1-10: Effect of Aging in Unpoled Ferroelectrics.....	22
FIG 1-11: Change in P-E Response as a Result of Ferroelectric Fatigue.....	23
FIG 1-12: Domain Wall Pinning Model of Ferroelectric Fatigue.....	25
FIG 1-13: Seed Inhibition Model of Ferroelectric Fatigue.....	26
FIG 1-14: AFM Assisted Piezo-Response Images of a Fatigued PZT Film.....	27
FIG 1-15: Comparison of Fatigued Domain Structure for Two Different Models.....	28
FIG 1-16: Phase Diagram Showing Elemental Metal / Metal Oxide Stability as a Function of Temperature and Oxygen Partial Pressure.....	31

Chapter 2

FIG 2-1: Illustration of Metal Carboxylate and Metal Alkoxide Species	40
FIG 2-2: Depiction of a Bridging Ligand Versus a Non-Bridging Ligand	41
FIG 2-3: Illustration of the Driving Force for Gel-to-Ceramic Conversion as a Function of Temperature	54
FIG 2-4: Representative Plot Combining TTT Diagrams with Sintering Kinetics to Optimize Sol-gel Annealing Conditions	58
FIG 2-5: Effect of Heating Rate on the Densification Behavior of Sol-Gel TiO ₂ Films	61

Chapter 3

FIG 3-1: Summary of Process Parameters Explored in Chapter 3	69
FIG 3-2: Phase Evolution for EC Air Pyrolyzed PZT Films on Copper	71
FIG 3-3: Phase Evolution in EC Derived Film During N ₂ Thermolysis	72
FIG 3-4: XRD of Crystallized EC Derived, N ₂ Thermolyzed PZT Films	72
FIG 3-5: Phase Evolution in EC Derived 300°C Dried PZT Films	73
FIG 3-6: Micrograph of 4-Layer EC N ₂ Thermolyzed Sample	74
FIG 3-7: Micrographs of Crystallized EC Samples Processed in Dry Conditions	75
FIG 3-8: XRD Analysis of Varying WVT Temperatures	77
FIG 3-9: Effect of Crystallization Atmosphere on WVT PZT	77
FIG 3-10: Micrograph of EC WVT Sample	78
FIG 3-11: Micrograph of WVT PZT Film Crystallized in Water Vapor	79
FIG 3-12: Micrograph of WVT PZT Film Crystallized in N ₂	79
FIG 3-13: Effect of WVT Condition on PZT Crystallization in Vacuum	81

FIG 3-14: Impact of Crystallization pO_2 on WVT PZT Films.....	81
FIG 3-15: Crystallization Behavior of 0.1 M EC Solution with 15 min WVT	83
FIG 3-16: Crystallization Behavior of 0.1 M EC Solution with 7.5 min WVT.....	83
FIG 3-17: Effect of Sample Containment on Perovskite Crystallization.....	84
FIG 3-18: XRD Analysis of Thermolysis Conditions for Acac Solution	86
FIG 3-19: Acac Solution Crystallization Behavior for WVT and 300°C Dried Films.....	87
FIG 3-20: Micrograph of WVT Acac Derived PZT Film Annealed in N_2	87
FIG 3-21: Micrograph of 300°C Dried Acac Derived PZT Film.....	88
FIG 3-22: Effect of pO_2 and Drying Temperature on Acac Derived PZT Films.....	88
FIG 3-23: Dielectric Tunability Data for Acac Solution Derived PZT Film on Cu	89

Chapter 4

FIG 4-1: Comparison of SPA and IMO Solution Preparation Procedures	93
FIG 4-2: XRD Analysis of Substrate Oxidation During Drying of IMO Derived Gels.....	98
FIG 4-3: XRD Analysis of IMO Drying Series Crystallized in Nitrogen.....	99
FIG 4-4: XRD Analysis of IMO Drying Series Crystallized in $pO_2 = 1.3 \times 10^{-14}$ Torr	99
FIG 4-5: XRD Analysis of IMO Drying Series Crystallized in Forming Gas.....	100
FIG 4-6: Micrographs of PZT Films Dried at Various Temperature and Crystallized in Nitrogen	101
FIG 4-7: Micrograph of PZT Film Crystallized in Forming Gas.....	102
FIG 4-8: XRD Comparison of PZT on Cu Samples Thermolyzed in N_2 and 1% H_2 / N_2	103

FIG 4-9: Micrograph of Cracking in Completely Thermolyzed IMO PZT Films.....	104
FIG 4-10: XRD Comparison of 1 + 4 Process to 2 + 3 Process.....	106
FIG 4-11: Phase Development in EC Derived Films Using the 2 + 3 Methodology	107
FIG 4-12: Micrograph of 2 + 3 Processed PZT Film Using the EC Solution Chemistry.....	107
FIG 4-13: Dielectric Tunability of a 2 + 3 Layer Processed IMO PZT Film on Copper.....	109
FIG 4-14: Dielectric Dispersion of a 2 + 3 Layer Processed IMO PZT Film on Copper.....	109
FIG 4-15: Ferroelectric Response of a 2 + 3 Layer Processed IMO PZT Film on Copper.....	110
FIG 4-16: Comparison of Ferroelectric Response from PZT Films Prepared on Cu and Si	111
FIG 4-17: Ferroelectric Response Comparison Showing Reproducibility of 2 + 3 Layer Process	112
FIG 4-18: Photograph Comparing Gel/Cu Appearance After Initial Drying Step.....	113
FIG 4-19: XRD Comparison of PZT Films Prepared from a Fresh IMO Solution and a 30-Day Old Acac-Chelated Solution	115
FIG 4-20: SEM Image of IMO Derived PZT Film	116
FIG 4-21: AFM Images of IMO and Acac-Modified PZT Films	116
FIG 4-22: AFM Images Acac-Modified PZT Film Crystallized at 700°C.....	117
FIG 4-23: AFM Images Illustrating Micro-cracking in PZT Films.....	118
FIG 4-24: Dielectric Tunability of PZT Film on Cu from 1-Day Old IMO Solution....	119
FIG 4-25: Dielectric Tunability of PZT Film on Cu from Aged IMO Solution with Acac Chelation	119

FIG 4-26: Dielectric Tunability of PZT Films on Cu Crystallized at 700°C.....	120
FIG 4-27: Comparison of Ferroelectric Response from PZT Films Prepared with IMO and Acac Modified Solution Chemistries	121
FIG 4-28: Leakage Current Measurement of PZT Film on Copper Foil	122
FIG 4-29: Ferroelectric Fatigue Characteristics of PZT Film Prepared on Copper.....	123
FIG 4-30: P-E Response of PZT Film on Copper as Fatiguing Occurs.....	123
FIG 4-31: Comparison of Fatigued and Recovered Ferroelectric Responses for a PZT Film on Copper	124
FIG 4-32: Dielectric Response of PZT Film After Fatiguing and Recovery Anneal.....	124
FIG 4-33: XRD Evidence for the Texturing of PZT Films on Copper Foils.....	126
FIG 4-34: AFM and PFM Images Illustrating the Domain Structure in PZT Films Prepared on Copper Foils.....	128
FIG 4-35: Evaluation of Copper Oxidation During Crystallization of Dried Films	130
FIG 4-36: Phase Evolution in 2 + 3 Layer Process Using a 250°C Dry	131
FIG 4-37: Phase Evolution in 2 + 3 Layer Process Using a 300°C Dry	131
FIG 4-38: Attempts to Form Intermediate During Thermolysis of IMO Films.....	132

Chapter 6

FIG 6-1: Powder Diffraction Cards Used in Phase Identification.....	139
FIG 6-2: Cu-Pb Binary Phase Diagram.....	140

List of Tables

Table 1-1: Property Comparison for BaTiO ₃ and Pb(Zr,Ti)O ₃ Ceramics.....	15
Table 2-1: Requirements for Successfully Synthesizing Thin Films by a Chemical Solution Deposition Process.....	39

List of Common Abbreviations

2-MOE.....	2-Methoxyethanol
Acac.....	Acetylacetone / Acetylacetonate (2, 4-pentanedione)
AFM	Atomic Force Microscopy
CSD	Chemical Solution Deposition
EC	Ethanolamine Chelated (Solution Chemistry)
E_c	Coercive Field
ϵ	Relative Permittivity
HOAc	Acetic Acid
IMO	Inverted Mixing Order (Solution Chemistry)
MeOH.....	Methanol
MOD.....	Metalorganic Decomposition
PFM.....	Piezo-response Force Microscopy
pO_2	Oxygen Partial Pressure

P_r	Remanent Polarization
P_s	Saturation Polarization
Py.....	Pyrochlore
PZT	Lead Zirconate Titanate
SEM.....	Scanning Electron Microscopy
SPA.....	Sequential Precursor Addition (Solution Chemistry)
T_c	Curie Point
$\tan \delta$	Dielectric Loss
XRD	X-ray Diffraction

Preface

This thesis is a tribute to those who still believe in the possibility of idealized scientific research. Regrettably, today's research pursuits are too often dictated by the current "hot topic" or the desires of funding sources. Three factors allowed me to escape these traps: (1) we lost the funding for my original project, (2) I was able to fall back on my NSF Fellowship for funding (for this luxury I am eternally grateful to the National Science Foundation), and (3) I worked in a group that encourages and supports research for the sake of scientific curiosity. This latter point is why this research has become a thesis rather than another lackluster journal article. At first, my endeavors to put PZT on nickel / copper were simply motivated by completing some unfinished previous experiments and writing a short journal article about the results. However, as advances were made, Jon-Paul would allow me another two weeks of research—to satisfy our scientific curiosities. These advances continued and two week extensions were added until I had worked on this project for an entire summer and reached the basic scientific conclusions presented in this manuscript. It was an exciting time full of frequent scientific breakthroughs, and the research was truly enjoyable. I can only hope that others will have a similar opportunity in their scientific careers—the pleasure of undertaking a research project of your own interest that is simply motivated by the desire to make new science.

1. An Introduction to Ferroelectric Materials and Their Properties

Central to the field of materials science is the intimate relationships between the processing, structure, and properties of materials. Ferroelectric materials represent a classical example of structure-property relationships. In this thesis, processing is explored as a means to control the structure of a materials system. Thus, an understanding of processing-structure relationships will be a principal theme. This first chapter sets the groundwork for understanding process-structure-property relationships in ferroelectric materials.

1.1 A Historical Perspective of Ferroelectric Materials:

Ferroelectricity was first experimentally identified in Rochelle salt ($\text{KNaC}_4\text{H}_4\text{O}_6 \cdot 4\text{H}_2\text{O}$) by Joseph Valasek in 1921 [1]. Rochelle salt was first prepared by Elie Seignette nearly 300 years earlier in La Rochelle, France and had become known as Seignette salt in Europe. Consequently, the term Seignette-electricity has also been used to describe ferroelectricity [2, 3]. Although the ease in preparing single crystals of Rochelle salt rendered it initially interesting to study, its water solubility made it technologically unattractive [3].

The first technologically significant breakthrough in ferroelectricity was the discovery of barium titanate (BaTiO_3) as a high- ϵ dielectric during the Second World War [4-7]. The relative permittivity of this ceramic was reported to be at least 1100, which was enormous compared to the dielectric constant of ~ 100 for the previous “highest- ϵ ”, rutile. Further insight was gained when BaTiO_3 was identified as being ferroelectric [8, 9] and that the pseudocubic (tetragonal) nature of this perovskite at room temperature gave the material its spontaneous polarization [10, 11]. Of equal importance was the realization that if a ferroelectric polycrystalline ceramic is poled (held at an electric field greater than the coercive field), the dipoles in the previously isotropic ceramic can be aligned to form a unique polar axis that is electromechanically active [2]. Since its discovery in the 1940s, BaTiO_3 has been engineered to act as a temperature invariant, high permittivity, low

dielectric loss material for high capacitance devices. However, for piezoelectric and ferroelectric applications, BaTiO₃ has been supplanted by the family of lead zirconate titanate (PZT) solid solutions, which were first reported on by Jaffe *et al.* in 1954 [12].

1.2 A Description of Ferroelectricity:

Ferroelectrics are commonly described as non-centrosymmetric materials containing an electrically re-orientable spontaneous polarization at equilibrium. Although somewhat cumbersome, the adjectives of this definition—non-centrosymmetric, spontaneous, and re-orientable—adequately convey the material’s structural necessities for exhibiting all of the commonly quoted properties of these materials: piezoelectricity, pyroelectricity, and ferroelectricity.

Piezoelectricity is a material property that linearly relates applied stresses to induced dielectric displacements (direct piezoelectric effect) or applied electric fields to induced strains (converse piezoelectric effect) [13]. A third rank tensor is necessary to fully describe the piezoelectric response of a crystal. Neumann’s principle establishes that the symmetry of a crystal’s point group is reflected in the symmetry of its external properties. Thus, only materials that lack an inversion point (i.e. are non-centrosymmetric) can exhibit piezoelectricity. Centrosymmetric materials are incapable of containing odd-rank tensor properties because the inversion symmetry produces perfect compensation for such “directional” properties. Of the 32 point groups, 21 lack inversion point symmetry and 20 of these display piezoelectricity (only the point group 432 fails to be piezoelectric) [2]. Thus, the adjective “non-centrosymmetric” establishes the piezoelectric nature of ferroelectric materials.

However, piezoelectric response does not guarantee the “polar” nature of a material. In some piezoelectric crystals such as quartz, polar directions are arranged such that they self-compensate and only exhibit a piezoelectric response under inhomogeneous

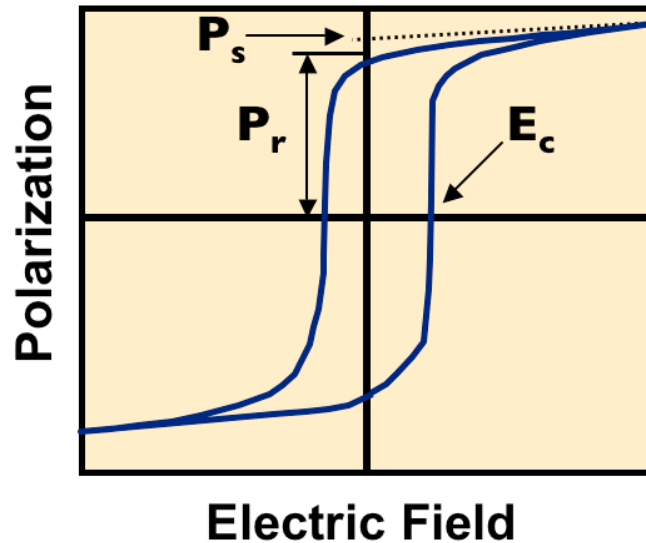


FIG 1-1 – Depiction of the Hysteretic Polarization Response in Ferroelectric Materials: *Schematic plot of an idealized P-E loop for a ferroelectric material indicating the remanent polarization (P_r), saturation polarization (P_s), and coercive field (E_c).*

stresses—not under hydrostatic conditions [2]. Only 10 of the 20 piezoelectric point groups (those that contain a unique axis of rotation with no mirror plane perpendicular to it [14]) allow for the existence of permanent dipoles—that is a unique polar axis [15]. These “polar” materials will exhibit a hydrostatic piezoelectric response as well as the additional property of pyroelectricity. In such crystals, temperature changes cause thermal fluctuations in the basic ionic and electronic forces of the material, varying the magnitude of the permanent dipole moments within the material. The pyroelectric effect manifests as a variation in the polarization magnitude as a result of a temperature change [15]. Pyroelectricity is intrinsically established in ferroelectrics because of their “spontaneous” polarization.

Yet, materials with a unique polar axis, such as ZnO or GaN, are not necessarily ferroelectric. The final requirement, a switchable or “re-orientable” dipole, is required for ferroelectric response. Ferroelectricity is essentially a hysteretic polarizability in response to an applied electric field. As shown in Fig. 1-1 a plot of polarization vs. electric field

will have the classic hysteresis loop shape analogous to the magnetization response of a ferromagnet.

Also akin to ferromagnets is the transition temperature. Above some transition temperature, denoted the Curie point (T_c), ferroelectric materials transform to a higher symmetry paraelectric phase which exhibits a dielectric response that follows the Curie-Weiss law:

$$\epsilon_r = \frac{C}{T - T_o} \quad [\text{Eqn. 1-1}]$$

where C is the Curie constant and T_o is the Curie-Weiss temperature ($T_o \leq T_c$) [16].

1.2.1 A Description of the Ferroelectric Phase Transition:

Many approaches can be taken to understand the ferroelectric phase transition; however, an examination of lattice dynamics is perhaps the most useful for visualizing the structure-property relationships that occur in the material. From this viewpoint, a displacive ferroelectric transition occurs if a transverse optic branch of the phonon spectrum has an instability at the Curie temperature. As the instability is approached from high temperatures, this phonon mode “softens” until its frequency reaches zero and the wavelength becomes infinite. Thus, at the transition temperature, the soft mode vibration locks in a displacive distortion, which creates the spontaneous polarization necessary for ferroelectricity. However, this vibrational mode remains easily activated, providing a significantly larger contribution to the dielectric permittivity than other modes. Fig. 1-2 demonstrates how soft modes can create both ferroelectric and anti-ferroelectric behavior (the latter being a non-polar state with alternating opposite dipoles) [15, 16].

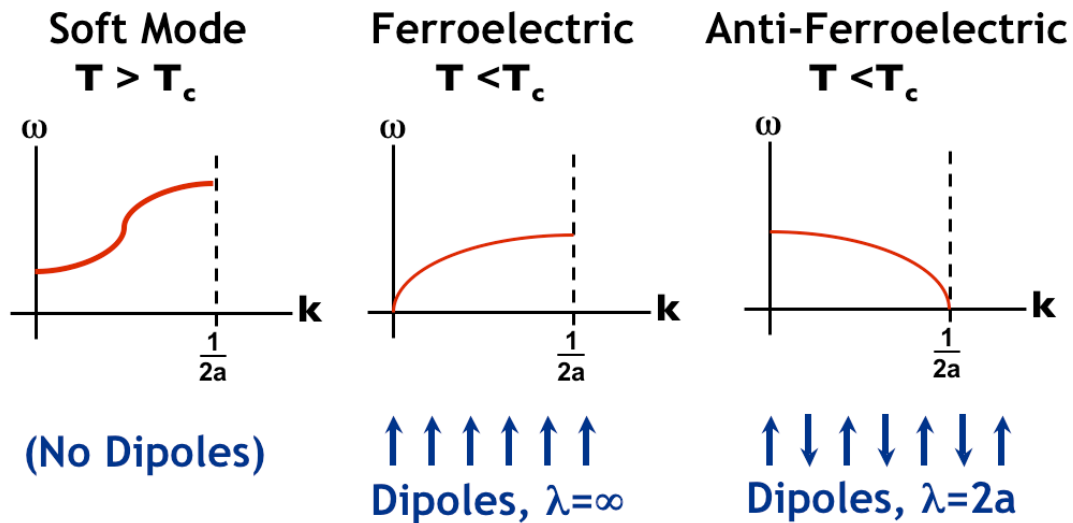


FIG 1-2 – Soft Mode Description of the Ferroelectric Phase Transition: Dispersion spectrum showing the change in a soft mode phonon when a material is cooled below the Curie temperature. The “frozen” phonon vibration ($\omega = 0$) in ferroelectric materials creates a set of distortions/dipoles that oscillate with infinite wavelength ($k = 0$) while anti-ferroelectric materials have dipoles that oscillate with a wavelength that is twice the unit cell dimension ($k = 1/\lambda = 1/2a$). Based on Ref [15].

1.2.2 Ferroelectricity in Perovskite Crystals:

Ferroelectrics with the perovskite crystal structure are probably the most important class of ferroelectrics for technological applications. An ideal perovskite structure is depicted in Fig. 1-3 and is described as having a cubic unit cell with A-site cations at the corners, a B-site cation in the center, and oxygen anions on the six faces. This structure is capable of adjusting through minor distortions to accommodate A and B site cations with inexact radii sizes to achieve ideal 12-fold and 6-fold respective coordinations. In the ideal perovskite structure, twice the B-O bond length ($2r_{B-O}$) should equal the unit cell dimension (a), while twice the A-O bond length ($2r_{A-O}$) should equal the face diagonal ($a\sqrt{2}$). From this analysis, a tolerance factor can be derived:

$$t_f = \frac{\sqrt{2}r_{A-O}}{2r_{B-O}} \quad [\text{Eqn. 1-2}]$$

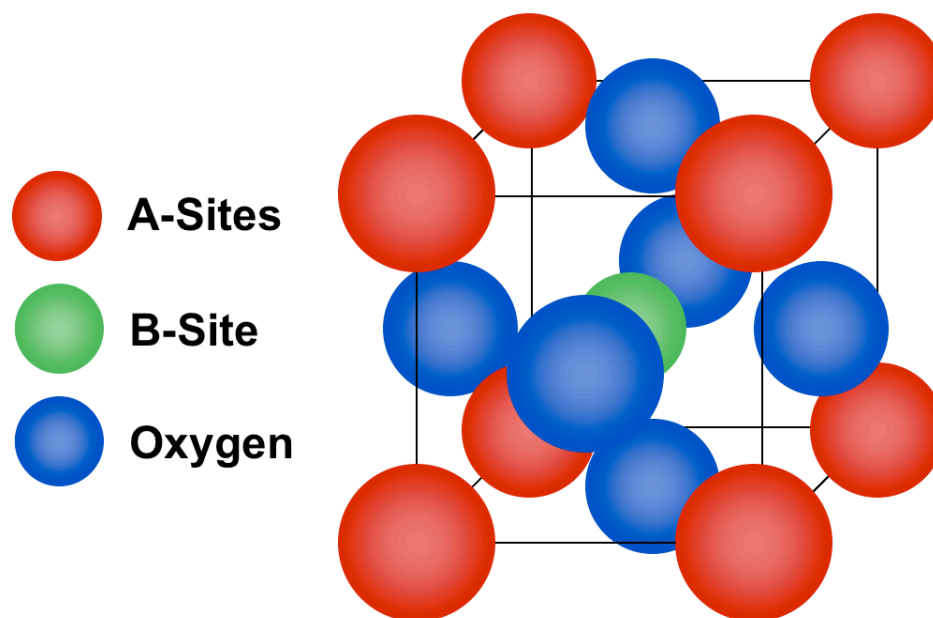


FIG 1-3 – Illustration of the Perovskite Unit Cell: *A drawing of the undistorted perovskite unit cell with the location of A-site and B-site cations labeled.*

where the tolerance factor (t_f) should equal 1 for the ideal case. When the B-site cation is too small for its site ($t_f > 1$), such as in BaTiO_3 and PbTiO_3 , this cation shifts towards an oxygen face, taking on an effective 5-fold coordination. To accommodate the reduction of the B-O bond length, the unit cell contracts in the plane perpendicular to the shift creating a tetragonal distortion. Conversely, if the A-site cations are too small ($t_f < 1$), the oxygen octahedron tilts. The octahedron may tilt towards the corners to create a rhombohedral distortion such as in Zr-rich PZT or towards the edges to create an orthorhombic distortion such as in the antiferroelectric PbZrO_3 [17]. Since the space group of cubic perovskite ($\text{Pm}3\text{m}$) is centrosymmetric, these distortions are necessary to remove the center of symmetry and stabilize the existence of permanent dipoles.

Although some technologically important ferroelectrics such as LiNbO_3 take on layered structures, the remaining portions of this chapter will focus on ferroelectricity in perovskite-based materials unless otherwise noted.

1.3 Ferroelectric Domains:

When a perovskite ferroelectric is cooled below T_c , the direction of the spontaneous polarization is equally probable in all of the crystallographically equivalent polarization directions—for instance, all six $\langle 100 \rangle$ directions for tetragonal distortions or all eight $\langle 111 \rangle$ directions for rhombohedral distortions. Inevitably, electrical and mechanical boundary conditions limit the volume over which a particular polarization direction can extend. As a result, regions of uniformly oriented spontaneous polarizations develop called domains. Domain walls separate domains with different spontaneous polarization orientations [13, 16].

Physically, the electrical constraint imposed on the material is a depolarization field developed from a “surface charge” that results from the emergence of the spontaneous polarization. Because a discontinuity in the periodic dipole alignment occurs at the surface or at an interface (grain boundary), an electric field forms due to the uncompensated dipole charges at this surface (“surface charge”). This field must act in opposition of the dipoles. Mathematically this situation is expressed using the dielectric displacement vector (D), which describes the surface charge density of the material:

$$D = \epsilon_0 E + P \quad [\text{Eqn. 1-3}]$$

where ϵ_0 is the permittivity of free space (8.85×10^{-12} F/m), E is the applied electric field, and P is the induced polarization of the material, which is also a function of the electric field:

$$P(E) = P_s + \epsilon_0 \chi E \quad [\text{Eqn. 1-4}]$$

where P_s is the spontaneous polarization and χ is the dielectric susceptibility [16, 18]. Assuming no charge compensation from outside charges ($D = 0$) and using the definition of the relative permittivity (dielectric constant) of a material ($\epsilon_r = 1 + \chi$) these expressions become:

$$E_D = -\frac{P_S}{\epsilon_o \epsilon_r} \quad [\text{Eqn. 1-5}]$$

where E_D is the depolarization field for spontaneous polarization. The volume density of energy stored by this electric field is then given by:

$$dW = \int E_D \cdot dP = \int -\frac{P_S}{\epsilon_o \epsilon_r} dP \quad [\text{Eqn. 1-6}]$$

which implies that the energy associated with the depolarization field inside the system increases with domain size as:

$$U_{field} \propto \frac{P_S^2}{2\epsilon_o \epsilon_r} V \quad [\text{Eqn. 1-7}]$$

where U_{field} is the energy and V is the volume of the domain [18]. At some volume, the increase in energy will make a single domain unstable. To lower its energy, the domain can split into two domains with different spontaneous polarization directions. However, the domain wall that separates the two new domains has an interfacial energy associated with it. The balance of depolarization field energy and domain wall interfacial energy partially determines domain size. A similar analysis can be undertaken for strain-related energies imposed by the lattice distortions undergone at the phase transition. This strain energy also influences domain size, specifically in ceramic (polycrystalline) ferroelectrics [13, 18].

Immediately after cooling below T_c , the complex electrostatic and elastic constraints present in a polycrystalline ceramic lead to a complex domain structure that often exhibits no net polarization direction. Thus, the ceramic is non-polar (neither piezoelectric nor pyroelectric) until the domains are aligned with the application of an

external electric field (poling) [13, 16]. Because ceramics have randomly oriented grains, the maximum spontaneous polarization is a fraction of the single-crystal value and has been calculated to be 0.83, 0.87, and 0.91 for perovskites with tetragonal, rhombohedral, and orthorhombic distortions respectively (distortions with more available polarization directions are more accommodating) [13].

1.3.1 Domain Walls:

A domain wall is typically classified by the angular difference between the spontaneous polarization directions of the two domains it separates. Besides 180° domain walls, tetragonally distorted perovskites can have 90° domain walls while rhombohedrally distorted perovskites can have 71° and 109° domain walls. As demonstrated in Figs. 1-4 and 1-5, 180° domain walls are capable of reducing the electrostatic energy associated with E_D while non- 180° domain walls can relieve both electrostatic as well as elastic energies. Because non- 180° domain walls separate domains with different spontaneous strain tensors, these walls are ferroelastic as well as ferroelectric. Due to their ferroelastic nature, the motion of non- 180° domain walls contributes to the piezoelectric response of a ferroelectric (180° domain wall movement does not) [16].

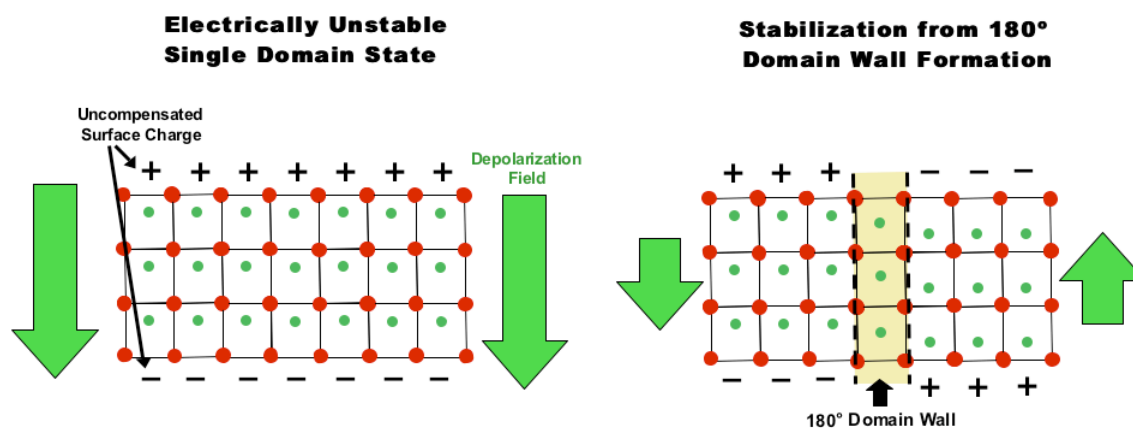


FIG 1-4 – Formation of 180° Ferroelectric Domain Walls: *Illustration of how 180° domain wall formation in a tetragonally distorted perovskite ferroelectric can relieve electrostatic energy.*

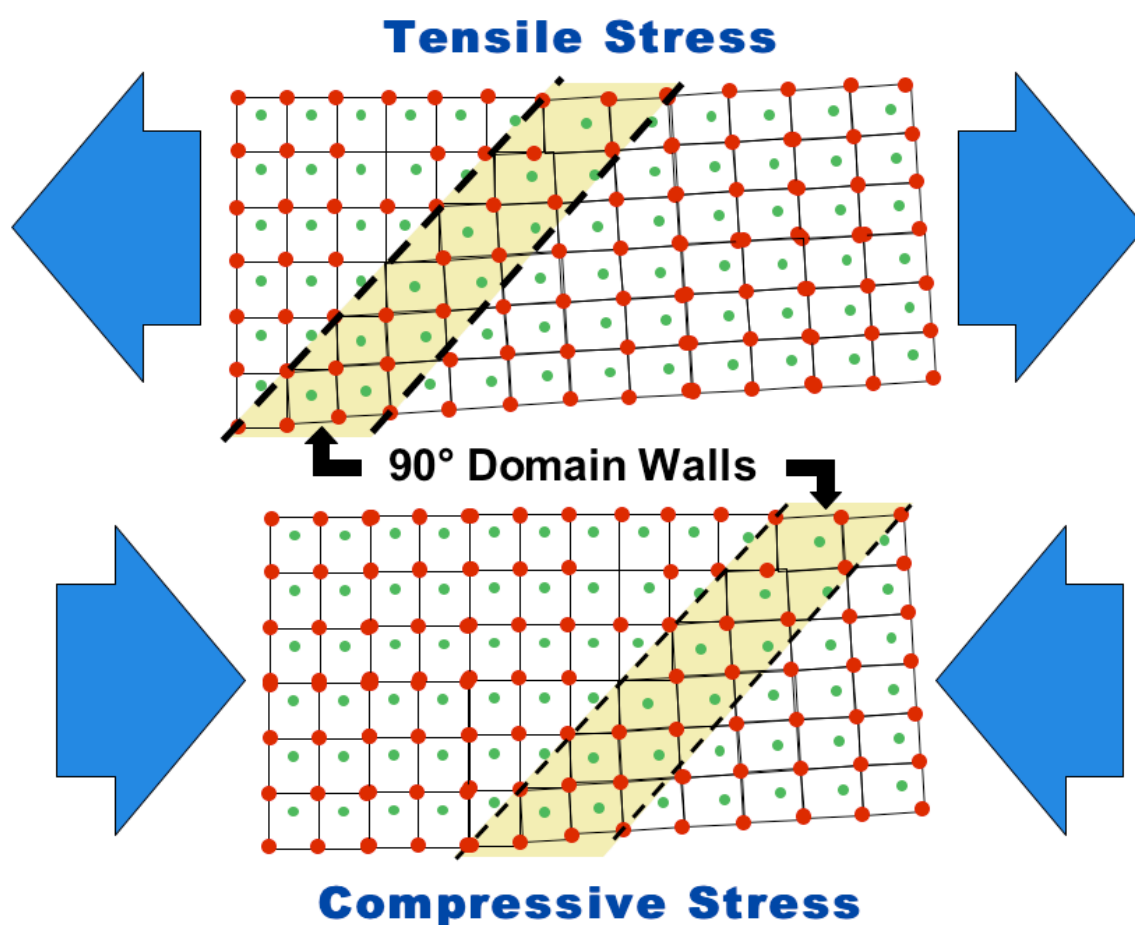


FIG 1-5 – Strain Energy Relief by 90° Domain Wall Motion: *Illustration of how 90° domain wall motion in a tetragonally distorted perovskite ferroelectric can relieve strain energy.*

1.3.2 The Extrinsic Contribution to Ferroelectric Properties:

Many of the properties observed in ferroelectrics have two contributing mechanisms—the intrinsic interactions of the lattice dipoles with the external stimulus and the extrinsic response resulting from domain wall motion. For example, when an electric field is applied to a ferroelectric, the dipoles “stretch” in response, creating a larger polarization. Concurrently, domain walls sweep through the material, switching domains that have a vectoral component opposing the field. Applied stresses are also

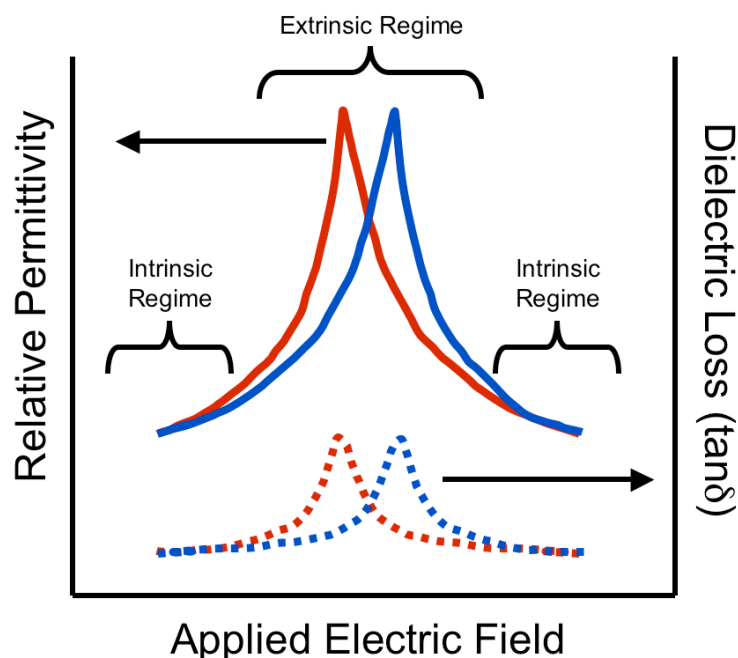


FIG 1-6 – Illustration of Dielectric Tunability in Ferroelectric Materials: *Depiction of the change in dielectric response with applied electric field for ferroelectric materials. Regions of intrinsic (unit cell dipoles) and extrinsic (domain wall motion) dominated responses are labeled.*

accommodated by changes in both the unit cells and domain structure. Both the intrinsic and extrinsic contributions are significant to the overall dielectric and piezoelectric response of a ferroelectric material [13, 16].

The extrinsic effect is particularly important in measurements of capacitance vs. applied voltage (C-V). In these measurements, a small amplitude AC voltage is used to sample the capacitance of a material over a larger DC bias. An example of a classic C-V loop is shown in Fig. 1-6. At high DC biases, the extrinsic contribution is reduced because most domains have been switched or have become immobile due to elastic constraints [13]. Thus, at high biases, the AC voltage is sampling primarily the intrinsic dielectric response. As the DC bias is relaxed, domain walls can begin to move in response to the AC voltage, thereby increasing the dielectric response. However, domain wall motion also requires energy and creates dielectric loss. The maximum in the capacitance and loss occurs when domains can fully switch and the material is dielectrically soft [16]. This

change in capacitance/permittivity with applied voltage/field is known as dielectric tunability and is quantified by:

$$\%tunability = \frac{\epsilon_{max} - \epsilon_{min}}{\epsilon_{max}} \cdot 100\% \quad [\text{Eqn. 1-8}]$$

1.4 Ferroelectrics for Commercial Applications:

Ferroelectric materials are used or are proposed for use in a plethora of applications. In this section a brief summary of the major applications, particularly emphasizing thin film technology, is presented. Reasons for how these devices benefit from the incorporation of ferroelectrics are discussed. Also a comparison is given between two of the most commonly investigated ferroelectric materials: barium titanate and lead zirconate titanate.

1.4.1 Applications of Ferroelectrics:

Capacitors – In addition to the electronic and ionic contributions that most insulating ceramics possess, ferroelectrics have an additional dipolar contribution to their dielectric response as a result of their spontaneous polarization. This dipolar contribution along with the extrinsic domain wall response makes ferroelectrics some of the highest known dielectric constant materials with ϵ' values ranging from 5,000 (single crystal BaTiO₃ at room temperature) to >50,000 (for some relaxor compositions). However, the strong dependency of dielectric properties on temperature, especially near phase transitions, is of serious concern for many applications. Thus, much research has focused on developing dopants and microstructures that will shift T_c, suppress the transition, or create relaxor behavior. Compositionally modified BaTiO₃ material is probably the most successful example and is used almost exclusively in the multilayer capacitor industry [2, 13].

Tunable Dielectrics – As already explained, ferroelectrics exhibit a tunable dielectric response with applied dc fields. This property makes ferroelectrics attractive for tunable high-frequency solid-state devices. By tuning the dielectric component in an RF circuit,

high-frequency signals can be systematically selected creating, for instance, a miniaturized frequency-tunable filter / antenna [19]. Ferroelectric thin films are especially attractive because of their compatibility with CMOS technology and the low voltages required for tuning. (Ba,Sr)TiO₃ has been extensively evaluated because of its high tunability but low dielectric loss in the paraelectric state [20].

Opto-Electronic Devices – The re-orientable dipoles of ferroelectric materials create a strong electro-optic response (the refractive index changes with applied electric field). This property can be exploited to fabricate optical wave devices like filters and switches. The primary requirement is that the ferroelectric be transparent. Thus, the elimination of porosity and other light scattering centers is crucial. Important examples of opto-electronic ferroelectrics are (Pb,La)(Zr,Ti)O₃ (PLZT), LiNbO₃, and LiTaO₃ [13].

Piezoelectric Applications – Piezoelectric materials can be evaluated by comparing their piezoelectric coefficients (d_{kij}), which relate strain (x_{ij}) to applied electric field (E_k):

$$x_{ij} = d_{kij} E_k \quad [\text{Eqn. 1-9}]$$

Ferroelectrics are attractive as piezoelectric materials because of their high piezoelectric coefficients; for example, quartz has a d_{11} values of ~2 pC/N while PZT has a d_{33} value of >250 pC/N [13]. In addition, the electromechanical coupling coefficient (k^2) for ferroelectrics can be above 0.8 [13], where k^2 describes the ratio of electrical energy converted to mechanical energy or vice versa and:

$$k^2 = \frac{d^2}{\epsilon_{uc} s} \quad [\text{Eqn. 1-10}]$$

where ϵ_{uc} is the unclamped (zero stress) dielectric constant and s is the compliance [16].

Because ferroelectrics can be poled, they offer the additional advantage of not requiring single crystal or highly-oriented material production; simple ferroelectric ceramics can be made piezoelectric [13, 16]. Consequently, piezoelectric ferroelectrics have been used in gas igniters, ultrasonics, and inkjet printer heads. Thin film ferroelectrics have been especially appealing for surface acoustic wave filters and actuation/sensing in microelectromechanical systems (MEMS).

At this point, it is important to recognize that a strong coupling coefficient can affect the dielectric constant when a ferroelectric is clamped (zero strain) such as in a thin film:

$$\epsilon_c = \epsilon_{ic} (1 - k^2) \quad [\text{Eqn. 1-11}]$$

where ϵ_c is the clamped dielectric constant. Thus increased piezoelectric response may come at the expense of reduced permittivity [2, 16].

Non-Volatile Memory: Because the polarization state of a ferroelectric can be switched between (at least) two directions, ferroelectric polarization can be used as a form of binary storage. Furthermore, because a ferroelectric maintains a remanent polarization at zero bias, this memory would require no refreshing—it is non-volatile. This application presumes that the polarization is strong enough to be read, easily switchable, and varies little with cycling or time. PZT has been proposed to be a good candidate. However, effects such as fatigue, aging, and imprint, which are discussed later in this thesis, currently limit the utility of ferroelectrics in non-volatile memory applications.

1.4.2 PZT and BaTiO₃ – Complementary Ferroelectrics:

The BaTiO₃ and PZT families of materials are complementary. Their respective properties dictate that these two classes of ferroelectrics are best suited for different applications. A comparison of relevant properties is presented in Table 1-1. PZT, for instance, has excelled in piezoelectric applications because of its markedly higher

piezoelectric coefficients and electromechanical coupling coefficient. Because of its higher Curie point, PZT piezoelectrics also age slower and can be used at higher operating temperatures. Furthermore, its larger remanent polarization makes PZT more attractive for non-volatile memory applications. In contrast, BaTiO₃-based materials have dominated dielectric applications. This dominance is partially due to its higher room temperature permittivity and its compatibility with base metal electrodes. Additionally, stoichiometry is fundamentally easier to maintain in BaTiO₃ because it contains low-volatility and highly refractory constituent oxides.

Table 1-1 – Property Comparison for BaTiO₃ and Pb(Zr,Ti)O₃ Ceramics: *A list of relevant dielectric, ferroelectric, piezoelectric, and pyroelectric properties for barium titanate and 52/48 PZT bulk ceramics at room temperature. Note that properties are quoted from the poled state. Data is compiled from references:[2, 13, 14, 21].*

Property	BaTiO₃	Pb(Zr_{0.52}Ti_{0.48})O₃
Curie Point (T _c)	120°C	386°C
Dielectric Constant (ϵ_r)	1620-1900	730-1180
Remanent Polarization (P _r)	8 $\mu\text{C}/\text{cm}^2$	36 $\mu\text{C}/\text{cm}^2$
Piezoelectric Coefficient (d ₃₁)	-79 pC/N	-93.5 pC/N
Piezoelectric Coefficient (d ₃₃)	191 pC/N	223 pC/N
Electromechanical Coupling Coefficient (k)	0.21-0.44	0.31-0.69
Pyroelectric Coefficient (P)	-20 nC/cm ² K	-27 nC/cm ² K*

*95/5 PZT composition.

1.5 PZT Thin Films:

Volumes of literature have been published on PZT thin films because of their technological importance and potential. This section focuses on specific topics (the influence of stress and film orientation) that are of most relevance to this thesis.

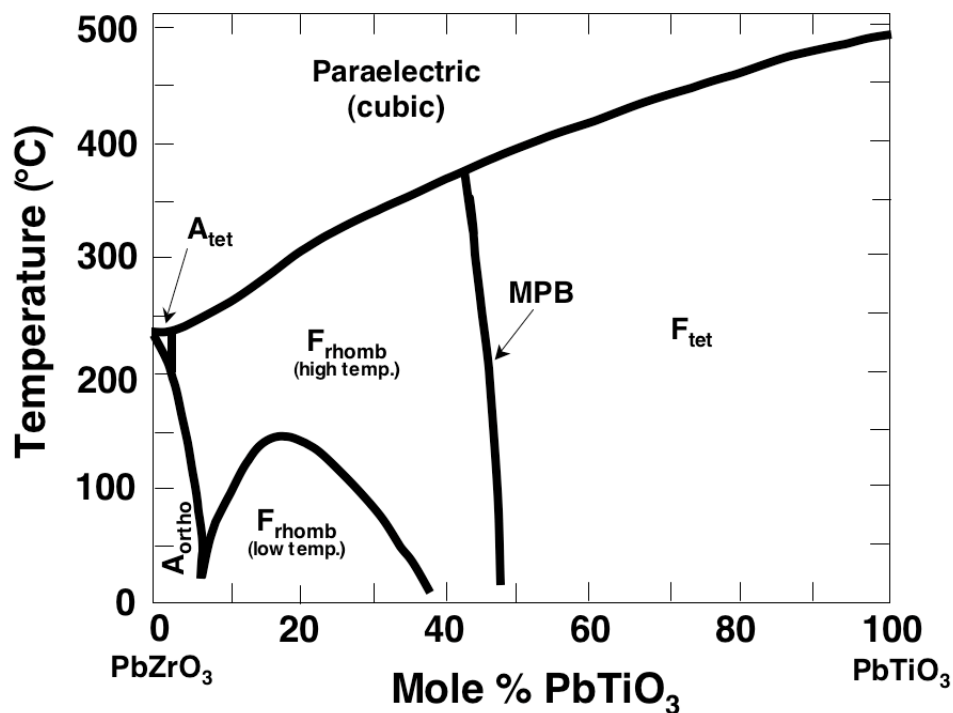


FIG 1-7 – Phase Diagram of the PbZrO₃ / PbTiO₃ Solid Solution System: Binary phase diagram for PbZrO₃ and PbTiO₃ indicating regions of composition and temperature for which the paraelectric, ferroelectric (F) and antiferroelectric (A) states are stable as well as the type of distortion that occurs in the perovskite structure—tetragonal (tet), rhombohedral (rhomb) or orthorhombic (ortho). From ref.[2, 22].

Before delving into these subjects, though, it is prudent to briefly summarize the structure-property relationships inherent to the PZT system. PZT is a solid solution of the high- T_c ferroelectric PbTiO₃ and the antiferroelectric PbZrO₃. As the phase diagram in Fig. 1-7 illustrates, PZT has both a rhombohedral and tetragonal ferroelectric phase [23]*. These two phases are separated by a morphotropic phase boundary (MPB) near the composition of 52/48 at room temperature. Near this MPB most of the ferroelectric-related properties in PZT reach a maximum—such as piezoelectric response and remanent polarization. The strong piezoelectric response and ease in poling near the MPB is believed to be a result of the domain structure. At the MPB both the tetragonal and

* Noheda *et al.* have demonstrated that a ferroelectric monoclinic phase may also exist near the MPB at about -25°C [23].

rhombohedral distortions are thermodynamically stable. Hence, 180° , 90° , 109° , and 71° domain walls are all active and the unit cell can accommodate 14 different spontaneous polarization directions [16]. Upon poling, 40-50% of the domains will be permanently altered compared to only about 10% in tetragonal BaTiO_3 [13]. Thus, the extraordinary ability of PZT at the MPB to re-orient its polarization allows it to retain a large remanent polarization. Moreover, the activity of 3 non- 180° domain walls creates a large extrinsic contribution to its piezoelectric response [16].

1.5.1 Effects of Stress in PZT Thin Films:

Because a substrate mechanically constrains a film from freely straining within the plane of the surface, stresses are often present in thin films. These stresses can impact the properties of a ferroelectric like PZT [24]. In a chemical solution deposited PZT film, tensile stresses are often present in the gel state due to volume shrinkage during solvent and organic removal. However, as long as the film does not crack or delaminate, these stresses can often be relaxed at higher temperatures through structural relaxations and viscous flow. More relevant to property modification are the stresses developed upon cooling the crystallized film. These stresses result from the mismatch between the film and substrate's coefficients of thermal expansion (CTE) [25]. These stresses may influence the final domain structure and hence the film's properties.

In thin films, ferroelectric domain structures are categorized in two general classes. Structures labeled "*c domains*" have spontaneous polarizations predominantly aligned perpendicular to the substrate. Alternatively, if the spontaneous polarization is principally within the substrate plane, it is referred to as "*a domain*" (Fig. 1-8). Because *c domain* material has the polar axis parallel to the poling direction (for an MIM structure), it exhibits a larger remanent polarization and piezoelectric response. In contrast, *a domain* films display higher permittivities because the dipoles are less constrained to vibrate perpendicular to the polar axis. Thus, *c domain* films are useful for piezoelectric and pyroelectric applications while *a domain* films make better capacitors [26, 27].

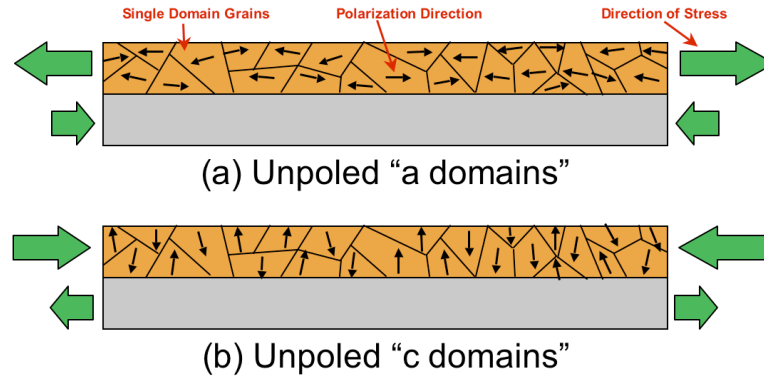


FIG 1-8 – Illustration of Stress Induced Domain Structure in PZT Thin Films: *When a film is placed under (a) tensile stress, ferroelectric domains align in the plane of the film. When a film is placed under (b) compressive stress, ferroelectric domains align perpendicular to the surface.*

Tuttle *et al.* [27] demonstrated that if PZT is deposited on a low CTE material like silicon, *a domains* develop due to tensile stresses within the film as it is cooled below T_c . Conversely, *c domains* developed when MgO or Al₂O₃ substrates, which have higher CTEs than PZT, were used. The properties of these PZT films reflected the domain structure. PZT on Al₂O₃ had P-E loops with higher remanent polarizations (40 $\mu\text{C}/\text{cm}^2$ vs. 20 $\mu\text{C}/\text{cm}^2$) and better polarization saturation than those prepared on silicon. Tensile stress also appeared to tilt the P-E loop, but no change in coercive field was observed [27]. Shepard *et al.* reported similar stress effects on P-E behavior for PZT films that were systematically stressed through mechanical wafer flexuring [26].

1.5.2 Effects of Crystalline Orientation on PZT Thin Films:

Through preferred nucleation or growth kinetics, PZT thin films may assume a textured or oriented crystalline direction. Because the energy barrier to nucleation (~ 441 kJ/mol) is four times greater than the activation energy for growth (~ 112 kJ/mol), nucleation behavior will generally be the dominant influence [28]. Heterogeneous

nucleation at the substrate is typically observed for PZT thin films. Thus, if the substrate is closely lattice matched to a particular PZT plane, the film may become textured. For example, platinized silicon substrates with Ti adhesion layers are often observed to induce *111* PZT texturing. A combination of the *111* Pt and diffused Ti is believed to create an epitaxial match for *111* PZT [29-31]. If no lattice match is possible, it has been suggested that a *100* texturing may still dominate. Due to charge considerations, the (100) face has the lowest surface energy and will act as the fast growth direction [30, 32]. Thus, if PZT continues to nucleate heterogeneously at the substrate, *100* crystallites will dominate due to their fast growth kinetics [30].

Properties are expected to be anisotropic with crystalline orientation. Unfortunately, a method for growing single crystals of PZT has yet to emerge. Property anisotropy has been investigated with highly oriented PZT films; however, decoupling the effects of complex domain structures expected in films is difficult. However, it is still instructive to examine some trends from the literature. The MOCVD deposited *100* PZT 50/50 films of Bai *et al.* [33] exhibited remanent polarizations of $49.7 \text{ } \mu\text{C}/\text{cm}^2$, which is almost twice as high as the value for bulk PZT ceramics ($\sim 26 \text{ } \mu\text{C}/\text{cm}^2$ [2]) of the same composition. Correspondingly, Tuttle *et al.* [34] reported a 50% increase in remanent polarizations when going from random to *100* orientation in 40/60 PZT films. This group also reported a decrease of $\sim 20\%$ in the permittivity of *100* oriented films relative to random films [34].

1.6 Ferroelectric Aging:

Aging effects are spontaneous changes in material properties that occur over time. The rate of aging typically increases with increasing temperature [16]. In 1948 Marks [35] demonstrated that permittivity decreased linearly with the log of time for ferroelectric materials as given by the following empirical expression:

$$\varepsilon_r(t) = \varepsilon_r(t = 0) - A \log(t) \quad [\text{Eqn. 1-12}]$$

where A is the aging rate and t is time. A more complete investigation revealed that spontaneous polarization, piezoelectric response, and dielectric loss also decrease with time, but all of these aged properties can be restored if the material is heated, even briefly, above T_c [36]. Moreover, aging effects are not observed for materials in their paraelectric state. From these observations, aging is concluded to be a relaxation process in the domain walls' positions [36]. If domain walls reach a low energy configuration and vibrate less, then extrinsic contribution to properties are expected to diminish. Moreover, the lack of aging in the paraelectric state is consistent with this hypothesis.

When a ferroelectric ceramic is initially poled or cooled below T_c , internal strains develop due to both electronic and elastic constraints. Aging occurs when domain walls and defects move to relieve these strains [14]. Two basic mechanisms for the stabilization of domain walls during aging have been proposed: alignment of defect dipoles and space charge trapping at domain walls. Defects such as vacancies and impurity atoms are believed to align with the spontaneous polarization or spontaneous strain tensors within a domain. Such alignments create defect dipoles that resist the switching of the domain and stabilize the domain wall's position. Defect dipoles can be extremely important in PZT where PbO volatility can easily create V_{Pb}'' and V_O'' . The high mobility of the oxygen vacancies to form defect dipoles can lead to rapid aging [16, 37]. Another contribution may be the collection of charges (electrons, holes, or point defects) at domain walls. This collection of defects can act to stabilize the position of the domain wall by reducing the local electronic charge imbalance or elastic strain. Thus, a domain wall's motion away from these collected defects becomes unfavorable [16, 37].

The defect alignments that occur during aging create an internal electric field, which acts additively to the coercive field of that domain. Hence, if the ferroelectric is aged in the poled state, the coercive field for reversing the poled direction is effectively increased while the coercive field for stabilizing the poled direction is decreased. Thus, the entire P-E loop is shifted. This behavior is illustrated in Fig. 1-9 and is the basis for the "imprint" phenomenon that destroys non-volatile memory devices. If this shift is

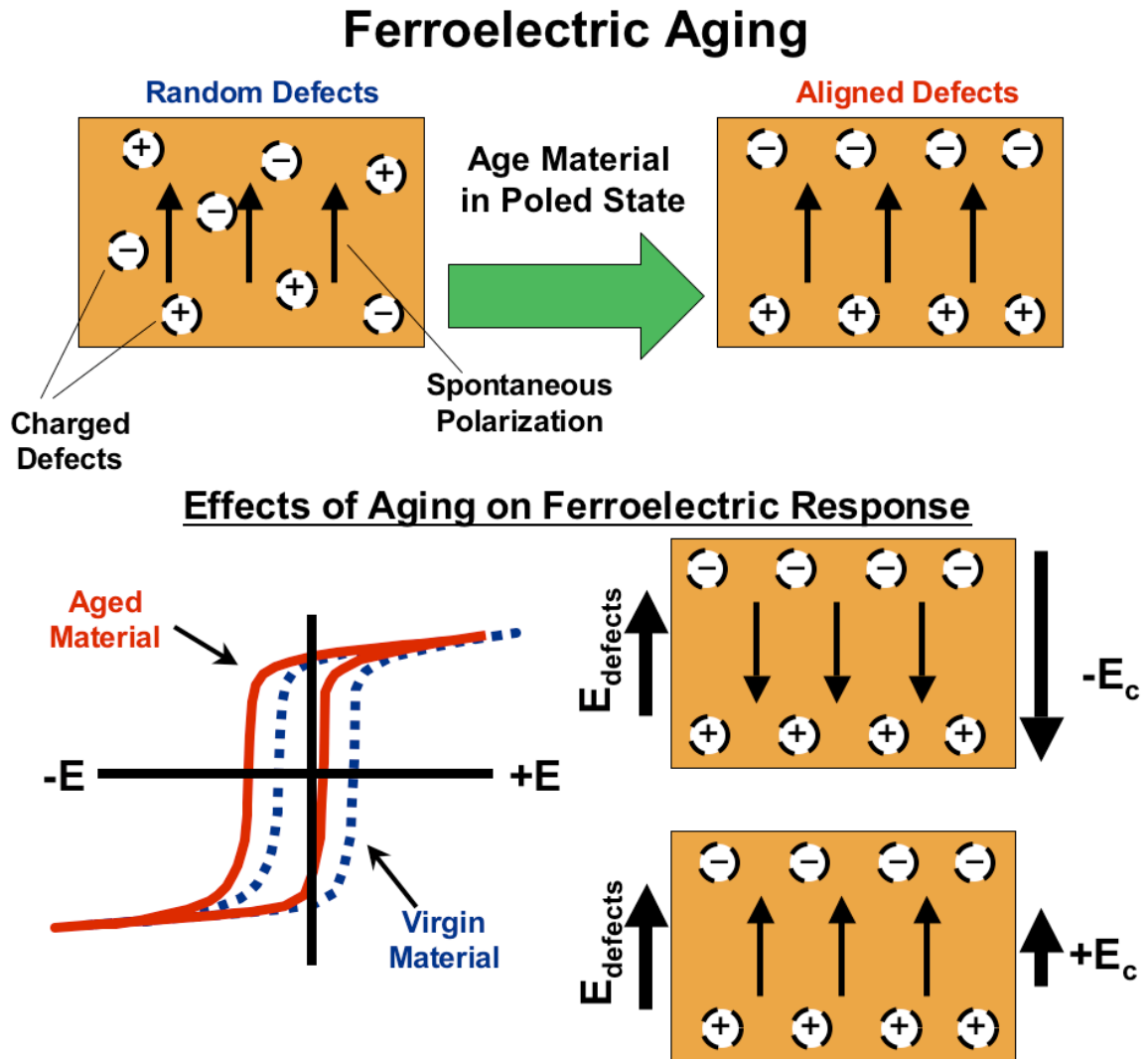


FIG 1-9 – Aging in Poled Ferroelectric Materials: *Depiction of how over time mobile charges can align in a poled ferroelectric material and subsequently impact the polarization response. The observed shift in the P-E loop is known as “imprinting.”*

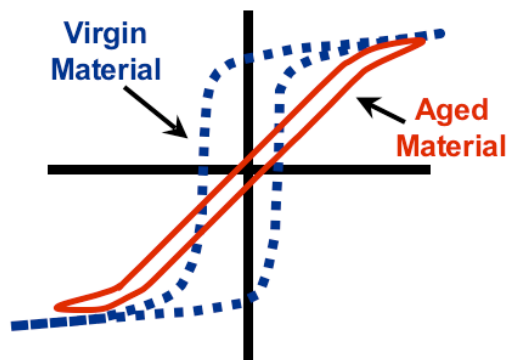


FIG 1-10 – Effect of Aging in Unpoled Ferroelectrics: *Illustration of the effect of aging on the polarization response of an unpolarized ferroelectric material.*

significant, the nominal switching voltage will be incapable of switching the polarization state and the memory device will be rendered useless [16, 37]. For ceramics that have randomly oriented domains (i.e. after cooling below T_c), this internal field leads to a constriction of the P-E loop as shown in Fig. 1-10 [16, 36].

1.7 Ferroelectric Fatigue:

In general, fatigue is a change in a material's properties as a result of cyclic external loading and has been classically associated with mechanical degradation. More commonly in ferroelectrics, fatigue relates to the loss of switchable polarization and piezoelectric response as a result of electrical cycling. However, similar degradation has been observed in ferroelectrics due to mechanical cycling and exposure to UV light [18]. Because fatigue creates a decrease in remanent polarization with electric cycling, it is of particular concern when developing PZT films for applications such as non-volatile memory. Thus, this discussion will primarily focus on fatigue in PZT thin films.

The classical effect of fatigue on a P-E loop is shown in Fig. 1-11. Fatigue typically results in a tilted loop with a lower remanent and switchable polarization. Graphically, fatigue is usually plotted as P_r or P_{sw} (switchable) versus the log of the number

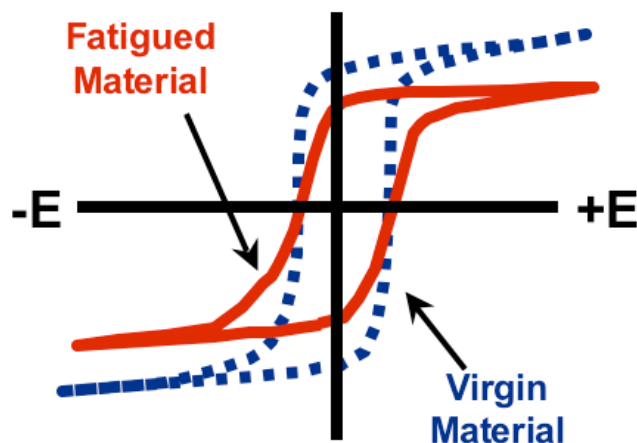


FIG 1-11 – Change in P-E Response as a Result of Ferroelectric Fatigue: *Illustration of P-E loop tilting and loss of polarization as a result of electrically cycling (fatiguing) a ferroelectric thin film with metal electrodes.*

of cycles. Note that the coercive field is typically invariant with cycling unless leakage current degrades the ferroelectric. If leakage current degradation is active, then the loop will become rounded (saturate poorly) and the coercive field will increase [38].

Two developments in the 1990s created excitement in ferroelectric fatigue research. The first discovery was that PZT films with conductive oxide electrodes exhibited negligible fatigue for a significantly longer number of cycles than devices using traditional noble metal electrodes [39]. With Pt electrodes, PZT typically fatigues within 10^4 to 10^7 cycles while with conductive oxide electrodes this can be extended to 10^9 – 10^{12} cycles [38]. These studies found maximum fatigue retardation when oxide conductors were used as both top and bottom electrodes, indicating that the electrode / ferroelectric interface is probably critical in determining fatigue properties [39]. Normal fatiguing rates have been observed, though, for certain combinations of conductive oxide materials and PZT compositions and in oxide electrode systems placed under other external stressing conditions such as UV exposure [37, 40]. The second significant discovery was that Bi-based layered perovskites like $\text{SrBi}_2\text{Ta}_2\text{O}_9$ (SBT) exhibit minimal fatigue past 10^{12} cycles even with the use of conventional metal electrodes [41].

1.7.1 General Discussion of Fatigue Mechanisms:

Despite the technological advancements in improving fatigue resistance, the specific mechanisms for ferroelectric fatigue are still controversial. In general, it is agreed that cyclic electrical stressing creates or redistributes imperfections within the material. These imperfections then degrade the switchable polarization. In their 2001 review of ferroelectric fatigue research, Tagantsev *et al.* [38] note three possible scenarios:

- (1.) The active electrode area is reduced.
- (2.) The amount of electric field within the ferroelectric is decreased.
- (3.) The switching of domains becomes more difficult.

Scenario (1), the burning or delamination of the top electrode, is an “artificial” loss of polarization (no change in the material) and should be easily identifiable since remanent polarization and capacitance will be affected equally. This mechanism is considered trivial by Tagantsev *et al.* and is only applicable in poorly processed systems. Scenario (2) assumes that a low-dielectric passive layer develops near the electrode and reduces the voltage drop in the ferroelectric due to the series capacitance. The large voltage drop in the passive layer may also lead to electron injection, which could cause further degradation. However, no strong experimental evidence has emerged to indicate the existence of this passive layer [38].

Scenario (3), frozen domains, has received the most attention and has spawned two well-developed hypotheses: domain wall pinning and seed inhibition. In *domain wall pinning*, defects are proposed to pin macroscopic domain walls from moving, thereby inhibiting domains from growing or switching [37]. In *seed inhibition*, regions of the ferroelectric are believed to have a finite number of seed nuclei present at the top electrode interface, which grow into the opposite domain upon switching. Once defects suppress the growth of all the seeds in a single region, that region can no longer switch, leaving a large, unswitchable domain [38]. In the following two sections the experimental support for these two mechanisms are discussed, and evidence is given for why seed inhibition is believed to be the primary fatigue mechanism under standard testing conditions.

1.7.2 Fatigue – Domain Wall Pinning Hypothesis:

The domain wall pinning hypothesis was proposed by Warren and colleagues at Sandia National Laboratories in the mid-1990s [37, 42, 43]. This hypothesis centers on mobile electronic charge carriers (electrons and holes) becoming trapped at discontinuities in the polarization (domain boundaries) and pinning the domain wall's motion by electrically stabilizing the domain wall's position near the trapped defects [37, 44]. An illustration of this model is shown in Fig. 1-12.

The evidence for electronic domain wall pinning arises from experiments that induce fatigue using stresses other than electrical cycling. For instance, the P-E loop of PZT becomes strongly tilted if it is biased below E_c and exposed to UV light greater than the bandgap. It is suggested that this bias creates numerous domain walls that can easily trap the optically excited electron-hole pairs (ehps). This fatigue can be reversed through ehf recombination if held at reverse saturation and re-exposed to UV light. Similarly, thermally induced ehps were shown to cause fatigue when the material was held at 100°C and low biases. The electronic nature of the trapped defects was verified by restoring the fatigued state through optical illumination. Fatigue induced by electrical cycling was also shown to be restorable with UV illumination, seeming to indicate a similar process [42]. Furthermore, similar effects were shown to occur in single crystal BaTiO₃, indicating that charge trapping was not just occurring along grain boundaries [43].

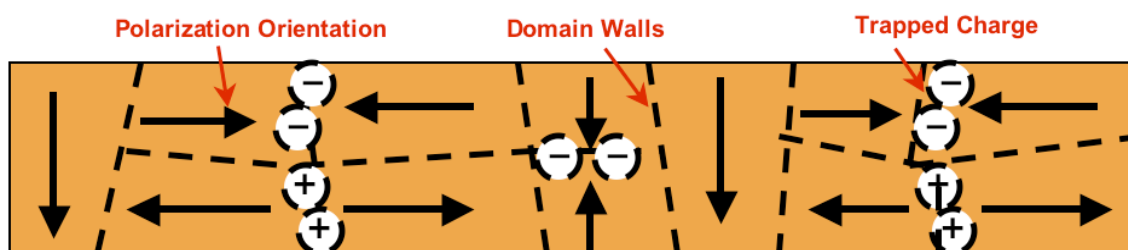


FIG 1-12 – Domain Wall Pinning Model of Ferroelectric Fatigue: *Drawing of how mobile electronic or ionic charge defects can stabilize the position of domain walls and effectively pin their position.*

1.7.3 Fatigue – Seed Inhibition Hypothesis:

Fig. 1-13 demonstrates the seed inhibition model for ferroelectric fatigue that has been developed by Colla, Tagantsev, and colleagues at the Swiss Federal Institute of Technology (EPFL) [38, 45-48]. This model begins with the premise that homogeneous nucleation of reverse domains is essentially impossible because it would require 10^3 kT of energy [38, 49]. Thus, domain switching must nucleate in defective regions where remnant “seeds” of oppositely directed domains are trapped. It is surmised that the electrode/ferroelectric interface is optimal for such defect seed trapping—particularly at the top electrode, which is usually of lower quality [47]. These authors propose that the built in field (E_{bi}) due to band bending at the electrode interface preferentially stabilizes seeds with orientations along E_{bi} [38]. When fatigue inhibits seed growth in some regions, islands of frozen polarization will develop. These frozen regions

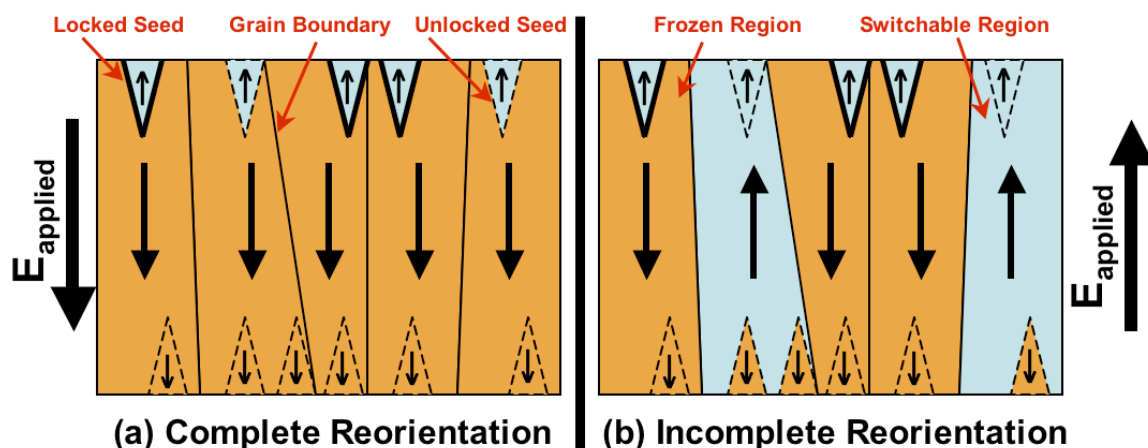


FIG 1-13 – Seed Inhibition Model of Ferroelectric Fatigue: *Schematic drawing showing locked or unlocked nano-domain seeds at the electrode interface in a fatigued ferroelectric film. In this schematic, all seeds at the bottom interface are unlocked allowing for complete reorientation (a) when a downward electric field is applied. In (b) the locked seeds at the surface cause frozen domain regions when an upward electric field is applied to the system.*

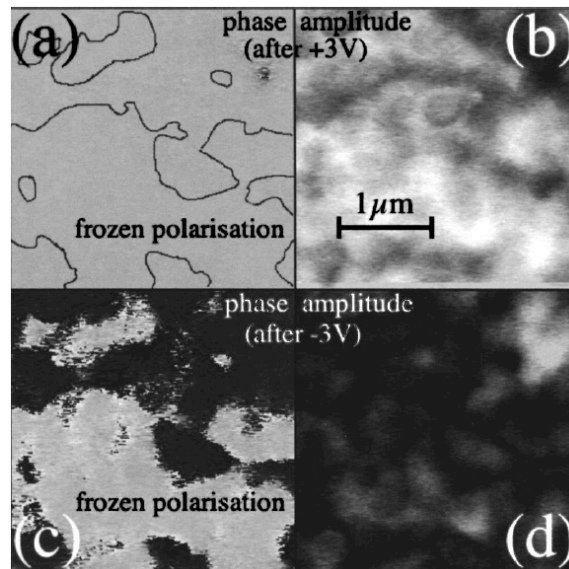


FIG 1-14 – AFM Assisted Piezo-Response Images of a Fatigued PZT Film: *AFM piezo-response images reported in ref. [45] showing phase (a and c) and amplitude (b and d) maps of a fatigued Pt-PZT-Pt structure. Images (a) and (b) are after positively poling the film while images (c) and (d) are after negative poling. Bright regions correspond to bottom-to-top polarization directions while dark areas correspond to top-to-bottom polarization directions. These images indicate complete switching in one polarization direction, but frozen domains upon reverse poling.*

will all exhibit the same polarization direction. Unlocked domains will continue to completely switch. Thus, the material will be fully switched in one poling direction but not the other. This situation has been observed with piezo-response force microscopy (PFM) and the images are reproduced in Fig. 1-14 [45, 47].

Further evidence has been presented by the EPFL group to discriminate between the seed inhibition and domain wall pinning mechanisms. Two premises were used in this discrimination: first, the profile of the cycling wave should impact which mechanism is active; second, the difference in the final domain structure (Fig. 1-15) should impact the film's properties [48]. As alluded to in the previous section, if the pulse voltage is held for extended periods of time within a regime of large “domain wall density” (i.e. near E_c), then domain wall pinning is more likely to occur. In [48] it was demonstrated that a triangular

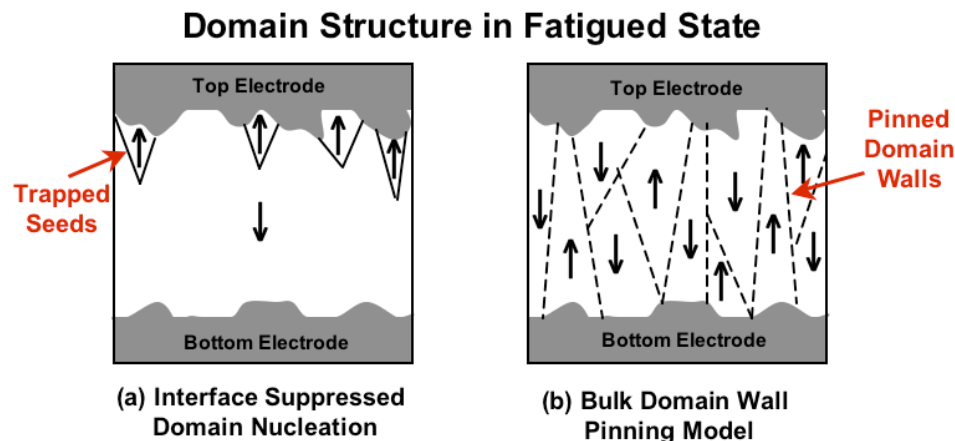


FIG 1-15 – Comparison of Fatigued Domain Structure for Two Different Models: *The domain structure of a fatigued ferroelectric in the poled state as expected for (a) seed inhibition at the top electrode interface and (b) domain wall pinning in the bulk. Based on ref [48].*

pulse of 1.7 mHz completely fatigued the PZT within 10 cycles! To further illustrate pulse shape dependencies, low frequency waves (1.7 mHz) with different amplitudes were investigated. It was shown that those waves with amplitudes of E_c fatigued within 18 cycles while those cycled well above E_c showed no fatigue after 100 cycles.

The properties of samples fatigued under low frequency conditions were then compared with samples fatigued under standard conditions (square waves with amplitudes above E_c at tens of kilohertz). Samples fatigued under standard conditions showed C-V curves with reduced peak capacitances but little change in the saturation capacitance. This result indicates a reduced domain wall contribution as would be expected for the seed inhibition model (Fig. 1-15a). Samples fatigued at low frequencies, showed decreased peak capacitances and increases in the saturation capacitance. This result implies a lower extrinsic contribution at switching but a higher extrinsic contribution at saturation—indicative of clamped domains (Fig. 1-15b) [46, 48]. Furthermore, for the films that underwent standard pulsing conditions, piezoelectric measurements gave non-symmetric butterfly loops that indicated a preferential direction of polarization in the fatigued state [46]. This is consistent with the seed inhibition model. Domain wall

pinning would be expected to give a random polarization arrangement that would simply reduce the overall piezoelectric response [46, 48]. A recent investigation contends to have imaged the presence of these seeds near the surface using PFM [47].

In summary, it appears that domain wall pinning may act as a fatigue mechanism when extremely low frequency pulses or other external stresses (UV light, thermal energy) are employed. However, at the current time, strong evidence supports the seed inhibition model for standard fatiguing conditions typically used to investigate ferroelectric lifetime in non-volatile memory-type applications.

1.8 Oxide Dielectric / Base Metal Electrode Compatibility:

The metal / ceramic composite structure of multi-layer capacitors (MLCs) has motivated research into the co-firing of oxide dielectrics with intimately contacted metal electrodes. In 1963, Herbert [50] published the first evaluation of preparing a perovskite dielectric (BaTiO_3) with base metal electrodes (nickel). Although noble metals can withstand high-temperature anneals in air consistent with conventional high-quality dielectric preparation, Herbert recognized that this process would be uneconomical for manufacturing*. However, base metals were traditionally considered incompatible because under standard ceramic processing conditions they would oxidize and/or react with the dielectric, degrading the metal's conductivity or the dielectric's permittivity / resistivity. Herbert proposed that if the stack was co-fired in a reducing environment and the electrode had a lower affinity for oxygen than the dielectric, then oxidized ceramics could be prepared while maintaining the integrity of the base metal electrode [50].

This concept was formalized using thermodynamics to express the exact temperature and oxygen partial pressure regime necessary to afford a thermodynamic equilibrium between the oxidized ceramic constituents and reduced metal electrode. An example of such a phase diagram is given in Fig. 1-16. However, Herbert also recognized that firing ceramics like BaTiO_3 in a reducing environment would increase their

* Herbert noted that Ag could be economical but its melting temperature (961°C) was too low for the sintering of any known high-permittivity dielectric [50].

conductivity, and the intentional addition of an impurity species could improve resistivity [50]. Much research was invested in this problem throughout the 1970s, 1980s, and 1990s. The basic problem is that firing in a reducing atmosphere increases the equilibrium concentration of $V_{O}^{\bullet\bullet}$. Whether electronically compensated (electrons) or ionically compensated (Ti_{Ti}'), these vacancies increase electronic conductivity. Thus, many investigations focused on compensating these oxygen vacancies with acceptor dopants, like Mn_{Ti}' and Ca_{Ti}'' , and improving capacitor lifetime and aging characteristics using rare earth dopants [51-53].

However, MLC technology has predominantly remained focused on integrating base metals with dielectrics within the $BaTiO_3$ family. For example, any extension to the PZT family is unknown to this author. The reason that PZT has not been investigated is probably three-fold. First, as the phase diagram in Fig. 1-16 illustrates, the region of thermodynamic equilibrium for the PZT / Cu or Ni system is constrained by the Pb constituent and is significantly narrower than that allowed for $BaTiO_3$. Thus, controlling the processing conditions for a PZT/Cu stack would be considerably more difficult whereas a PZT/Ni stack is thermodynamically impossible. Moreover, this narrow equilibrium window reduces the maximum thermodynamic driving force for reducing the base metal. The system is further complicated by the volatility of PbO. To achieve a true equilibrium state, it would be necessary to also control the partial pressure of PbO. Thirdly, the faster sintering kinetics expected for a Pb-based system may also create a kinetic limitation to reaching thermodynamic equilibrium. If the dielectric rapidly densifies, then any premature oxidation of the base metal may be difficult to reverse due to the slower diffusion rate expected through a dense ceramic layer.

In spite of these challenges, some attempts have been made to prepare PZT thin films on base metals. In thin films, some of these difficulties are expected to be relaxed due to the faster kinetics and lower processing temperatures associated with a thin film process. However, a PZT film on a base metal with properties comparable to films deposited on noble metals or conductive oxides has yet to be demonstrated.

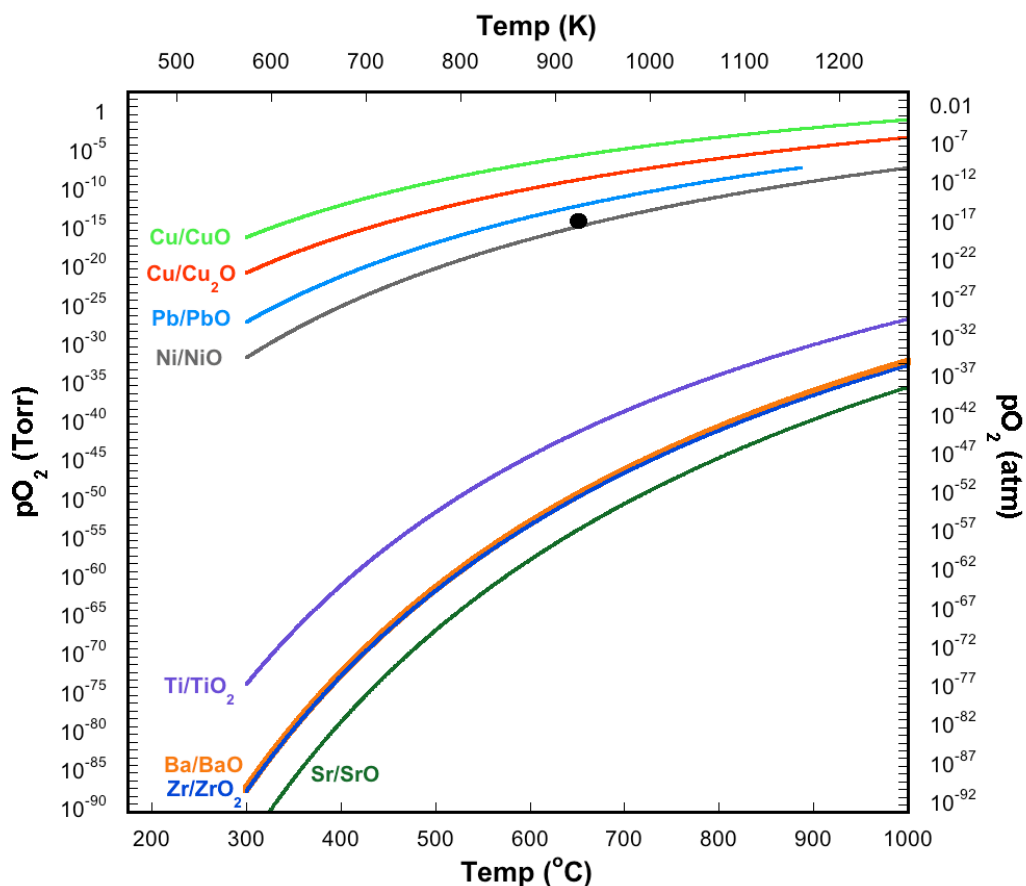


FIG 1-16 – Phase Diagram Showing Elemental Metal / Metal Oxide Stability as a Function of Temperature and Oxygen Partial Pressure: *A phase diagram showing lines of thermodynamic equilibrium between elemental metals and their simple oxides. Oxides are stable above these lines; metals are stable below these lines. The black circle labels the processing conditions investigated in Chapter 4 (650°C / $pO_2 = 1.3 \times 10^{-14}$ Torr) Data was calculated from ref [54].*

1.8.1 (Ba,Sr)TiO₃ Thin Films on Base Metal Substrates:

By adapting the thermodynamic equilibrium processing approach of the MLC industry to thin film technology, researchers have found much success in fabricating films of the (Ba,Sr)TiO₃ family on base metal bottom electrodes such as nickel and copper. Both CSD and sputtered deposited (Ba,Sr)TiO₃ films have been demonstrated to form unreacted interfaces with base metal electrodes when crystallized in a temperature / oxygen partial pressure (pO₂) regime that affords equilibrium between the oxidized perovskite and

unoxidized metal phases [55-60]. To date, a majority of this work has been completed on metal foils, tens of microns thick. Such approaches eliminate delamination problems that may occur between base metals and rigid substrates like silicon or alumina. In addition, these flexible foils expand the application of these films to novel technologies such as flexible electronics [59], large-scale manufacturable capacitors for printed wiring board (PWB) integration [57, 58], and oxide-buffer, crystalline-templates for superconducting tapes [56, 60].

Initial work was reported by Dawley and Clem [55] for (Ba,Sr)TiO₃ thin films deposited directly on <100>-textured Ni foils. Films with compositions of near room temperature T_c displayed relative permittivities of 430 and dielectric tunabilities of 56% at 10 kHz. When processing conditions were modified to induce <100> texturing in the dielectric, these values were improved to ~1500 and 73%. Loss tangents remained below 0.03 under all conditions [55].

Possibly the most impressive electrical properties for BaTiO₃ thin films reported to date are those of Ihlefeld *et al.* [57, 58]. These films were derived from HOAc/acac chelated metal alkoxide solutions, spin-coated on copper foils, and crystallized at 900°C in controlled pO₂ conditions. These BaTiO₃ thin films exhibited zero bias permittivities in excess of 2500 at 10 kHz, dielectric tunabilities of ~85% and loss tangents below 1.5% at high fields. Unlike conventional platinized silicon substrates, which tend to delaminate at high temperatures (>750°C), films processed directly on base metals can be annealed at much higher temperatures. This large thermal budget can allow dramatic grain growth. Thus, the exceptionally large grain sizes (~0.2 μm) observed for these thin films are believed to afford them dielectric properties nearly comparable to traditional ceramic BaTiO₃ materials with similar microstructures [57]. Besides dielectric response, these films also exhibited a pseudo-cubic unit cell and true hysteretic response as expected from a BaTiO₃ ceramic but often not observed for a BaTiO₃ thin film [57, 58].

(Ba,Sr)TiO₃ films have also been prepared by sputter deposition on copper foils [59]. Although crystallized under similar high temperature conditions, these materials exhibited a partially columnar morphology with 55 nm planar dimensions and 500-600 nm

longitudinal dimensions. This microstructure was probably induced by the microcrystalline nature of the as-sputtered films and, combined with the solid solution composition, probably accounts for the lower reported permittivity ($\epsilon \sim 625$). However, due to their conformality and high density, these sputtered films exhibited remarkably small dielectric losses of 0.003 at high fields and greater than 90% yields [59].

1.8.2 PZT Thin Films on Base Metal Substrates:

The earliest demonstration of sol-gel PZT thin films prepared on base metal substrates is probably the 1988 report of Sayer *et al.* [61] who investigated stainless steel plates as a possible substrate for their modified sol-gel PZT solutions. A year later, this group also reported depositing PZT films on wires of a nickel alloy (Alumel) [62]. In 1992, Chen *et al.* [63] at The Pennsylvania State University described results for alkoxide-derived PZT CSD thin films on Ni-Ti shape memory alloy (SMA) foils (0.1 mm thick). These structures were intended to function as a smart material composite that retains and couples the rapid strain response of PZT with the large stress-strain actuation of an SMA. Films were spun directly on the Ni-Ti alloy, pyrolyzed at 400°C, and crystallized at 500°C in ambient atmosphere. The observance of a relaxation event at 2 MHz in the permittivity dispersion spectrum led Chen *et al.* to conclude that this system contains an interfacial layer. Nevertheless, the dielectric constant for these 0.6 μm thick PZT films was reported to be 700 at 100 kHz with a loss of 0.03 and a remanent polarization of 15 $\mu\text{C}/\text{cm}^2$. These films were also reported to maintain their electrical integrity upon a 0.4% strain (2.5 cm diameter mandrel) and subsequent recovery of the SMA. However, films cracked/delaminated when a 0.5% strain was imposed (1.9 cm diameter mandrel) [63].

Work has continued in this area of ferroelectric / SMA smart material heterostructures for use as actuators and vibrational damping devices [64-66]. Because the Ti-Ni alloy must remain below $\sim 540^\circ\text{C}$ to retain its shape memory effect, CSD PZT films deposited on the SMA must be crystallized at relatively low temperatures [65]. However, even when a platinum interfacial layer was employed, remanent polarization of only 14 $\mu\text{C}/\text{cm}^2$ have been achieved [66]. One author claimed to have fabricated PZT directly on

Ti-Ni with no interfacial reactions by XRD but reported a polarization hysteresis “loop” with a remanent polarization of $0.152 \text{ } \mu\text{C}/\text{cm}^2$ [65].

Other work has been ongoing at the University of Toronto [67-71], focusing on the deposition of PZT thin films on titanium, aluminum, nickel, brass, and stainless steel substrates. PZT film preparation generally consisted of spin-coating 2-MOE/acac chelated alkoxide solutions and directly firing in air at $\sim 600^\circ\text{C}$ for 30-60 min. Films prepared directly on these substrates always exhibited interfacial reactions that degraded the dielectric response. For examples, films on Ti and Al showed suppressed permittivities due to series capacitance with a low- ϵ substrate oxide. Films deposited on stainless steel exhibited high dielectric losses, apparently due to Ni and Cr diffusion into the PZT [69, 71]. To date the best ferroelectrics reported by this group were PZT films deposited on titanium and nickel substrates with LaNiO_3 buffer layers. These films exhibited P_r values of $8.5\text{-}14 \text{ } \mu\text{C}/\text{cm}^2$, but were poorly saturated [70].

Maria and co-workers have published work on PZT and PLZT films deposited on electroless nickel plated (4 μm) copper foils for embedded passive applications [72, 73]. These experiments used alkanolamine chelated solutions spin-coated directly on the nickel surface and then pyrolyzed in two steps: 250°C hotplate (ambient) and 450°C tube furnace (air). Films were crystallized between 550°C and 650°C in either flowing nitrogen or under controlled $p\text{O}_2$ conditions in a vacuum furnace. Again, suppressed permittivities and dielectric tunabilities were observed, and a TEM investigation definitively revealed the presence of a $\sim 30 \text{ nm}$ thick interfacial reaction layer [73]. However, from an equivalent circuit analysis, this interfacial layer was determined to be insulating [72]. Annealing $p\text{O}_2$ was found to influence the perovskite/pyrochlore volume ratio, which directly impacted dielectric response. A $p\text{O}_2$ of $\sim 10^{-3}$ Torr was found to be optimum [72]. These films were also demonstrated to have sufficient handleability to undergo the lamination procedures necessary for integration into printed wiring boards [73].

Perhaps the most impressive work of PZT thin films on base metals to date is that of Cheng *et al.* [74] whom deposited a CSD PbTiO_3 seed layer onto stainless steel substrates prior to the deposition of 1.5 to 3.5 μm thick PZT films (2-MOE solutions). The

seed layer allowed for a lower thermal budget (550°C), reducing interfacial reactions. The dielectric constant was still low for this material (<300 at 10 kHz), but this was attributed to large compressive stresses due to thermal expansion mismatches. This conclusion is consistent with the nicely saturated polarization hysteresis loops attained for this material ($P_r = 35 \text{ } \mu\text{C}/\text{cm}^2$). Furthermore, since stress effects created *c domains* with high polarizations and low permittivities, the films displayed excellent piezoelectric response with d_{31} values of up to -76 pC/N [74]. Three main factors contributed to the success of this work. First, stainless steel is designed to resist oxidation. Second, the PZT film was sufficiently thick to be unaffected by any leakage that may have occurred in the PbTiO_3 seed layer due to Fe and Cr infiltration. Third, the lower process temperature minimized undesirable interfacial reactions.

1.9 Statement of Purpose:

This chapter has established ferroelectrics as a technologically important class of materials, with great opportunity available in thin film applications. Currently, a serious limitation to the commercialization of ferroelectric thin film technology is the expense associated with single crystalline substrates and noble metal or conductive oxide electrodes that are conventionally thought to be necessary for fabricating these devices. Recent reports have demonstrated that ferroelectric thin films of the $(\text{Ba,Sr})\text{TiO}_3$ family can be successfully processed on base metal substrates like Ni or Cu through the use of thermodynamic equilibrium conditions. The integration of PZT thin films with base metal substrates is also of interest because it would add a property set complementary to the $(\text{Ba,Sr})\text{TiO}_3$ family. Unfortunately, an equilibrium processing approach is riddled with complications. Most previous approaches have used diffusion barriers or allowed for interfacial reactions to occur, thus demonstrating the difficulty in integrating PZT with a base metal. None of these reports have demonstrated PZT films with dielectric and ferroelectric properties comparable to those commonly reported for PZT thin films deposited on a standard platinized silicon substrate; as such, none of these films can truly compete with the PZT on noble metal / conductive oxide technology.

The purpose of this research effort is to develop a processing route for depositing device-quality PZT thin films directly on copper foils that can match the performance of films deposited on semiconductor-grade single crystal substrates. Besides the economic benefits, copper foils offer the additional advantages of low resistivity, mechanical flexibility, ease in patterning, and compatibility with printed wiring board integration.

To accomplish this goal, a chemical solution deposition (CSD) process is investigated because it matches the ultimate objective of low-cost commercialization and it provides an expansive process window in which to achieve the desired PZT/Cu compatibility. Instead of focusing on an equilibrium approach for achieving oxide/base metal integration, this research is directed by understanding the science of sol-gel chemistry thin film processing and utilizing this knowledge to design a methodology for achieving PZT/Cu compatibility.

2. A Review of Chemical Solution Deposited Ceramic Thin Films

Chemical solution deposition (CSD) has become an important method for preparing multicomponent oxide thin films for both research and commercial applications. Like any processing technique, CSD has both advantages and limitations. For multicomponent films the use of wet chemicals as precursors allows for excellent stoichiometric control as well as the ability to easily examine a range of compositions. Furthermore, CSD processing is commercially attractive because of its low capital cost and compatibility with standard semiconductor fabrication technology [75, 76]. A typically quoted disadvantage is its inability to provide the conformal coverage of a chemical vapor deposition process, limiting the utility of CSD for random access memory applications. (New advancements in mist delivery technology may provide a resolution to these issues but would also dramatically increase the cost associated with the process [77]). Other limitations include difficulty in achieving epitaxial growth, depositing ultrathin films (< 30 nm), and minimizing optical losses [76, 78].

However, perhaps the most important advantage of CSD is also its most serious disadvantage: versatility. The versatility of the CSD process provides extreme adaptability for the control of film composition and microstructure but at the same time presents the challenge of maintaining a robust and repeatable process. Schwartz has also commented on the dichotomy of CSD's versatility acknowledging that a CSD approach contains an extensive amount of process variables, which must be understood and controlled. From an engineering perspective, Schwartz has recommended and employed statistical design of experiment techniques [75, 79]. For this thesis, though, it is more appropriate to gain a scientific understanding of the CSD process and then apply this knowledge to the specific problem of depositing PZT films directly on copper surfaces.

2.1 A General Outline for Processing CSD Thin Films:

The type of CSD thin films relevant to this thesis can roughly be classified as sol-gel in nature. The material begins as a sol—defined as a colloidal suspension of nano-

scale solids in a liquid matrix. Through solvent evaporation and chemical reaction, the monomers within the sol polymerize to form a gel—that is a macroscopic, three-dimensionally connected mass fractal network interpenetrated with a continuous liquid phase. The solid polymeric skeleton gives a gel its elasticity while the liquid phase maintains some compliance, making the gel state viscoelastic. Upon further heat treatment, the liquid phase and residual organics are completely removed, and the material densifies and crystallizes into a ceramic [80].

The CSD of thin films involves four basic steps: (1) solution preparation, (2) solution deposition, (3) low temperature drying and/or organic removal, and (4) high temperature crystallization. Typically, steps 2 and 3 are repeated several times to achieve a desired film thickness prior to crystallization. Each of these steps will be investigated further in subsequent sections.

It is also important to note some fundamental differences between bulk and film sol-gel processing. Sol-gel films generally use solutions of lower concentration, but evaporation typically occurs much more rapidly during deposition. This situation profoundly affects microstructural evolution. Additionally, the severe shrinkage due to solvent removal combined with the mechanical constraints imposed by the substrate can lead to substantial tensile stresses in thin films [81].

2.2 Solution Chemistry:

For the successful fabrication of CSD thin films, certain properties of the solution chemistry must be addressed. A rather complete list of important solution properties, which was originally present by Schwartz *et al.* [78], is summarized in Table 2-1. For this thesis the (#2) solution stability, (#3) phase separation in the gel state, (#5) substrate interaction, (#7) organic removal, and (#8) crack formation will be of particular importance.

Table 2-1 – Requirements for Successfully Synthesizing Thin Films by a Chemical Solution Deposition Process: *List of important considerations in designing a CSD process, based upon ref [78].*

1. Solubility of metalorganic precursors
2. Acceptable long-term stability of solution
3. Minimal phase separation in the sol and gel states
4. Adequate wettability of the substrate
5. Interaction with substrate causes minimal degradation
6. Proper rheology to achieved desired/uniform film thickness
7. Complete decomposition/removal of organic precursors
8. Avoidance of crack formation during solvent evaporation

2.2.1 Precursors and Ligands:

Precursors for metal oxide films are typically metalorganic species*. The two primary types of metal precursors used in CSD thin films are metal carboxylates and metal alkoxides. Metal carboxylates (Fig. 2-1a) are the salts of a metal cation with a carboxylic acid anion (such as acetate) and are commonly used for the A-site perovskite cation. These polar moieties are typically soluble in their parent acid and, if the organic chain is short, will also dissolve in polar solvents such as water. Although metal carboxylates tend to decompose in water, they do not exhibit a tendency to polymerize like metal alkoxides [78].

Metal alkoxides are the salts of metals and alcohols (Fig. 2-1b). These metalorganics are typically used for the B-site cation. The combination of a low electronegativity transition metal with a high electronegativity alkoxide group forces the cation into its highest oxidation state. This situation also makes the M-O bonds highly ionic and very susceptible to attack by water (hydrolysis) [80].

* Metalorganics bond metal cations to organic ligands through an oxygen atom (M-O-C) whereas organometallic species contain metal cations bonded directly to carbon atoms (M-C)—for example: silane [80].

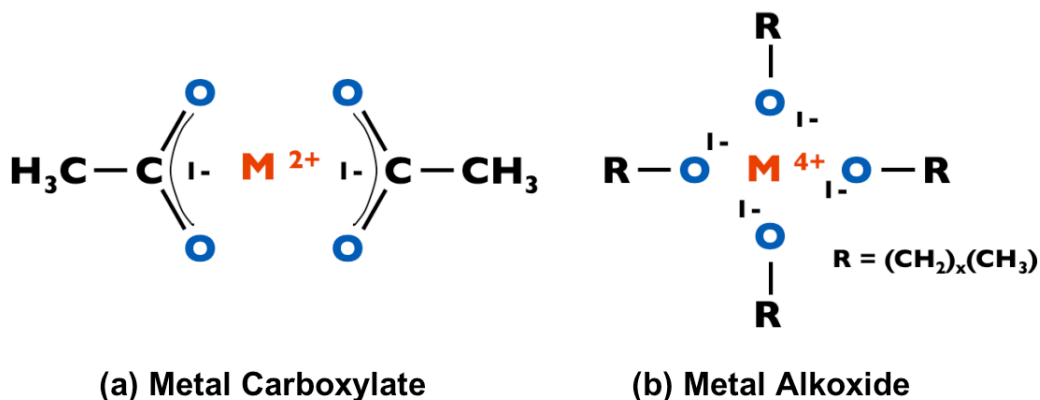


FIG 2-1 – Illustration of Metal Carboxylate and Metal Alkoxide Species: Drawings of metal cations (M) complexed with (a) 2 carboxylic acid groups and (b) 4 alkoxide groups.

The reactivity of metal alkoxides can be reduced in three ways: (1) increasing the size of the alkyl chain, (2) adding polar species to the organic chain, or (3) replacing the alkyl chain with a modifying ligand. If the size of the organic constituent is increased, then steric hindrances can limit the reactivity of the metal alkoxide [80]. The addition of polar species (such as ether linkages in 2-methoxyethanol) serves to create additional polar sites that can further complex the metal cation and increase stability. This process of bonding multiple polar groups of one organic chain to the same metal cation is known as *chelation* [78]. Such modifications to the organic chain can be designed into the original precursor, or a modifying ligand such as a carboxylic acid or a β -diketonate can be added to the solution to replace the alkoxide chain. Two common examples are the carboxylic acid, acetic acid (HOAc), and the β -diketonate, 2,4-pentanedione (acetylacetone or acac). The acetate ion can act as a bridging ligand (see Fig. 2-2a) while acac (see Fig. 2-2b) typically acts as a non-bridging ligand (true chelating agent) with a bidentate complexation (bonds with both oxygens) [82]. The acac ligand provides a lower reactivity metalorganic due to its non-bridging nature and the high stability established by the electron delocalization in the 6-member ring [78].

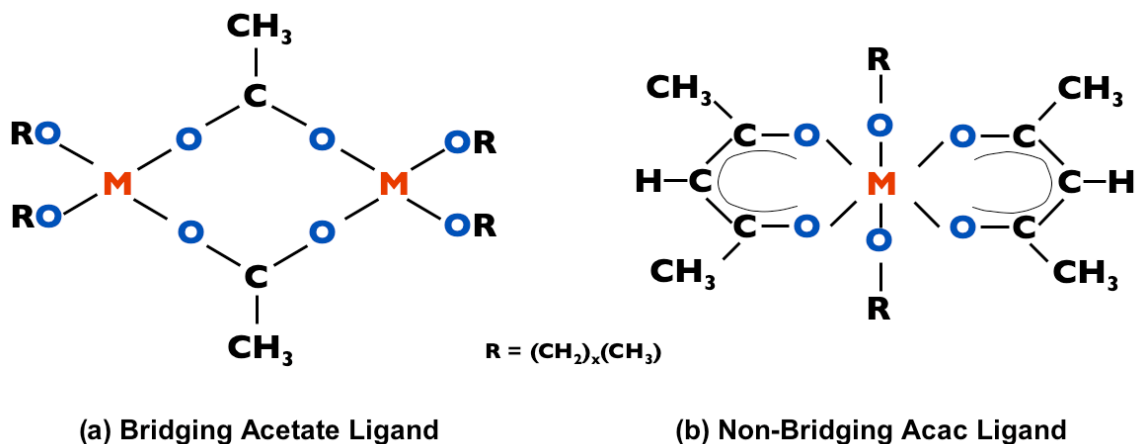


FIG 2-2 – Depiction of a Bridging Ligand Versus a Non-Bridging Ligand: *Drawing of metal cations chelated with either (a) a bridging acetic acid ligand or (b) a non-bridging acac ligand.*

2.2.2 Methods for Solution Preparation:

Three basic classes of solution chemistry exist: (1) metalorganic decomposition (MOD), (2) sol-gel, and (3) hybrid sol-gel. Although the hybrid sol-gel process will be of primary interest for this thesis, the former two will also be briefly summarized.

Metal Organic Decomposition – In MOD, metalorganics with large carboxylate groups are dissolved stoichiometrically in a common non-polar solvent such as xylene. The precursors' large organic groups make these species non-reactive due to steric considerations. Thus, the final solution is a simple mixture that is insensitive to hydrolysis and straightforward to prepare. The gel-to-ceramic conversion simply requires the decomposition of the large organic ligands. However, this substantial removal of organics results in significant weight loss and volume shrinkage that can easily lead to cracking. Additionally, the lack of precursor reactivity reduces the solution's versatility and limits the control over eventual film microstructure [75, 78].

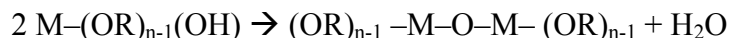
Sol-Gel – In a true sol-gel process, metal alkoxides are dissolved in a single solvent, and precursor structures are engineered by controlling the hydrolysis, alcohol exchange, and condensation reactions. Water drives the *hydrolysis* reaction, replacing a ligand with a highly reactive hydroxyl group (-OH):

Hydrolysis

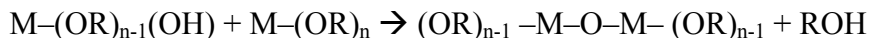


where M is the metal and R is an alkyl group/chain. This hydroxyl group will then readily react with either another hydroxyl or an alkoxide ligand in a *condensation reaction* forming an M-O-M bond:

Condensation By Water Elimination

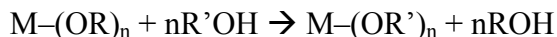


Condensation, By Alcohol Elimination



Additionally, the solvent, which is typically 2-methoxyethanol (2-MOE or CH₃OCH₂CH₂OH), can often act as a chelating agent through an alcohol exchange process:

Alcohol Exchange



forming a metal methoxyethoxide that is less susceptible to hydrolysis. By controlling these reactions through refluxing, distillation, and water additions, precursor oligomerization can be engineered and excellent solution stability can be achieved. Unfortunately, this process is time intensive (1 to 2 days to make a solution) and the procedural sophistication can be overwhelming for the non-chemist. Additionally, 2-MOE is known to cause birth defects and is often avoided in manufacturing facilities [75, 76, 78].

Another solvent used in sol-gel preparation of perovskite materials has been 1,3-propanediol, which, unlike 2-MOE, acts as a bridging ligand. This effect results in larger, more cross-linked oligomeric species, which then leads to thicker films. Films with thicknesses of 0.5 μm to 1 μm can be reached in a single deposition step using this solvent [78].

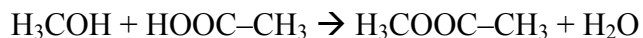
Hybrid Sol-Gel – Hybrid sol-gel solutions combine characteristics of MOD and pure sol-gel methods. These solutions typically use both carboxylate and alkoxide precursors [83]. The metal alkoxide species are purposely stabilized against hydrolysis by exchanging the alkoxide complex with a modifying ligand or chelating agent. Common chelating agents for metal alkoxides used in solutions for ferroelectric thin films include acetic acid, acetylacetonone (acac), and diethanolamine. These chemicals undergo a reaction similar to alcohol exchange:

Precursor Chelation with HOAc



Unlike a true sol-gel process, the metal alkoxides are reacted directly with the chelating agent and then diluted in a common solvent such as an alcohol or a carboxylic acid. This immediate chelation lowers precursor sensitivity to hydrolysis, allowing the solution to be handled in ambient air. Water may also be added to impart solution stability by equilibrating the hydrolysis reaction. However, chelated solutions tend to exhibit continued reactivity, leading to serious solution aging effects that can degrade film properties [78]. Aging in these solutions can be partially explained by continued esterification reactions that occur between carboxylic acids and alcohols in the solution. These reactions create excess water and an ester:

Esterification between methanol and HOAc



Although solution synthesis is relatively straightforward (1 to 2 hours of preparation), the actual chemical reactions can be much more complex than traditional sol-gel chemistry. Hence, control over precursor structure is diminished [75, 76, 78].

During gellation, these solutions form M-O-M bonds through hydrolysis and condensation pathways similar to those discussed for traditional sol-gel solutions. However, the decomposition routes for chelating agents can differ from those of alkoxides or 2-MOE, creating unique opportunities for controlling organic removal and film microstructure [76].

2.3 Film Deposition:

Film deposition is accomplished using three basic methods: (1) mist delivery, (2) dip-coating, and (3) spin-coating. Although uncommon, mist deposition offers an opportunity for conformal thin film deposition from a CSD process on non-planar substrate architectures. In the liquid source misted chemical deposition (LSMCD) process, a nebulizer converts the liquid precursor into an aerosol that is transported to the substrate via a carrier gas [77]. Deposition rates for this process have been enhanced with the implementation of electric fields to accelerate charged droplets [84]. However, processing thicker ($> 0.3 \mu\text{m}$) films remains time intensive due to minimal drying/consolidation of the gel during deposition [85]. LSMCD has also been hampered by the necessity for constant cleaning of delivery lines [77].

In dip-coating the substrate is immersed vertically in the solution and removed at a constant rate. This process has been divided into five stages: immersion, start-up, deposition, drainage, and evaporation [86]. Some overlap exists between these stages, especially with regards to evaporation. A combination of multiple forces (including gravity, viscous drag, surface tension, and inertial forces) determines the final film thickness. Calculated and experimental observations [80] have shown that thickness (t) has the following relation with substrate speed (U) for most systems:

$$t \propto U^{2/3} \quad [\text{Eqn. 2-1}]$$

For spin-coating, the substrate is flooded with solution and then spun at 1000-8000 rpm using a standard photoresist spinner with a vacuum chuck holder. The spin coating process has four basic stages: deposition, spin-up, spin-off, and evaporation. During spin-up the solution is dispensed radially due to inertia, and during spin-off excess solution flows off the edges. As the film gets thinner, its resistance to flow increases, and evaporation becomes the primary mechanism for subsequent shrinkage. Evaporation also removes solvent, increasing film viscosity and driving film consolidation [80]. Film thickness is thus determined by spin speed, solution viscosity, and solution concentration [78]. Although this process is predicted to give a uniform film thickness for Newtonian fluids, sols are often thixotropic leading to a radial decrease in thickness that is congruent with the radial increase in shear [80]. The shearing forces in spin-coating can also act as a driving force for consolidation prior to gellation, especially for large, compliant, non-branched precursors. Experimentally, the refractive index (or film density) has been shown to increase with increased spin speed [81].

2.4 Gellation:

Following deposition, films often fall into one of three categories: (1) chemical gels, (2) physical gels, or (3) non-gelling films [78]. Solvent evaporation drives gellation by shrinking the film and forcing precursor species to interact. Thus, non-gelling films are usually only observed in systems with non-reactive precursors and low volatility solvents (mostly MOD processes). Physical gellation is the aggregation of oligomeric precursors through van der Waals or steric interactions. These films can be redissolved in the parent solvent. Chemical gellation, in sol-gel chemistries, occurs through the formation of a macroscopic M-O-M skeletal network via hydrolysis/condensation reactions. Such films are insoluble in the parent solvent [78]. EXAFS (extended x-ray absorption fine structure) studies by Sengupta *et al.* have revealed that PZT gels usually consist of separate M-O-M networks for the B-site and A-site cations respectively [87].

Gellation behavior has a strong impact on film consolidation. Because physical gels are only weakly constrained, low temperature heat treatments can further consolidate the film prior to chemical gellation [78]. However, the extent of consolidation is dependent on the transparency or opacity of the oligomeric or polymeric species present. When brought into proximity, two transparent species will interpenetrate while two opaque species will remain separated [80]. In general, opacity increases as species become more branched (sterically hindered) and/or more reactive (more likely to form M-O-M bonds). As an example, acid catalyzed gels will form linear chain oligomeric precursors [80]. This precursor geometry is transparent and provides for substantial structural rearrangement during gellation. This transparency results in a dense, low porosity gel. If the pH is raised to catalyze precursor branching or if water is added to drive hydrolysis, then precursors become more opaque and the gel network forms before full consolidation. The final gel structure is more porous and of lower density than the acid catalyzed condition [88].

Another way to approach the issue of consolidation is to model the gel network as a mass fractal. Unlike Euclidean shapes (like a sphere), mass fractals exhibit dilational symmetry—that is a magnified portion will look identical to the original structure [81]. Examples of such symmetry are found in nature—for instance heads of broccoli or trees. This symmetry creates a unique mass (m) dependency on mass fractal size (radius $\sim r$):

$$m \propto r^{D_f} \quad [\text{Eqn. 2-2}]$$

where D_f is the mass fractal dimension and describes the amount of branching [80]. For simple Euclidean shapes, $D_f = 3$ while for mass fractals, $D_f < 3$. Thus, if one considers the density of a shape to be $\rho = m/r^3$ then it can be concluded that density is constant for Euclidean geometries while density decreases with mass fractal size [80]. Note that a smaller D_f corresponds to a greater decrease in density. This dimension can be obtained experimentally through small angle x-ray scattering (SAXS) experiments [89].

If gelled species are capable of redissolving, then it is possible to create an equilibrium gel network, which minimizes surface area and has a Euclidean shape.

However, for most metal alkoxide gels where condensed M-O-M species are not redissolvable in the gel's liquid phase, mass fractal network geometries develop [80]. An important relationship for the interaction between two of these mass fractal species is given by Mandelbrot [90]:

$$M_{1,2} \propto r^{D_{f1}+D_{f2}-d} \quad [\text{Eqn. 2-3}]$$

where $M_{1,2}$ is the number of intersections between mass fractal 1 and 2, D_{f1} and D_{f2} are the respective mass fractal dimensions, and d is the dimension of space ($d = 3$ for 3D situations). This equation reveals that for weakly branched species, in which $D_{f1} + D_{f2} < 3$, the amount of intersections will decrease with increasing size—implying transparency and film consolidation. Conversely, if $D_{f1} + D_{f2} > 3$, then the species will strongly interact leading to opacity and poor consolidation. Larger oligomers will increase porosity concentrations due to the density behavior of mass fractals [81]. However, this interaction probability assumes rigid networks and perfect sticking probabilities. Both of these factors can be manipulated in real sol-gel systems particularly by chelation chemistry and solution pH [81].

2.5 Drying of Gels:

Drying, which is the process of removing liquid from the gel, is primarily driven by evaporation of the solvent at the exterior surface. Once dried, the remaining solid skeletal network is known as a xerogel [80]. A closely related mechanism for removing liquid from the gel is syneresis. Syneresis occurs when the network contracts due to condensation reactions, expelling liquid from the interior. This process is driven by the desire to reduce solid-liquid interfacial energy (σ_{sl}); thus, unlike drying, syneresis can occur in a closed system (where evaporation is prevented) [80, 91]. The linear contraction associated with syneresis (~10%) is typically significantly less than that associated with evaporation (50-70%). Syneresis is used in bulk sol-gel processes during aging to influence the elastic modulus and rheology of the gel upon drying [92]. However, as

already mentioned, sol-gel thin films undergo immediate evaporation during conventional spin-coating and dip-coating processes. Consequently, syneresis will typically not impact thin film processing behavior.

In the drying process, evaporation of the liquid phase leaves behind solid/vapor interfaces that have higher energy than the prior solid/liquid interfaces ($\gamma_{sv} > \gamma_{sl}$). Initially, capillary pressure will force liquid to flow from the saturated interior to cover the exposed exterior regions to minimize this interfacial energy. The energy released (ΔE) by replacing this interface is given by:

$$\Delta E = 2\pi ah(\gamma_{sl} - \gamma_{sv}) \quad [\text{Eqn. 2-4}]$$

where a is the radius of the pore and h is the height that the liquid rises. The work done by the rising liquid in these pores is simply $P_c \Delta V$ where P_c is the capillary pressure and $\Delta V = \pi a^2 h$. By equating these energies (ΔE with $P_c \Delta V$):

$$P_c = -\frac{2(\gamma_{sv} - \gamma_{sl})}{a} = -\frac{2\gamma_{lv} \cos(\theta)}{a} \quad [\text{Eqn. 2-5}]$$

where P_c is simplified using Young's equation ($\gamma_{sv} \cos(\theta) = \gamma_{sv} - \gamma_{sl}$) and θ is the contact angle [92]. Physically, the liquid is being stretched from the saturated interior towards the unsaturated exterior. This situation has two important consequences. First, it sets up the pressure gradient (ΔP) that drives the flow of the liquid as is described by Darcy's Law:

$$J = -\frac{D}{\eta_L} \nabla P \quad [\text{Eqn. 2-6}]$$

where J is the flux of the liquid, η_L is the viscosity of the liquid (Pa·s), and D is the permeability of the solid network (m^2) [93]. Second, the tensile stress of the stretched liquid places the solid network into compression, which drives shrinkage of the gel [92].

During the first stage of drying, known as the constant rate period, the gel network is compliant enough to fully contract into the liquid in response to the capillary pressure. Thus, the surface remains fully saturated and the rate of evaporation is constant. (In fact, the evaporation rate approaches that observed for the pure liquid in an open environment.) However, as the gel continues to consolidate, condensation occurs, stiffening the network. To maintain network contraction, capillary forces must increase. Capillarity reaches its ultimate pressure when the radius of the meniscus equals the radius of the pores. Beyond this point, known as the critical point, the capillary forces can no longer overcome the modulus of the network, and the liquid begins to recede into the solid network [80]. Past the critical point, the shrinkage rate is dramatically reduced and further solvent removal manifests as porosity in the xerogel [81].

2.5.1 Drying Stresses and Cracking in Bulk Sol-Gel Systems:

The amount of shrinkage prior to the critical point is determined by the magnitude of the maximum capillary pressure (P_R). The maximum capillary pressure can be described by:

$$P_R = - \frac{\gamma_{lv} \cos(\theta) S_p}{V_p} \quad [\text{Eqn. 2-7}]$$

where S_p/V_p is the surface area to volume ratio of the empty pore region [80]. This relationship indicates that the capillary force and the consolidation will increase with increasing surface energy (γ_{lv}) and decreasing pore size (S_p/V_p). This pressure can reach 3 to 200 MPa in alkoxide gels, which may lead to cracking. A possible solution is to add surfactants to the liquid to reduce γ_{lv} and subsequently P_R [80].

The process of drying itself may also lead to cracking. Consolidation in the bulk lowers the permeability of the network. Hence, flow from interior to exterior is reduced via Darcy's Law. As a result a larger pressure gradient develops that places the surface region under significantly more compressive stress. The result is that the exterior will

contract more than the interior resulting in a macroscopic tensile stress on the gel's surface [94]. Such a tensile stress can be sufficient to drive crack propagation.

The basic approach to reduce drying cracks is to homogenize the contraction process throughout the thickness of the gel. One method is to retain large pore sizes. Large pores lower the capillary stress (S_p/V_p decreases) while maintaining network permeability and continual fluid flow. Unfortunately, large pores can lead to subsequent difficulties in sintering [80]. Another approach is to incorporate two liquids with different volatilities (for example, water and an alcohol). In this case, the volatile phase will evaporate much faster at the surface setting up a concentration gradient. Thus, even if the frictional forces imposed by small pores restrict *fluid flow*, the *diffusional flux* may be sufficient to maintain a homogeneous contraction [94]. A final approach is supercritical drying, where the gel is taken above the liquid's critical temperature and pressure. In this thermodynamic phase regime, no distinction exists between the solid and liquid phase. Consequently, the liquid exerts no capillary pressure because the liquid-vapor interface is non-existent. Gels processed by supercritical drying undergo negligible contraction, so the dried state, known as an aerogel, is nearly the same volume as the wet gel [80].

2.5.2 Drying in Thin Film Sol-Gel Systems:

Although the same factors (like capillary pressure, evaporation, permeability) influence the drying behavior of thin films, the situation is dramatically different than in bulk drying. For bulk systems, gellation, aging, and drying occur sequentially. Slow evaporation rates are required to prevent cracking and the entire process can take months. The consequence of slow processing is that significant condensation occurs and stiffens the gel at an earlier stage of drying. Subsequently, gellation is completed prior to the end of drying and the bulk xerogel will contain a network of porosity [80, 81].

For spin-coated or dip-coated sol-gel films, the processes of gellation and drying overlap one another, and drying is completed within a few seconds. The rapid rate of evaporation in films allows drying to be completed prior to gellation because the oligomeric species have insufficient time to react. In some cases, the film may not

chemically gel at all and remain a simple physical aggregation. Because the network remains compliant during drying, evaporation and capillary forces can drive significantly more gel consolidation in films as compared to bulk. It is even possible for the pores to collapse [81]. Often, film gels exhibit smaller pores that are more likely to be trapped in the interior than bulk gels. The viscosity of the gel network may also kinetically limit porosity reduction. In addition, subsequent removal of remaining organic ligands can create new porosity [81].

Surprisingly, although the small pores of a film can create capillary stresses in excess of 100 MPa, films below 0.5 μm rarely crack during deposition drying.* To understand this behavior, it is necessary to examine the energies associated with crack propagation. The energy release rate for crack propagation is proportional to the thickness of the film [80]. Below some critical thickness (t_c), crack propagation will be unfavorable:

$$t_c = \left(\frac{K_{IC}}{\sigma W} \right)^2 \quad [\text{Eqn. 2-8}]$$

where K_{IC} is the critical stress intensity, σ is the applied stress, and W is a factor describing the relative elastic moduli of film and substrate [95]. One approach to increase film thickness is to reduce the elastic modulus of the gel. Chelating with non-bridging multidentate ligands such as β -diketonates or reducing the rate of hydrolysis can accomplish this goal [81]. Solvent selection can also influence the maximum film thickness since surface tension determines the amount of stress applied by capillary pressure [78].

The microstructure (porosity, pore size) of a dried gel film is determined by the relative rates of evaporation (which drives network compaction) and condensation (which stiffens the network) [80]. Thus, dense xerogel films will form when evaporation/condensation rate ratios are high. Evaporation is primarily controlled by solvent selection. However, adjusting the partial pressure of the solvent over the drying film can also affect evaporation rates [80]. Condensation is controlled by the transparency

*This discussion pertains to the drying that occurs during deposition and not the drying/organic removal process that is often carried out on a hotplate.

of the precursors. Branched precursors (base-catalysis) impinge and create large porosity that reduces capillary pressure and consolidation. In accordance with the mass fractal character of precursors, increased branching lowers gel density (more porosity) [81]. Aging the solution also affects precursor structure. As the solution ages, precursors become larger and/or more branched, which then can lead to increased porosity [81]. The addition of water is of particular interest. It can, to some extent, increase consolidation because of its high surface tension. However, water also promotes hydrolysis, which then leads to network stiffening. Thus, depending on the conditions, water additions have been observed to both increase and decrease porosity (dip-coating [81] and spin-coating [96]).

2.6 Organic Removal from Gelled Thin Films:

Two types of organics must be removed from the gel prior to crystallization: solvent molecules entrapped in pores and organic ligands attached to metallic species. Reactions that occur during organic removal can be classified in four basic categories: thermolysis, pyrolysis, dehydration, and oxidation. In thermolysis, thermal energy is used to decompose organics and remove volatile species. Pyrolysis reactions occur when organics and O_2 undergo combustion to form volatile species like CO_2 and H_2O . Dehydration is the removal of hydroxyl species (-OH) as H_2O through condensation reactions. Oxidation occurs when intermediate metal carbonate phases ($M-O-CO_2$) form. The carbonates can then decompose into $M-O$ bonds and CO_2 [78].

Two basic regimes exist in organic removal. In the low temperature regime ($\sim 25^\circ C$ to $\sim 150^\circ C$), physical desorption of solvent molecules occurs. Thus, this regime is marked by significant weight loss but minimal shrinkage in the gel's volume. At slightly higher temperatures ($\sim 150^\circ C$ to $\sim 500^\circ C$), a gel is observed to undergo approximately equivalent fractions of weight loss and volume shrinkage. In this regime, weight loss occurs by further solvent removal coupled with ligand elimination via condensation reactions. However, ligand removal via condensation provides an equivalent amount of volume shrinkage. In addition, the gel can structurally relax, leading to further volume shrinkage.

Above about 400-450°C, organic removal is essentially complete and no further weight loss is typically observed [80].

Unlike processing bulk gels where this removal occurs during the ambient temperature drying step and the final gel-to-ceramic heat treatment (1-step process), thin film processes often include a heat treatment step, usually on a hotplate, designed for organic removal (2-step process). If films are processed in a single heating step, a rapid thermal annealer (RTA) is typically used to quickly reach the annealing temperature. This 1-step process involves complex, overlapping pathways of organic removal, densification, and crystallization. However, because the gel remains viscous to high temperatures, cracking can often be avoided during organic removal. Furthermore, this viscous state usually enhances densification prior to crystallization. In the 2-step approach, a low temperature (200°C – 400°C) step is used to remove organics prior to the crystallization step. This intermediate step is often performed on a hotplate because it provides immediate heating and removes organics prior to the collapse of the gel network. Thus, cracking can often be avoided. The 2-step approach is often used to avoid cracking issues when depositing thicker ($>0.5 \mu\text{m}$), multi-layer films. Engineering precursors to maintain their transparency and viscoelastic nature throughout the organic removal temperature regime, can also aid in avoiding cracking associated with shrinkage [78].

Finally, it is important to emphasize that organic removal can produce trapped porosity. If an organic removal process does not have an associated shrinkage mechanism, then the space left by the organic species can become a pore [80]. This effect has been observed in PZT films with 2-MOE chemistry that have been acid-catalyzed [97]. Acid-catalyzed gels have been shown to rapidly consolidate, which can lead to significant amounts of entrapped organics. The eventual removal of these organics has been observed to lead to cracking or porosity in the crystalline ceramic. Base-catalyzed gels have a characteristically more open, networked structure, which allows for the rapid and total removal of organics prior to crystallization. This gel network must also undergo significant structural rearrangement prior to crystallization, which further delays crystallization and aids in densification [97].

2.7 Crystallization of Gels:

The gel-to-ceramic conversion is typically described as a traditional nucleation and growth process that occurs in the amorphous gel. As shown in Fig. 2-3, the driving force for nucleation (ΔG_v) is the difference in free energy between the gel state and the crystalline solid. Note that the gel has higher free energy than the corresponding undercooled liquid because of its larger surface area, hydroxyl content, and free volume [78]. Additionally, a gel is a truly unstable state, not metastable, and is only inhibited from crystallization because of slow kinetics [80].

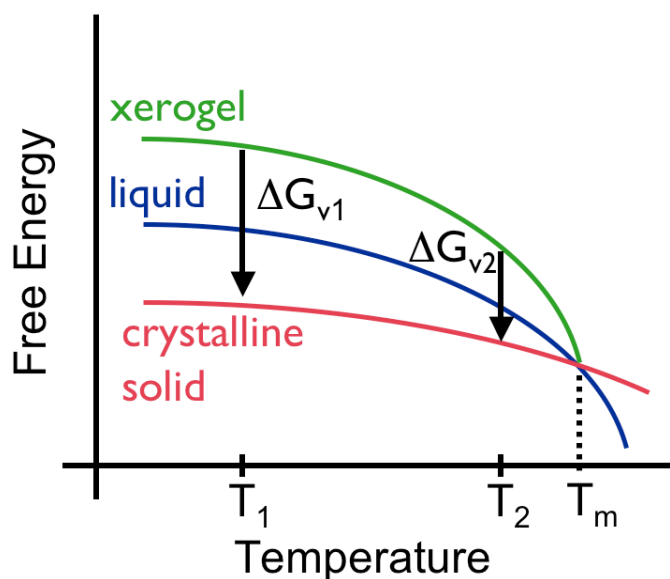


FIG 2-3 – Illustration of the Driving Force for Gel-to-Ceramic Conversion as a Function of Temperature: *Depiction of the free energies for the xerogel, super-cooled liquid, and crystalline solid states of a material. The free energy driving force (ΔG_v) for crystallite nucleation from the xerogel state is labeled for two different temperatures, where $T_2 > T_1$. Based on ref [98].*

2.7.1 The Application of Classical Nucleation Theory to Sol-Gel Systems:

The barriers to nucleation in the gel state can be described by classical nucleation theory. The thermodynamic barrier to homogenous nucleation of spherical nuclei is given by:

$$\Delta G_{Homo}^* = \frac{16\pi\gamma^3}{3(\Delta G_v)^2} \quad [\text{Eqn. 2-9}]$$

where γ is the interfacial energy. Similarly, the barrier to heterogeneous nucleation is:

$$\Delta G_{Hetero}^* = \frac{16\pi\gamma^3}{3(\Delta G_v)^2} f(\theta) \quad [\text{Eqn. 2-10}]$$

where $f(\theta)$ describes the reduction in interfacial energy as a function of contact angle θ :

$$f(\theta) = \frac{2 - 3\cos\theta + \cos^3\theta}{4} \quad [\text{Eqn. 2-11}]$$

An analysis of these functions reveals that the absolute difference between the barriers to homogeneous nucleation and heterogeneous nucleation ($|\Delta G_{Homo}^* - \Delta G_{Hetero}^*|$) decreases with greater undercooling because the increasing driving force (ΔG_v) dominates the barrier heights [98]. This result implies that if crystallization begins at lower temperatures, homogeneous and heterogeneous nucleation will be equally favorable. However, if the onset of nucleation is delayed to temperatures closer to the melting temperature, the difference in the barrier heights is significant and will lead to predominantly heterogeneous nucleation events. Various mechanisms may contribute to delaying the onset of crystallization such as intermediate phases, chemical stability of precursors, and heating rates [78].

2.7.2 Competition Between Sintering and Crystallization:

During the final high-temperature processing step used for gel-to-ceramic conversion, a critical competition occurs between densification (sintering) and crystallization. Crystallization is driven by the need to form a thermodynamically favorable phase while densification is driven by the need to reduce interfacial energy by eliminating solid-vapor interfaces (porosity). From traditional powder processing, it is understood that finer powder sizes densify more effectively [99]. Similarly, it is the unconventionally large surface area (related to the mass fractal nature of the network) and small pore sizes that allow xerogels to sinter orders of magnitude faster and at lower temperatures than conventional ceramics. Concurrently, if crystals begin to nucleate, then similar kinetic considerations will drive rapid grain growth [80]. Densification problems arise when the grains impinge upon one another to form a semi-rigid network (percolation threshold) prior to reaching full density. At the percolation threshold, rapid sintering mechanisms are eliminated and densification is effectively halted [100]. Because xerogels begin with such a low density, if the percolation threshold is reached too rapidly, then large porosity will likely remain in the final ceramic body.

Unlike conventional ceramics, which rely primarily on sintering processes for densification (diffusion, viscous flow, evaporation-condensation, and plastic deformation [99]), xerogels may also densify by capillary contraction, structural relaxations, or condensation reactions [101]. Furthermore, the sintering of xerogels is more likely to occur by viscous flow (densification goes as $\Delta V/V \sim t$), which densifies the body more rapidly than diffusional processes ($\Delta V/V \sim t^{2/5}$) that occur in the crystalline state [80, 99]. Capillary contraction occurs when adsorbed solvents desorb from the pore surfaces. This changes the surface energy and creates a capillary pressure, which can act to densify the network. Structural relaxation is driven by the need to reduce free volume. Free volume can be described as the excess volume an atom has beyond its necessary volume required for thermal vibrations. Materials with large free volume have great latitude in their structural mobility (low viscosity), and when above the glass transition temperature these systems structurally relax towards a lower free volume state that is equilibrated with the

metastable liquid phase of that temperature [80, 101]. Further condensation reactions, which replace hydroxyl (-OH) and unreacted ligand (-OR) groups with smaller M-O-M structures, also act to densify the network. Work by Brinker *et al.* indicates that in general capillary contraction is important at low temperatures (below $\sim 150^\circ\text{C}$), structural relaxation and condensation dominate at intermediate temperatures (between $\sim 150^\circ\text{C}$ and $\sim 525^\circ\text{C}$), and viscous sintering occurs at high temperatures (above $\sim 525^\circ\text{C}$) [101].

To understand the effects of heating rate on densification, let us first examine the idealized case where a xerogel is converted to a non-crystalline solid (glass). Brinker *et al.* have demonstrated that as the heating rate is increased, a lower density, less-crosslinked gel will be attained at the sintering temperature. Because high heating rates give less time-at-temperature, less structural relaxations will occur in the network. However, the structure now has more free volume (higher fictive temperature) at the sintering temperature, and thus will exhibit lower viscosity and a faster viscous sintering rate. This thermal history dependence of the viscosity can in fact compensate for the lower initial density. Hence, densification is commonly observed to show no heating rate dependence for gel-to-glass systems [101].

However, as already mentioned, crystallization can complicate this idealized situation because viscous flow sintering is halted at the percolation threshold. Thus, for efficiently achieving maximum density in gel-derived ceramics it is prudent to fully sinter the body prior to crystallization. One approach for accomplishing this goal is to use conventional Time-Temperature-Transformation (TTT) diagrams in conjunction with densification curves [102]. This allows one to design a ramp rate that will fully densify the structure prior to the onset of crystallization (Fig. 2-4).

Finally, it is important to examine which variables can affect the relative rates of sintering and crystallization. For instance, viscosity affects both sintering and crystallization rates similarly such that changes in viscosity do not improve density. In contrast, pore size has a strong influence on viscous sintering rates ($dr/dt \sim 1/r_0$ where r_0 is initial pore size, [99]) but negligible impact on crystallization kinetics. Thus, by

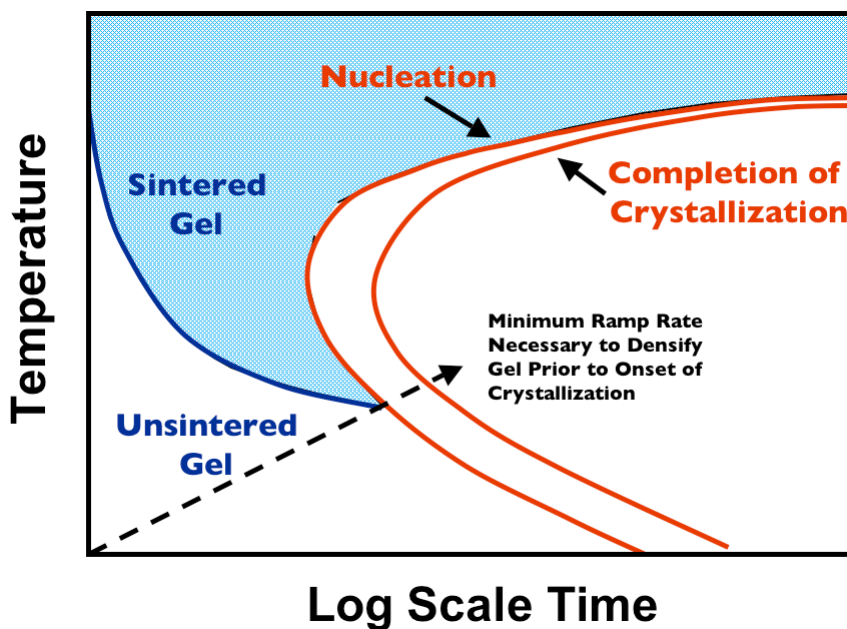


FIG 2-4 – Representative Plot Combining TTT Diagrams with Sintering Kinetics to Optimize Sol-gel Annealing Conditions: *The combination of a time-temperature-transformation diagram and gel sintering rate plot is shown to illustrate an approach for optimizing the crystallization anneal ramp rate such that sintering is complete prior to the onset of crystallization. Based on ref [80, 102].*

controlling the gel microstructure and forming small pores, sintering kinetics can be enhanced preferentially to crystallization. Additionally, care must be taken that impurities are not introduced into the gel (dust, etc.) because these can act as heterogeneous nucleation sites and increase crystallization kinetics [80].

2.8 Examples of Applying Sol-Gel Science to Real Thin Film Systems:

This section focuses on some examples from the literature where investigators carried out elegant experiments that correlate the previously discussed theory with the behavior of relevant sol-gel thin film systems. Examples of TiO_2 and ZrO_2 films are used because of their simplicity (single metal oxides) and relevance to the PZT system. These transition metals are believed to create most of the M-O-M network within PZT gels and

are expected to give insight into the behavior of the PZT system. Section 2.9 will discuss the specifics of CSD PZT films.

2.8.1 Influence of Precursor Chemistry on ZrO₂ and TiO₂ Films:

Investigations by Schwartz and colleagues of CSD ZrO₂ and TiO₂ films were undertaken to examine the influence of chelation chemistry on gel densification and resulting microstructure [82, 103]. Two general solution chemistries were examined: acetic acid chelated solutions and acac chelated solutions. The nature of the gel (physical vs. chemical) was investigated by solvent re-dissolution. Acac gels dissolved readily, indicating their physical gel nature, while HOAc gels were insoluble immediately after spinning, indicating a truly cross-linked M-O-M gel structure. All gels became insoluble with a 200°C hotplate dry, indicating that this heat treatment activated consolidation, which promoted condensation [103].

Directly after spinning, acac-modified films were less dense than HOAc modified films. The steric hindrance of the acac ligand is believed to limit the initial consolidation of the films [82]. However, because the acac ligand is sufficiently transparent (contains non-bridging ligands), acac-modified gels displayed higher rates of consolidation when dried at room temperature [82, 103].

Upon heat-treatment a similar trend was observed. Acac-modified zirconia films exhibited densities of ~95% compared to the ~88% density of an HOAc chelated zirconia film. TiO₂ films only showed a 3% difference in density, but this was attributed to the use of the less reactive butoxide ligand for Ti precursors as compared to the isopropoxide ligand used for zirconia films. Further investigation revealed that acac-modified ZrO₂ films retained a significant organic fraction (40%) at 650°C, while organics in HOAc-modified films were completely removed by this temperature. Thus, by 700°C the HOAc films were observed to be crystalline and had stopped densifying while acac-modified films retained their amorphous structure and continued to sinter by viscous flow [82]. The heating ramp rate was shown to influence densification behavior. As expected, faster ramp rates produced denser films; this effect was most dramatic for acac modified ZrO₂

films—for a 700°C anneal, a density of 81% was reached with a 5°C/min rate compared to 88% density when the film was inserted directly into the hot furnace. This density was increased further (96%) when ramp rates of 3000°C/min were achieved using a rapid thermal annealer (RTA) [103]. The addition of H₂O to the TiO₂ solution decreased film consolidation by increasing the condensation rate. The final film density was reduced from 88% to 81% [82]. Interestingly, the use of low temperature pyrolysis steps (200-300°C) were also found to decrease the final density of ZrO₂ films, presumably because of increased M-O-M bonds and lower organic fractions in the green body [103].

2.8.2 Densification vs. Crystallization Kinetics in TiO₂ Films:

Keddie and colleagues investigated the influence of heating rates on the competition between densification and crystallization in TiO₂ films derived from ethoxide precursors [100, 104]. Again, films processed under faster heating rates exhibited higher densities. (In contrast, Keddie *et al.* also prepared amorphous SiO₂ films. No rate dependency was observed in this system, as is expected for a non-crystalline ceramic.) Hydrogen content was also observed to decrease with increasing heating rates. This is believed to be a self-perpetuating process of densification driving condensation driving densification [104].

In a more complete analysis of the densification/crystallization behavior, Keddie *et al.* [100] mapped out the film shrinkage as a function of temperature for varying heating rates. Their data is presented in Fig. 2-5. Three distinct regions were identified. At low temperatures (~100-250°C), densification is proposed to occur by spontaneous condensation reactions between hydroxyls. In this regime the rate of densification is independent of heating rate but the onset is slower for higher heating rates. In the second regime (~250-500°C), the gel reaches its glass transition temperature and densification occurs by structural relaxation and subsequent condensation. Thus, because the rapidly heated gels display a higher fictive temperature, they densify more rapidly and surpass the shrinkage of slower ramped films (27% shrinkage in 1°C/min films vs. 37% shrinkage in

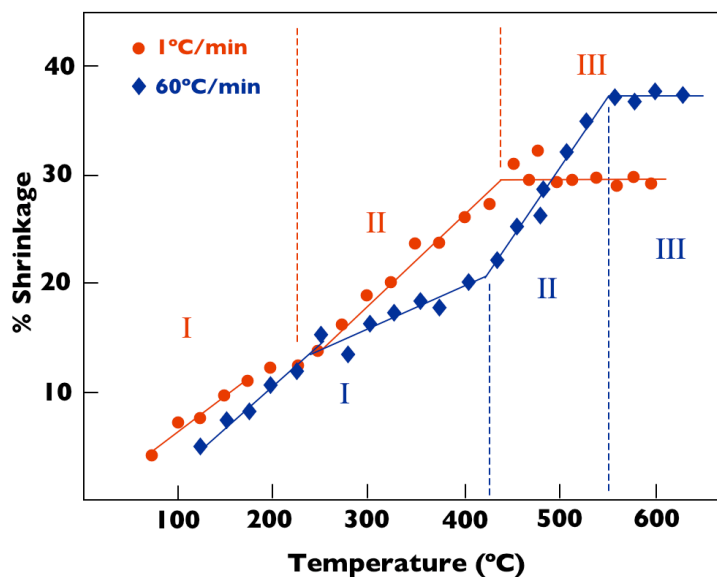


FIG 2-5 – Effect of Heating Rate on the Densification Behavior of Sol-Gel TiO₂ Films: Data from ref [100] showing the shrinkage in film thickness as a function of temperature for two different heating rates: 1°C/min and 60°C/min.

60°C/min films). The end of the second regime approximately corresponded with the onset of crystallization, and the amount of shrinkage plateaued. It was only in this final regime that significant carbon removal was observed. Thus, it was concluded, that hydroxyl condensation reactions dominated during densification and the residual carbon organics were not removed until crystallization—at which point they become insoluble in the material. Films heated in an RTA (8000°C/min) never arrived at the shrinkage plateau (up to 700°C) indicating that the percolation threshold for these films was not reached [100].

2.9 The Chemical Solution Deposition of PZT Thin Films:

The first report of a CSD prepared PZT thin film was that of Fukushima, Kodaira, and Matsushita in 1984 [105]. Their approach was akin to an MOD method with the use of lead 2-ethylhexanoate, zirconium acetylacetonate, and titanium tetrabutoxide as precursor sources and butanol as the solvent. The 2 μm thick 50/50 PZT thin films

prepared by this group on platinum substrates exhibited dielectric constants of 300 and reasonable polarization hysteresis with remanent polarizations of $30.5 \text{ } \mu\text{C}/\text{cm}^2$.

The first report of a true sol-gel CSD process similar to most modern chemistries was published by Budd, Dey, and Payne in 1986 [106]. Their solution contained lead acetate and Zr/Ti alkoxide precursors dissolved in methoxyethanol. The focus of this initial work was to investigate the effects of solution chemistry and heat treatment conditions on film microstructure and crystallinity.

In 1988 Yi, Wu, and Sayer [61] reported on the development of a PZT CSD solution chemistry that relied on precursor chelation. In their scheme, the Zr/Ti alkoxides were reacted with acetic acid to stabilize against hydrolysis; water or propanol were used as solvent media. Films were deposited by spin-coating on a variety of substrates including glass, silicon and mica. However measured values of dielectric constants (100-260) and remanent polarizations ($6.6 \text{ } \mu\text{C}/\text{cm}^2$) were low.

Throughout the 1990s, tremendous advancements were made in the understanding of processing CSD PZT thin films. The remaining portion of this section is devoted to a review of the accumulated understanding of PZT sol-gel chemistry and how it affects the final ceramic film's phase assemblage and microstructure.

2.9.1 Nucleation Behavior in CSD PZT Films:

Schwartz *et al.* [98] observed that modifying ligands can affect the temperature of organic extraction and consequently impact the crystallization behavior of PZT films. Solution precursors modified with HOAc were found to have less organic constituent (16% carbon) than those modified with acac (20% carbon). Furthermore, FTIR spectroscopy revealed that HOAc modified films were nearly devoid of C-O bonds after a 300°C , 5 min pyrolysis step while acac modified films retained most of their organic ligands. Because a gel cannot crystallize until it is fully pyrolyzed, acac-modified films exhibited higher crystallization temperatures, as verified by XRD data [98].

As already discussed, an increase in the crystallization temperature is also expected to favor heterogeneous nucleation events. Schwartz *et al.* [98] evaluated nucleation events

by the resulting microstructure. The lowest energy barrier events were assumed to be heterogeneous, epitaxial nucleations at the substrate, which resulted in columnar microstructures. Surface and bulk nucleation events require more energy and created randomly oriented grains. As expected, Schwartz *et al.* [98] observed that acac-modified films were more likely to nucleate at the substrate and grow columnar microstructures whereas HOAc-modified films displayed a higher tendency for surface and bulk nucleation.

Other kinetic factors also appear to affect nucleation events, in a manner consistent with the nucleation barrier model. For example, thinner films of HOAc-modified precursors exhibited columnar microstructures. Schwartz *et al.* hypothesize that the interface nucleated grains complete columnar growth prior to the onset of homogeneous nucleation in these thinner films. Slow heating rates also promote heterogeneous nucleation in this system. When heated slowly, the film remains within a regime that affords enough thermal energy to overcome the heterogeneous nucleation barrier but not the homogeneous nucleation barrier, making a columnar microstructure more favorable. In this instance, although the low temperature creates a sufficient driving force for homogeneous nucleation, the kinetic barrier cannot be overcome [98].

The addition of H₂O to the solution was observed to increase homogeneous nucleation events. Two reasons for this behavior were proposed. First, H₂O increases precursor hydrolysis, thereby reducing organic content and lowering the pyrolysis temperature. Second, well-hydrolyzed precursors create a more networked gel structure with increased free volume, surface area and hydroxyl content, which all increases the ΔG_v and favors homogeneous nucleation [98].

2.9.2 Evolution of the Perovskite Structure in CSD PZT Films:

It is generally accepted that PZT films prepared by sol-gel methods transform from the gel to ceramic state through an intermediate/transitory phase. Electron diffraction investigations by Reaney *et al.* [32] have demonstrated that the intermediate is stabilized because the interatomic distances within the gel state are comparable to the transitory

phase but substantially different from the perovskite. Wilkinson *et al.* [107] tracked the phase development of 2-MOE derived CSD 45/55 PZT films using *in situ* x-ray diffraction (XRD). This investigation revealed that perovskite PZT crystallizes at $\sim 500^\circ\text{C}$ through a transitory phase. These investigators loosely identify this intermediate phase as a fluorite structure. A pyrochlore phase has also been suggested. However, pyrochlore is simply a $2 \times 2 \times 2$ supercell of fluorite with ordered vacancies and cations, and since few researchers have shown diffraction data with superlattice peaks to indicate this ordering, fluorite is probably the more accurate descriptor [107]. Because the distinction is marginal, though, fluorite and pyrochlore will be used interchangeably when discussing the intermediate phase.

The ability for fluorite to accommodate a higher concentration of vacancies with less ordering than perovskite favors its initial formation from the gel state. The >6 coordination of Zr in the gel has also been suggested to stabilize fluorite formation. This hypothesis is supported by XRD results that indicate PT forms homogeneously from the gel while PZT and PZ require intermediates [107]. Additionally, Lefevre *et al.* have determined that the fluorite phase has higher PbO volatility than the perovskite. Thus, the intermediate may self-stabilize if held at temperatures below perovskite crystallization [108]. To counteract Pb loss, 5-15% excess Pb is typically added to sol-gel solutions. PbO overlayers and PbO overpressures have also been demonstrated to neutralize PbO volatility [108].

Organic pyrolysis conditions also appear to influence the behavior of the intermediate phase. Reaney *et al.* [32] showed that *111* oriented perovskite PZT films develop when pyrolyzed at 350°C in air. If the pyrolysis temperature is increased to 420°C , a *100* orientation forms and pyrochlore becomes difficult to remove. These authors suggest that initially an unstable $\text{Pb}_2(\text{Zr,Ti})_2\text{O}_6$ phase forms that can rapidly transform to the perovskite structure. This condition is proposed to dominate at low pyrolysis temperatures. At higher pyrolysis temperatures, the more oxidized $\text{Pb}_2(\text{Zr,Ti})_2\text{O}_7$ pyrochlore phase may form. This phase places Pb into a 4+ oxidation state, which may stabilize it against perovskite transformation. Reaney *et al.* propose that only the more

stable 100 oriented crystallites exhibit sufficient driving force to compel the pyrochlore-to-perovskite conversion. To support this hypothesis, films pyrolyzed at 420°C in reducing atmospheres have been shown to exhibit 111 orientations, implying that the reducing atmosphere stabilizes the easily convertible $\text{Pb}_2(\text{Zr,Ti})_2\text{O}_6$ phase [32].

This formation of an intermediate may be extremely beneficial in eliminating porosity in PZT thin films. Because the intermediate is expected to lower the driving force to perovskite transformation, it should also promote heterogeneous nucleation at the substrate. The resulting growth front of columnar grains may then act to push porosity out of the film [108, 109].

3. Investigation of Organic Extraction in CSD PZT Films on Copper Substrates

In this chapter, exploratory experiments are discussed involving PZT films derived from alkanolamine and acetylacetonone (acac) chelated solution chemistries deposited directly on copper foils. This work primarily focuses on extracting organics—specifically with regards to various atmospheric conditions and solution chemistries. Although these experiments demonstrate only moderate success, they do give crucial insight into the appropriate parameters / metrics that must be considered in designing a process to achieve PZT/Cu compatibility. In particular, this chapter emphasizes the necessity to develop a process that carefully balances the need to eliminate copper oxidation while maintaining uncracked films with the proper perovskite phase assemblage.

3.1 Solution Preparation:

Various solutions have been prepared for this work, but all have been designed to give the same final film composition. The Zr/Ti ratio has been kept near 52/48, which is approximately the location of the morphotropic phase boundary at room temperature. Solutions also contain 15 mol% excess Pb to compensate for PbO volatility and maintain stoichiometry. The precursor source chemicals also remained constant. The titanium source was titanium (IV) isopropoxide (Sigma-Aldrich, 99.999% purity) and the zirconium source was zirconium (IV) propoxide (70 wt% in 1-propanol, Sigma-Aldrich). The lead precursor was lead acetate trihydrate powder (Sigma Aldrich, 99+% purity).

3.1.1 Alkanolamine Chelated PZT Solution:

Initial experiments utilized a solution chemistry that chelated the metalorganic precursors with alkanolamine moieties such as diethanolamine (DEA) and triethanolamine (TEA); thus, this solution will simply be referred to as the ethanolamine chelated (EC) solution. This chemistry is based upon work initially completed by Kim *et al.* [110] and has been used in previous studies of PZT thin films deposited directly on nickel surfaces [72, 73].

Solution preparation began with 40 mL of MeOH in an open flask. The chelating agents (1 mL of DEA and 2 mL of TEA) were added and the solution was continually stirred at 300 rpm and maintained at a temperature of 80°C during precursor addition. Next 2.834 mL (0.0096 mol Ti) of titanium isopropoxide was added and the flask was lightly capped. The precursor was given ~45-60 min to react. Then, 4.662 mL (0.0104 mol Zr) of zirconium propoxide was added. Again, the solution was given 45-60 min to react. Next, 8.724 g (0.023 mol Pb) of lead acetate trihydrate was added. The solution was then allowed to homogenize for ~90-120 min, at which point the heat source was turned off but stirring continued. Next, 3 to 6 drops of nitric acid (70 wt% in H₂O, 99.999% purity, Sigma-Aldrich) was added to modify the solution's pH and possibly act as a catalyst for hydrolysis / polycondensation. The solution was then diluted 1:1 with MeOH, filtered, and allowed to stir at 300 rpm overnight to complete homogenization. The final solution is designed to have a concentration of about 0.2 M. For some experiments, the solution was further diluted with MeOH to give a 0.1 M concentration.

Note that currently no study has been published on the stability and aging effects of this solution's chemistry. However, previous experience with this solution at North Carolina State University has indicated that it retains stability for a few months with minimal change in film properties [111].

3.1.2 Acetylacetonone (Acac) Chelated PZT Solution:

Due primarily to cracking issues, which will be discussed later in this chapter, a solution with a lower boiling point chelating agent was also prepared. This solution was synthesized using 35 mL of MeOH as the starting solvent. The solution was continually stirred at 500 rpm and 90°C throughout the preparation. Acac was added (4.107 mL) in sufficient quantity to give a 4:1 molar ratio with the B-site metalorganics. Next, the B-site precursors were added: 2.331 mL (0.0052 mol Zr) zirconium propoxide and 1.417 mL (0.0048 mol Ti) titanium isopropoxide. Some precipitation initially occurred, but particles redissolved after 15-20 min of mixing. Next the lead acetate (4.362 g, 0.0115 mol Pb) was

added and given about 90 min to dissolve and homogenize. The final solution was filtered and had a concentration of about 2.3 M.

3.2 Procedures for PZT Thin Film Preparation:

Various permutations of processing steps and ranges of processing variables have been examined in preparing PZT thin film samples for this thesis. These conditions are summarized in Fig. 3-1 and specific parameters will be clarified when appropriate. This section describes the basic steps that were utilized in thin film preparation and the ranges of process variables that were explored.

All solutions were deposited through 0.2 μm filters and spin-coated on 18 μm thick copper foils (Oak-Mitsui, PLSP 0.5 oz foil) at 3000 rpm for 30 s. Drying was then performed on a hotplate between 200°C and 300°C for 5 min. The standard condition was 250°C; variations from this temperature will be noted in the text. In many cases, samples were then thermolyzed at a higher temperature (350°C - 450°C) in a controlled atmosphere 2-inch diameter tube furnace. The controlled atmosphere furnace was utilized to create ambient air, nitrogen, and wet nitrogen atmospheres. All incoming gases were bubbled through water at ~ 1 slm. The nitrogen source was a reagent grade dewar (99.999% purity). Wet nitrogen conditions were created by heating the bubbler to $\sim 75^\circ\text{C}$ to increase the vapor pressure of water; this provided the conditions referred to as “water vapor thermolysis” or WVT. Samples were held in the desired atmosphere for 5 min prior to being transferred into the hot-zone to allow a steady-state condition to be reached; samples were also cooled in their given atmosphere (5 to 10 min) to prevent high temperature exposure to ambient conditions. This latter condition was especially important during crystallization anneals. However this precautionary measure was relaxed during water vapor thermolysis because of problems from condensation at the cooler tube ends.

The spinning/drying/thermolysis procedures were repeated until typically 4 layers were deposited. The samples then underwent a crystallization anneal at temperatures between 600°C and 700°C in either the controlled atmosphere furnace or a 3-inch diameter

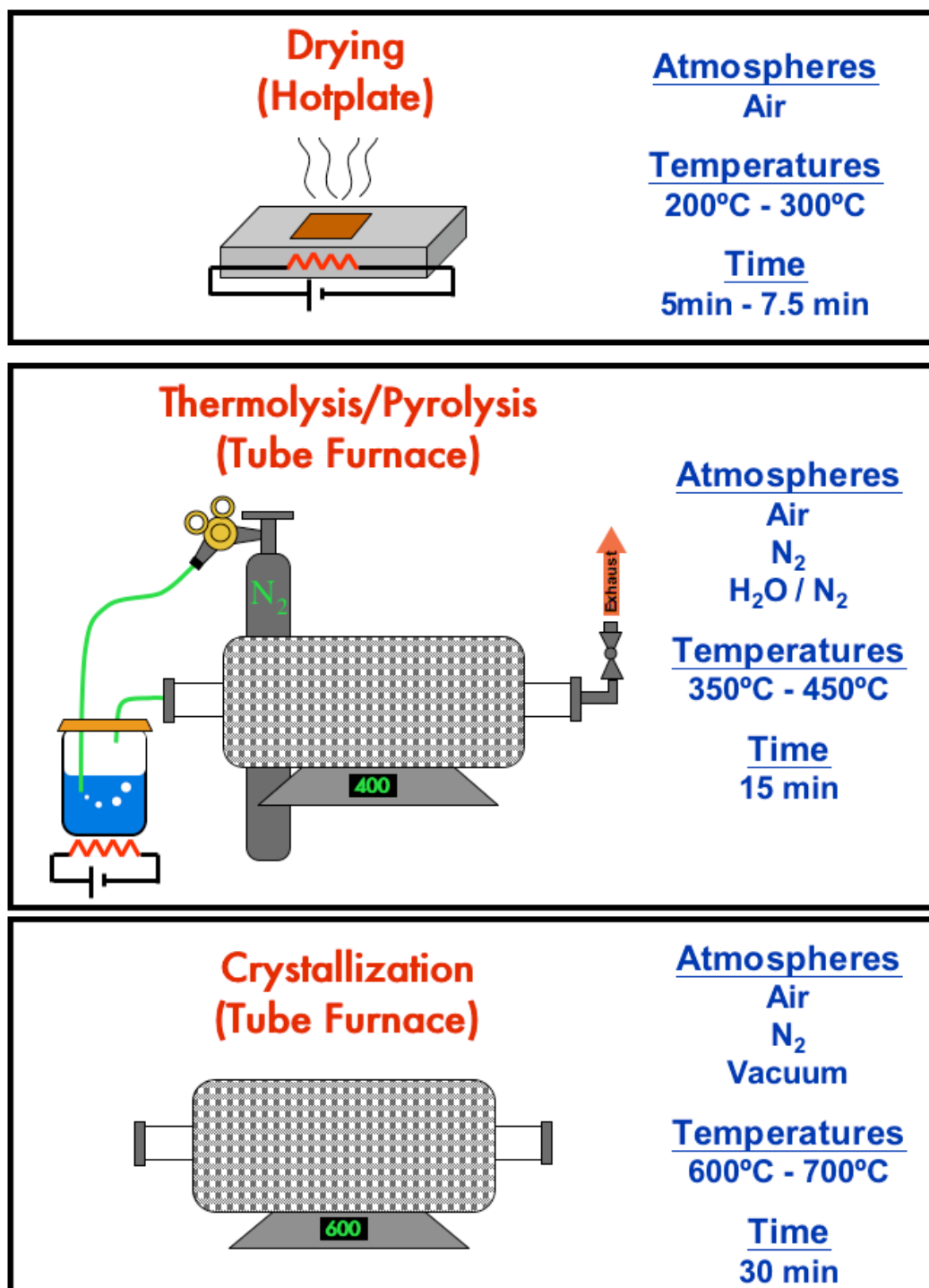


FIG 3-1: Summary of Process Parameters Explored in Chapter 3: *A description of the different atmospheres, temperatures, and times explored for each processing step in this chapter.*

vacuum tube furnace. Conditions in the controlled atmosphere furnace were similar to those used for thermolysis. The vacuum furnace had a base pressure of $\sim 10^{-6}$ Torr and the pO_2 could be increased to 10^{-3} Torr by bleeding in O_2 through a leak valve. The samples were typically inserted directly into the heated furnace at the annealing temperature without ramping unless otherwise noted. The annealing time was always 30 min.

3.3 Organic Removal in Dry Atmospheres:

As a starting point, conventional organic removal conditions were investigated; these include pyrolyzing in air and nitrogen. This section discusses these initial results.

3.3.1 Organic Removal in Air:

In previous work where PZT was deposited on Ni surfaces [72, 73], samples were prepared using an ambient air pyrolysis step. Although interfacial reaction layers are expected to occur, these experiments were completed to provide a baseline for the current investigation.

Fig. 3-2 shows the XRD results for samples prepared from the EC solution using a 250°C dry step followed by a 400°C pyrolysis condition in either static or flowing air. Following pyrolysis, both samples were crystallized at 650°C in flowing nitrogen. Fig. 3-2 indicates no detectable substrate oxidation after drying, but significant oxidation occurs during pyrolysis.

This data has two implications. First, these copper surfaces are more susceptible to oxidation than the electroless nickel surfaces investigated previously [72, 73]. Second, the oxidation does not appear to occur until the 400°C pyrolysis step. Consequently, we conclude that an inert-gas containing atmosphere is needed to preserve the foil surface. This possibility is discussed in the next section.

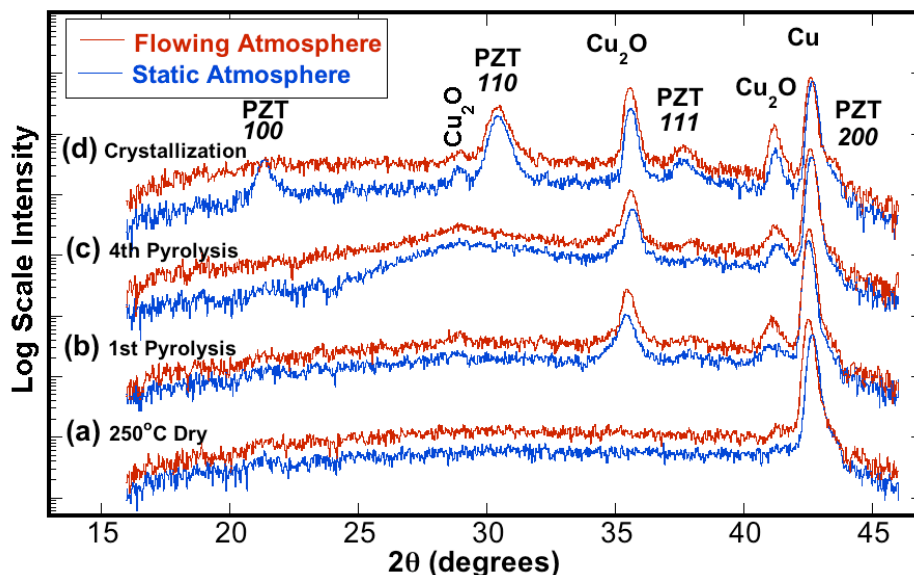


FIG 3-2 – Phase Evolution for EC Air Pyrolyzed PZT Films on Copper: XRD data showing the phase evolution in the PZT/Cu system using an ambient air pyrolysis; (a) 1st 250°C dry, (b) 1st 400°C pyrolysis in air, (c) 4th pyrolysis, (d) 650°C crystallization in N₂.

3.3.2 Organic Removal in Nitrogen:

Unpublished work completed by Jimison *et al.* [112] in 2003 indicated that EC derived films deposited on copper become extremely dark in color (almost black) upon heat treatment (drying/thermolyzing) in dry N₂ atmospheres. However, this color change only appeared in regions containing the film; the foil's underside and regions of foil covered by tape during spin-coating retained a “copper” color. XRD results suggested the presence of Cu₂O. Thus, these investigators concluded that the darkened color indicated the presence of copper oxide and that oxygen contained within the organics had been the primary source of this oxidation.

This experiment was repeated in the current study and the XRD results are shown in Fig. 3-3. Two reflections emerge during pyrolysis and appear to fit with the d-spacings for 110 PZT and 111 Cu₂O. However, note that the peak intensities (see appendix) are inconsistent with the polycrystalline microstructure that is present. Consequently, we

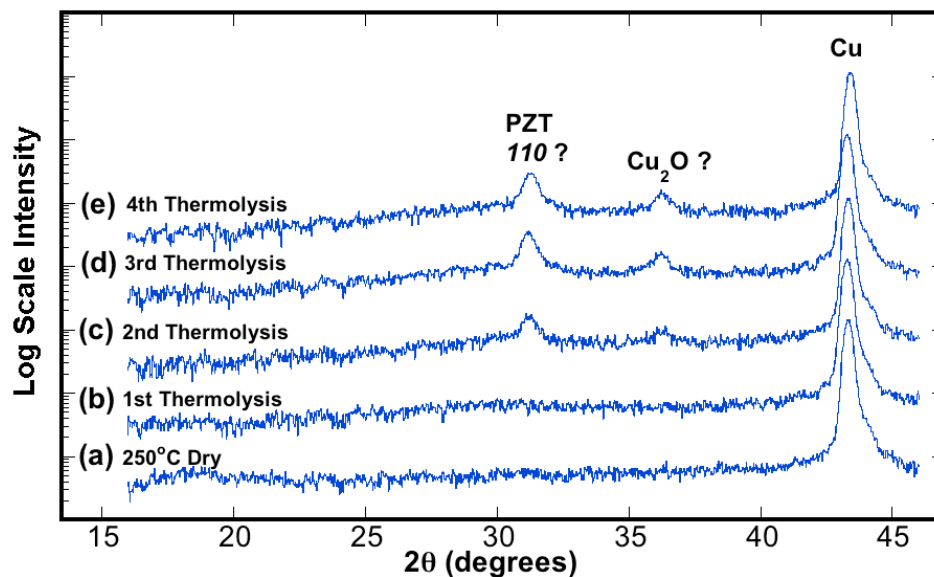


FIG 3-3 – Phase Evolution in EC Derived Film During N_2 Thermolysis: XRD data showing the phase evolution in the PZT/Cu system using a 400°C flowing N_2 thermolysis condition; (a) 1st 250°C dry, (b) 1st 400°C thermolysis in N_2 , (c) 2nd thermolysis, (d) 3rd thermolysis, (e) 4th thermolysis.

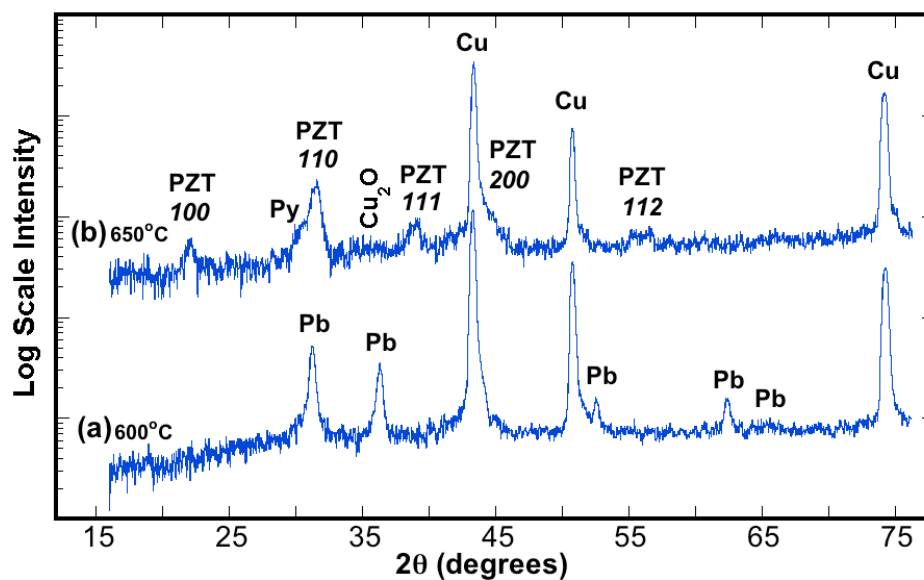


FIG 3-4 – XRD of Crystallized EC Derived, N_2 Thermolyzed PZT Films: XRD data of N_2 thermolyzed EC-derived PZT films crystallized at (a) 600°C and (b) 650°C.

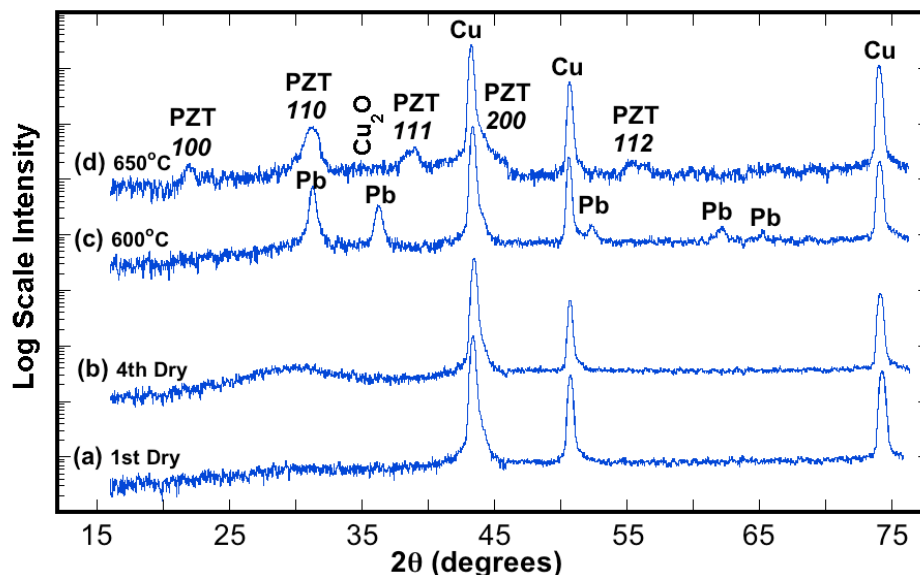


FIG 3-5 – Phase Evolution in EC Derived 300°C Dried PZT Films: XRD data showing the phase evolution in the PZT/Cu system using a 300°C drying step; (a) 1st dry, (b) 4th dry, (c) 600°C anneal in N₂, (d) 650°C anneal in N₂.

question the initial interpretation. In Fig. 3-4, XRD for these same films are shown after crystallization in N₂. The higher angular range and sharper peaks allow for a more clear interpretation—the presence of metallic lead. Thus, it is concluded that when the EC solution chemistry is thermolyzed in a low-pO₂ environment such as flowing nitrogen, the lead precursors decompose and the remaining Pb species are reduced. This emergence of metallic Pb is also consistent with the dark color that appears in these films. A set of XRD scans tracking the phase evolution in a 300°C dried sample and subsequent annealing in N₂ is presented Fig. 3-5. Again, Pb precipitates during the 600°C anneal, despite not being detected by XRD after thermolysis.

These films also exhibit severe cracking. The N₂ thermolyzed samples cracked during the 4th thermolysis step (Fig. 3-6) while the 300°C air pyrolyzed samples cracked during the crystallization anneal (see Fig. 3-7). Two explanations are proposed: (1) disruption / dissolution of the gel network as a result of the liquid Pb precipitation

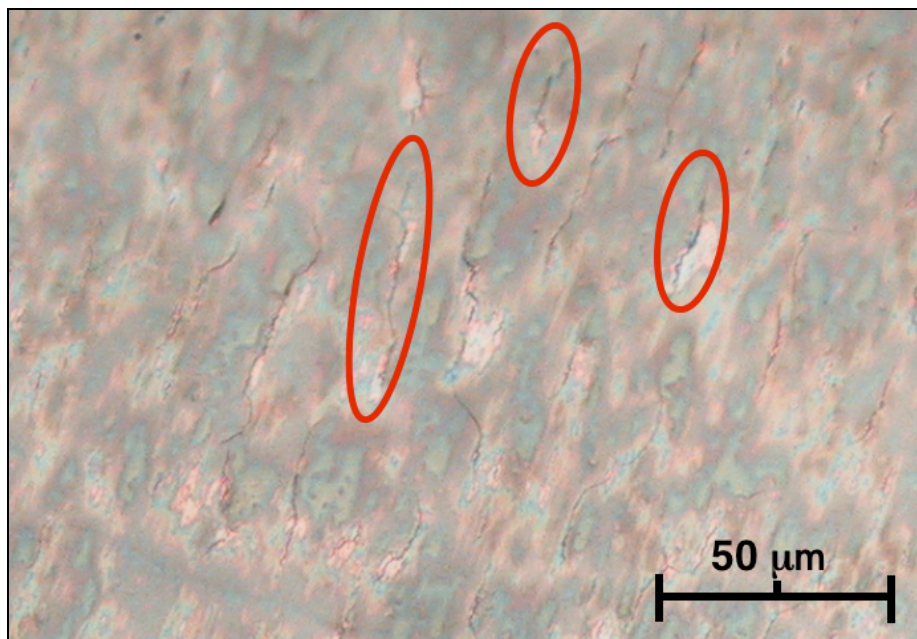


FIG 3-6 – Micrograph of 4-Layer EC N₂ Thermolyzed Sample: *Optical microscopy image showing cracks in a 4 layer EC solution derived, N₂ thermolyzed sample. Some cracks are indicated with circles. (Sample matches XRD pattern in Fig. 3-3e.)*

($T_{m,Pb} = 327^{\circ}\text{C}$) and (2) insufficient gel network formation due to unhydrolyzed alkanolamine modifying ligands. Both mechanisms suggest that the skeletal M-O-M network is inadequate—due to either Pb precipitation or the low reactivity (transparency) of the alkanolamine ligands. Although mechanism (1) may at first appear to dominate, Figs. 3-5 and 3-7 show that ligand transparency is also important. In this system, Pb did not precipitate prior to crystallization. Therefore, if a suitable M-O-M network had been formed during the 300°C drying step, Pb precipitation would have been frustrated during the crystallization anneal. However, this was not the case for the 600°C crystallization condition; instead the precursors remained transparent and the network's compliance allowed for Pb precipitation leading to similar cracking as the N₂ thermolyzed sample. This is consistent with previous research [111] showing that a $400\text{-}450^{\circ}\text{C}$ air pyrolysis step is needed to fully remove the alkanolamine ligands.

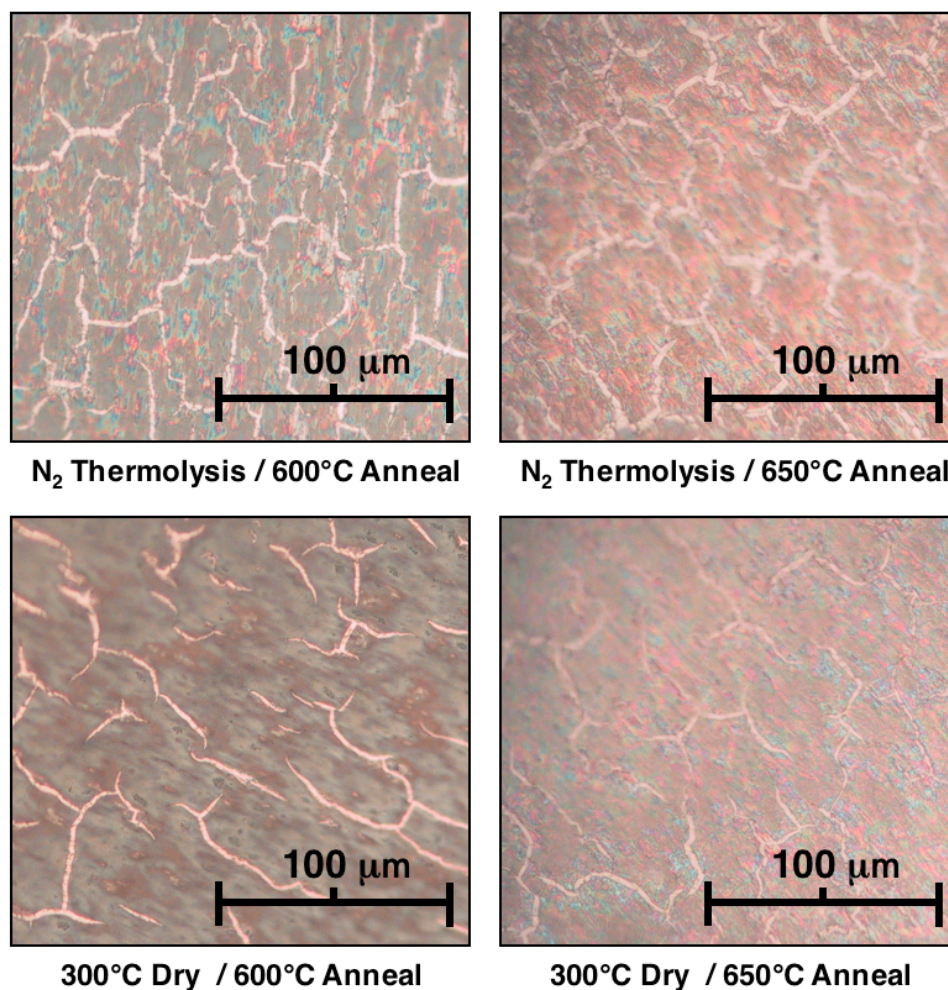


FIG 3-7 – Micrographs of Crystallized EC Samples Processed in Dry Conditions: *Optical microscopy images showing cracking upon crystallization in EC solution derived films processed under both a N₂ thermolysis and 300°C drying condition. (Samples match with XRD patterns presented in Figs. 3-4 and 3-5.)*

In summary, thermolysis treatments in dry atmospheres create two significant problems: (1) Crystallized samples become severely cracked and (2) large quantities of Pb may precipitate out of the gel. Work completed by Jimison *et al.* [112] and this author has shown that incorporating water vapor into the thermolysis atmosphere can alleviate these problems; this approach is discussed in the next section.

3.4 Water Vapor Thermolysis of EC Derived PZT Films:

In an attempt to more effectively remove the alkanolamine ligands from the gel without implementing severe oxidizing conditions, water vapor was introduced to the atmosphere during the thermolysis step. This section reviews previous research in water vapor thermolysis (WVT) and describes the results of applying WVT to EC PZT films.

3.4.1 Previous Research on Water Vapor Thermolysis:

Water is necessary for the hydrolysis of organic ligands within the gel. Thus, the addition of water vapor to the atmosphere is expected to make hydrolysis more favorable via Le Chatelier's Principle. Although some work has been published to support this premise, the amount of literature is sparse. The work of Kitaoka *et al.* [113] examined the processing of sol-gel PLZT fibers in an autoclave with H₂O vapor. The inclusion of water vapor appears to have enhanced hydrolysis rates and alleviated cracking issues in the PLZT fibers. However, in their data it is difficult to differentiate between the effects of water vapor and process temperature. Other work by Kato [114] on SrBi₂Ta₂O₉ films clearly shows FTIR spectra where absorption from the ligand groups is reduced in water vapor atmospheres relative to ambient conditions. This improved organic extraction also provided a lower crystallization temperature and better film crystallinity with larger grain growth. Similar results have also been seen for sol-gel PZT films where crystallization temperature was reduced by 50°C when processed in a water vapor atmosphere [115].

3.4.2 Effects of WVT Temperature and Crystallization Atmosphere:

A set of films was prepared as discussed previously (250°C dry, 400°C thermolysis). However, water vapor was introduced to the N₂ thermolysis atmosphere. XRD data is shown for this film set in Fig. 3-8. This figure indicates that Cu₂O formation is reduced with respect to air pyrolysis and, in contrast to dry N₂, Pb does not precipitate.

These 400°C WVT samples were annealed at 600°C for 30 min in three conditions: a water vapor atmosphere, vacuum (10⁻⁶ Torr), and in flowing reagent grade nitrogen. XRD results from this experiment are shown in Fig. 3-9. A striking result is the enhanced

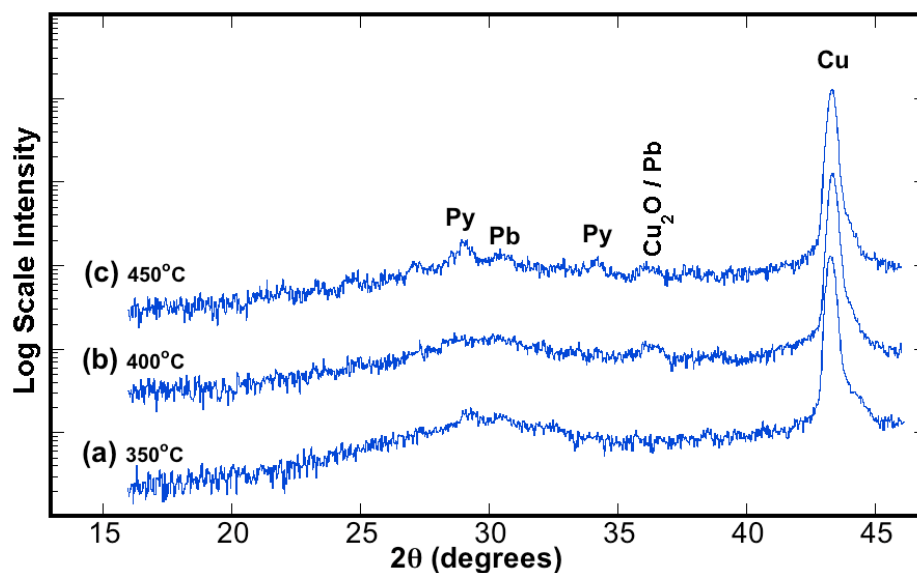


FIG 3-8 – XRD Analysis of Varying WVT Temperatures: XRD data collected from 4-layer EC solution deposited samples using WVT at (a) 350°C, (b) 400°C, (c) 450°C.

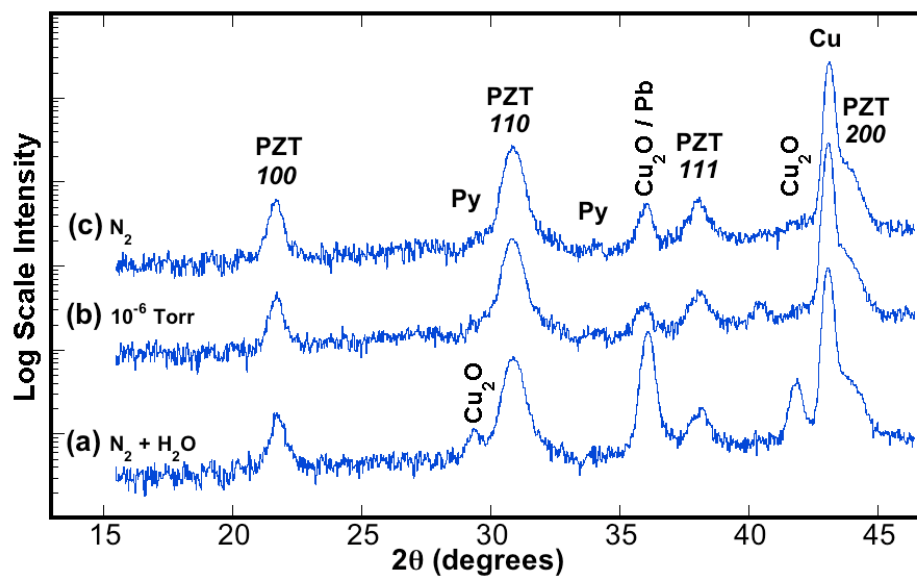


FIG 3-9 – Effect of Crystallization Atmosphere on WVT PZT: XRD data collected from a 4-layer EC solution deposited WVT 400°C sample crystallized at 600°C in (a) water vapor atmosphere, (b) vacuum of 10^{-6} Torr, and (c) flowing nitrogen.

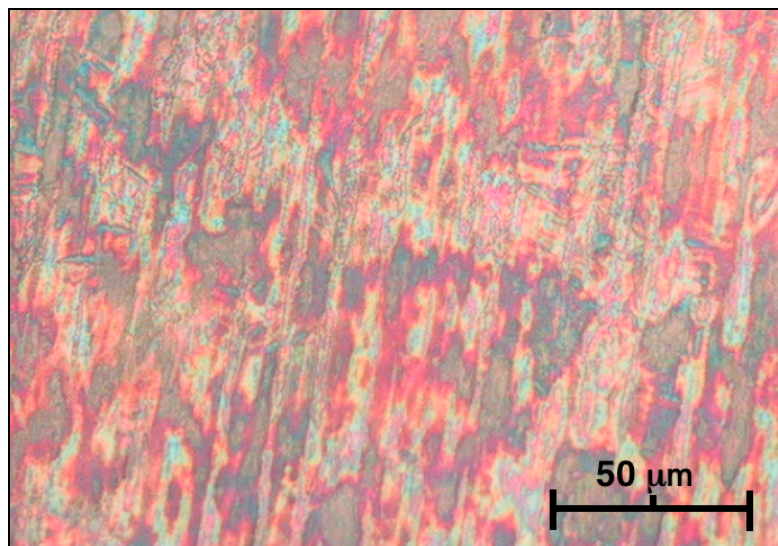


FIG 3-10 – Micrograph of EC WVT Sample: *Optical microscopy image of a 4-layer EC solution derived film that has undergone 400°C WVT but is uncrystallized. (Sample corresponds to XRD pattern in Fig. 3-8b).*

rate of copper oxidation when crystallization is performed in a water vapor rich atmosphere—sufficient enough to clearly observe the 200 and 110 reflections of Cu_2O . Because the sample prepared in a dry nitrogen atmosphere displays less oxidation, the water vapor can be identified as the source for substrate oxidation. It is suggested that once hydrolysis of organic ligands is complete, the presence of water vapor becomes deleterious and leads to copper oxidation. Another explanation may be that the oxidation of copper via interaction with H_2O is contingent on higher reaction temperatures.

This data also indicates that WVT significantly reduces the amount of Pb precipitation. When crystallization was performed at 600°C in dry thermolysis conditions, films contained Pb with minimal perovskite (Fig. 3-4a). In contrast, the WVT samples are primarily perovskite with minimal Pb.

Finally, it should be noted that despite severe oxidation, the water vapor process did avoid crack formation during both thermolysis (see Fig. 3-10) and crystallization (Fig. 3-11). However, WVT films that were annealed in both nitrogen and vacuum cracked upon crystallization (see Fig. 3-12). Although this issue of cracking may seem mundane, it is a critical problem that is further addressed in Chapter 4.

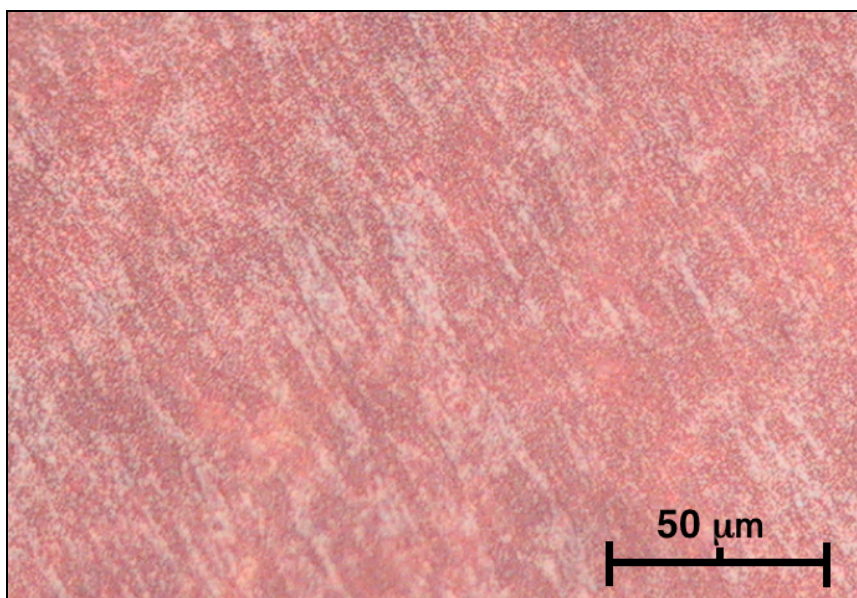


FIG 3-11 – Micrograph of WVT PZT Film Crystallized in Water Vapor: *Optical microscopy image of a 4-layer EC solution derived film that has undergone 400°C WVT and crystallization in a water vapor atmosphere. (Sample corresponds to XRD pattern in Fig. 3-9a).*

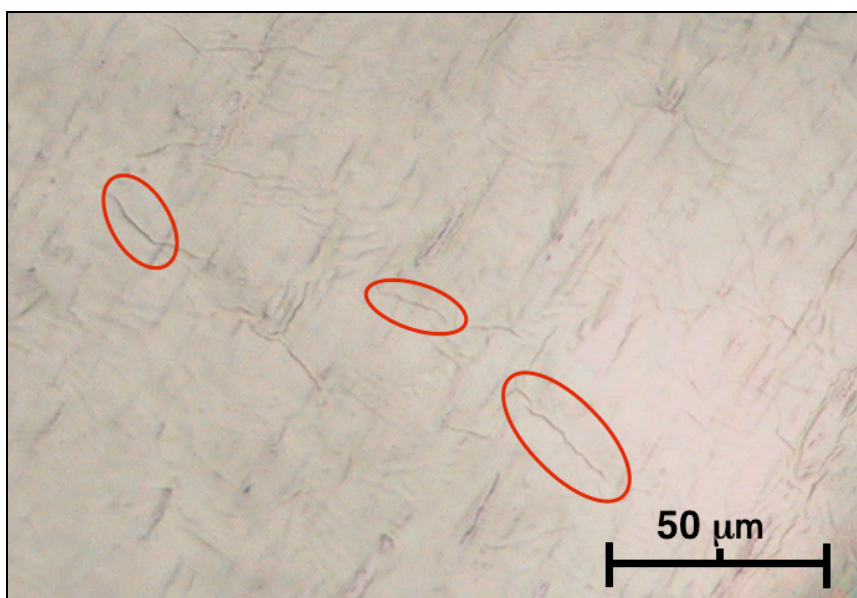


FIG 3-12 – Micrograph of WVT PZT Film Crystallized in N₂: *Optical microscopy image of EC solution derived film that has undergone 400°C WVT and crystallization in N₂. Image was taken on Pt coated region to improve crack visibility (Sample corresponds to XRD data in Fig. 3-9c).*

3.4.3 Effects of Oxygen Partial Pressure on Crystallization Behavior:

Because the vacuum anneal shown in Fig. 3-9 appeared to be the most promising atmosphere with respect to minimizing substrate oxidation, these conditions were extended to films prepared under a more complete set of thermolysis conditions. The XRD results are shown in Fig. 3-13. In all cases crystallization of the perovskite phase is minimal or incomplete, even when the annealing temperature is raised to 700°C.

Crystallization of the perovskite phase in the sample thermolyzed at 450°C appears to be prevented by the competing crystallization of a pyrochlore phase. This observation is consistent with the XRD data collected for the gel state (Fig. 3-8c) that indicated pyrochlore formation at this thermolysis temperature. In contrast, the lack of crystallization in the samples that were thermolyzed at 350°C and 400°C (2 layers at once) is hypothesized to originate from inadequate organic removal during thermolysis. The subsequent low-pressure annealing atmosphere may be insufficient to hydrolyze/pyrolyze the remaining organics, and thus, crystallization is frustrated.

To further investigate this condition of insufficient organic removal, the 350°C thermolysis sample underwent crystallization anneals at higher oxygen partial pressures (10^{-4} and 10^{-3} Torr). The XRD data collected for these conditions is shown in Fig. 3-14 along with a similarly annealed 400°C thermolysis sample for reference. Despite incomplete perovskite formation, this data does reveal that higher pressures promote more crystallization in the 350°C thermolyzed sample. These results support the possibility that the 350°C sample contains a significant organic fraction that requires a sufficient amount of oxygen in the annealing atmosphere to drive pyrolysis. However, as a consequence, the substrate is more oxidized.

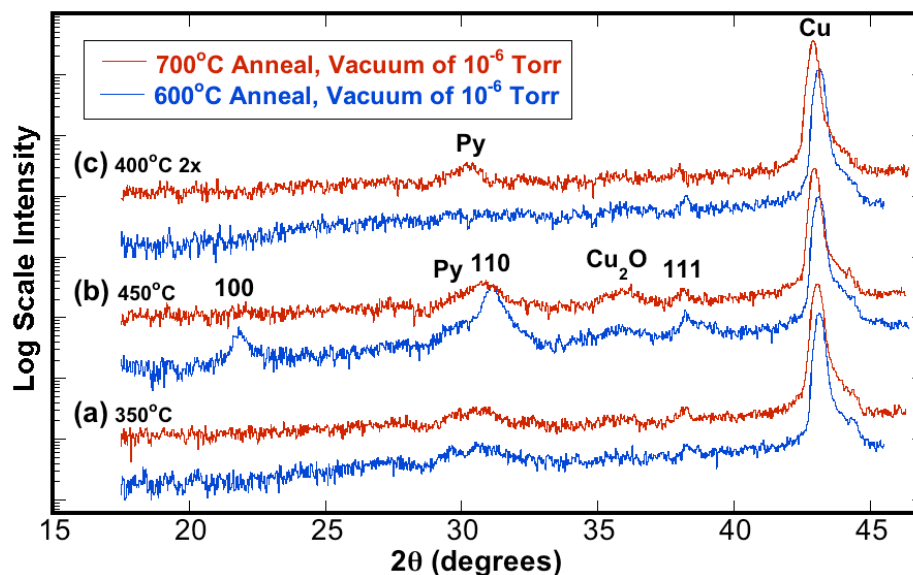


FIG 3-13 – Effect of WVT Condition on PZT Crystallization in Vacuum: XRD data showing crystallized 4-layer PZT films using different WVT conditions; (a) 350°C, (b) 450°C, (c) 400°C on two 250°C dried layers at once (only two thermolysis runs total).

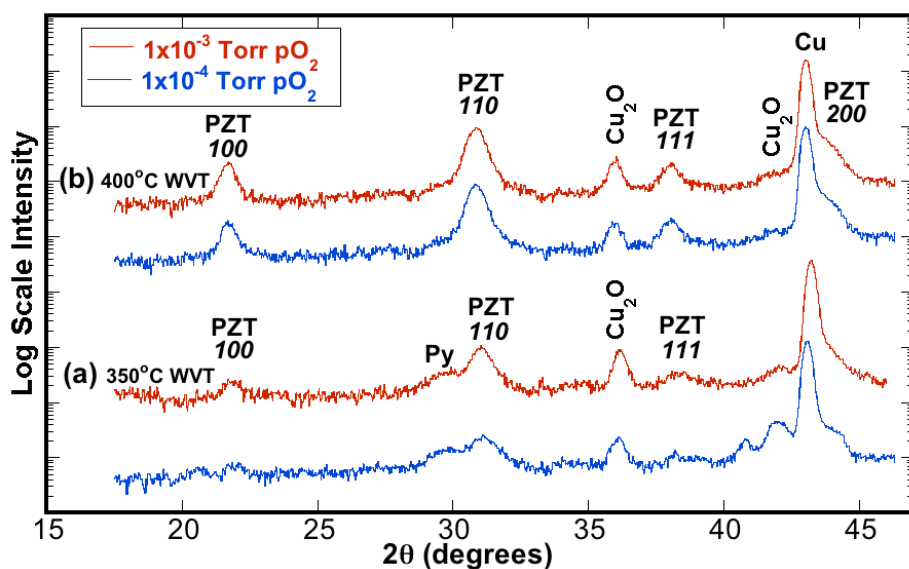


FIG 3-14 – Impact of Crystallization pO_2 on WVT PZT Films: XRD data showing EC solution derived PZT films crystallized at 600°C under higher pO_2 conditions as obtained in a vacuum furnace; (a) 350°C thermolyzed sample, (b) 400°C thermolyzed sample.

3.4.4 Dependence of Solution Molarity:

A set of experiments was also conducted to examine the effect of solution concentration on substrate oxidation. A 6-layer film was processed from a 0.1 M EC solution with a 400°C WVT step performed on each layer. Two samples were created using different thermolysis times (15 min and 7.5 min). The results of crystallizing these samples at 600°C under different vacuum pressures are shown in Figs. 3-15 and 3-16.

The sample thermolyzed for 15 min (Fig. 3-15) indicates a clear trend of increasing copper oxidation with increasing atmospheric pressure. The film crystallized at 10^{-6} Torr is predominantly perovskite and the substrate oxidation is comparatively low for this phase assemblage. Unfortunately, electrical response could still not be acquired because this entire set of films had cracking problems.

The set of samples thermolyzed for only 7.5 min (Fig. 3-16) appear to have had insufficient organic removal. As previously observed, higher oxygen pressures appear to alleviate this problem. The sample crystallized in flowing N_2 exhibits the most perovskite formation, which is consistent with the oxygen partial pressure of $\sim 10^{-3}$ Torr measured for our nitrogen source. Thus, this result is consistent with increasing oxidation. Also, consistent with previous results, these samples showed increased substrate oxidation and film cracking with increased perovskite formation.

3.4.5 Improved Phase Assemblage with Sample Containment During Crystallization:

During crystallization small Cu pieces are used to pin the foil edges and keep the sample flat. These covered regions were often observed to be of a different color than those regions exposed directly to the annealing atmosphere. When examined by XRD, these covered regions often exhibited superior phase assemblages with well-crystallized perovskite structures and virtually undetectable levels of substrate oxidation. An example of this situation is shown in Fig. 3-17 where two portions of a 350°C thermolyzed sample are investigated. As shown previously, this sample is poorly crystallized in a vacuum of 10^{-6} Torr. However, the region of the film covered by a copper block (used to hold the

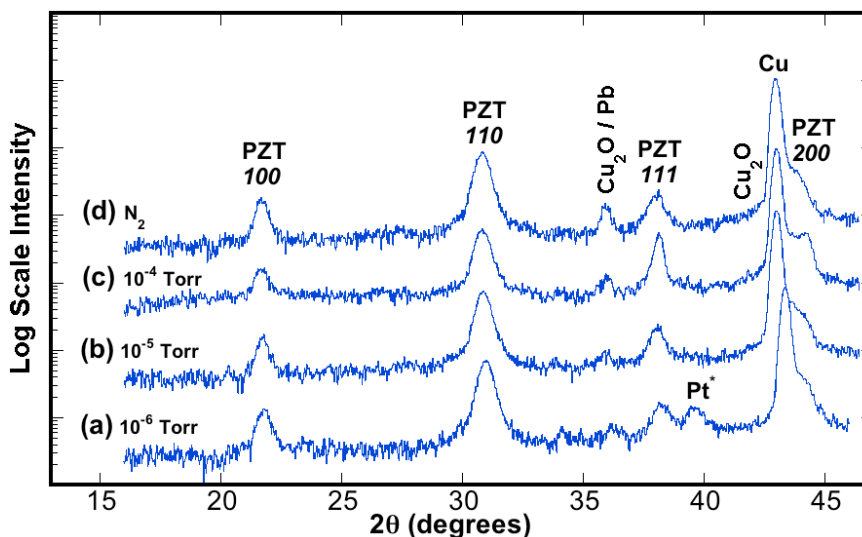


FIG 3-15 – Crystallization Behavior of 0.1 M EC Solution with 15 min WVT: XRD patterns showing a 6-layer 0.1 M EC solution derived PZT film thermolyzed at 400°C for 15 min and then crystallized at 600°C in different atmospheres; (a) vacuum of 10^{-6} Torr*, (b) vacuum with $pO_2 = 10^{-5}$ Torr, (c) vacuum with $pO_2 = 10^{-4}$ Torr, (d) flowing N_2 .

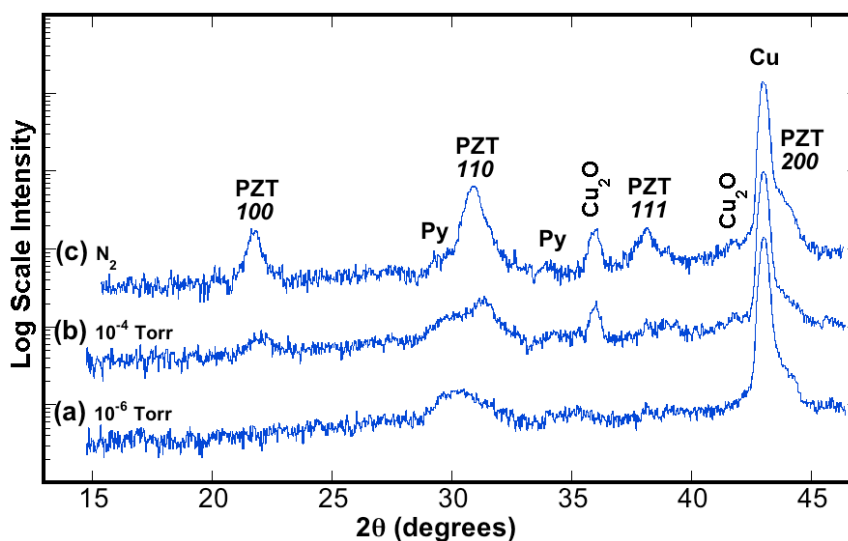


FIG 3-16 – Crystallization Behavior of 0.1 M EC Solution with 7.5 min WVT: XRD patterns showing a 6-layer 0.1 M EC solution derived PZT film thermolyzed at 400°C for 7.5 min and then crystallized at 600°C in different atmospheres; (a) vacuum of 10^{-6} Torr, (b) vacuum with $pO_2 = 10^{-4}$ Torr, (c) flowing N_2 .

* Pt peak is from Pt top electrodes that had been sputtered on the sample.

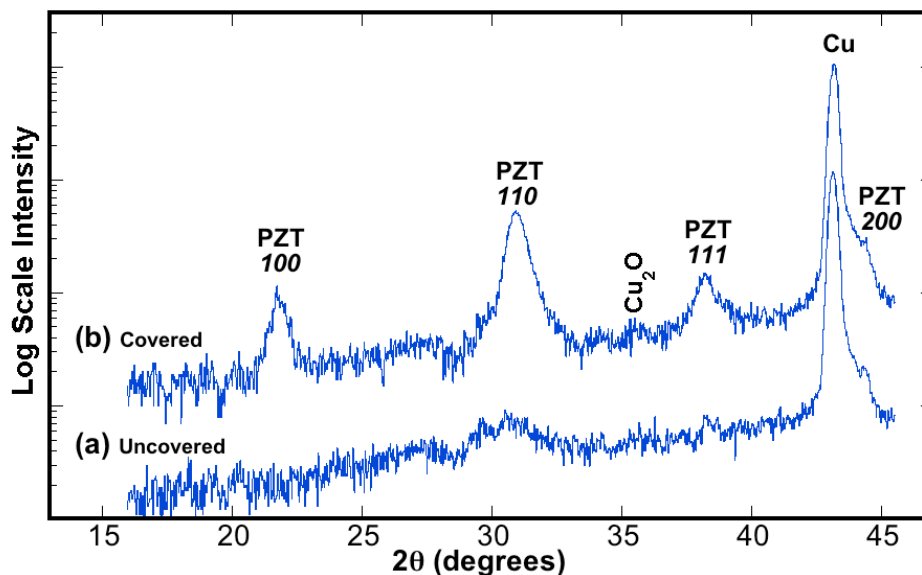


FIG 3-17 – Effect of Sample Containment on Perovskite Crystallization: XRD data for a single EC solution derived film that was WVT at 350°C and then annealed at 10^{-6} Torr—portion (a) was uncovered while portion (b) was covered with a copper block.

sample in place upon annealing) exhibits a well-formed perovskite phase when annealed under the same conditions. Although this result is not well understood, it may indicate that the covered region has trapped oxygen to drive pyrolysis of residual organics. This cover may also act as a mechanism to reduce PbO volatility, thereby stabilizing the perovskite phase preferentially to the pyrochlore structure. This latter supposition is consistent with reports of similar improvements in perovskite stabilization for PbO overcoat layers and high-temperature processes performed in PbO-rich atmospheres [108]. Unfortunately, such enclosures did not eliminate cracking.

3.4.6 Implications of WVT Investigation:

The implementation of WVT has to some degree alleviated the problems identified with dry atmospheric conditions. Lead precipitation has been obstructed. Thus, samples that underwent WVT at 400°C did not crack upon 4 layers of deposition (Fig. 3-10). Additionally, film cracking during crystallization has been reduced. Comparing the micrographs of WVT samples to those thermolyzed in dry conditions, reveal that the

cracking mechanism has changed. Under dry conditions, the film appears to have severely shrunk leaving gaping crack lines open to the substrate—indicating unmanaged film densification. Cracks appearing in the WVT sample are often much finer, possibly indicating the extraction of entrapped organics. Thus, it is hypothesized that the water vapor atmosphere improves hydrolysis and polymerization of the M-O-M network but fails to completely volatilize / remove the alkanolamine-related byproducts. These organic species become trapped in the gel's network. Depending on the crystallization annealing conditions, these trapped species can either frustrate perovskite crystallization without cracking the film (Fig. 3-13, no perovskites/no cracking) or escape and allow for crystallization but cause film cracking (Figs. 3-9 & 3-12, perovskites/cracking). Pyrolyzing (i.e. oxidizing) conditions may be necessary to combust the alkanolamine organics into more volatile species during the thermolysis step. Unfortunately, as this work has shown, the use of more oxidizing conditions or higher WVT temperatures have proven too aggressive for the substrate and result in copper oxidation.

3.5 Implementation of Acac Solution Chemistry:

Currently, a route for extracting alkanolamine chelating ligands under mild enough conditions to allay copper substrate oxidation and prevent film cracking has not been discovered. However, this difficulty may be avoided by switching the solution to a chemistry that uses a more volatile (lower-boiling point) chelating agent. This section describes the first attempt at this approach where an acac-chelated solution chemistry was investigated.

3.5.1 Phase Analysis of PZT Films Derived from Acac Solution:

The acac molecule ($T_{B.P.} = 136^{\circ}\text{C}$) has a lower boiling point than the alkanolamines ($T_{B.P.} > 200^{\circ}\text{C}$) used previously. Thus, acac is expected to be extracted from the gel at a lower temperature. For this reason, lower temperature drying steps without thermolysis were examined as well as a 400°C WVT condition. XRD patterns for uncrystallized gels

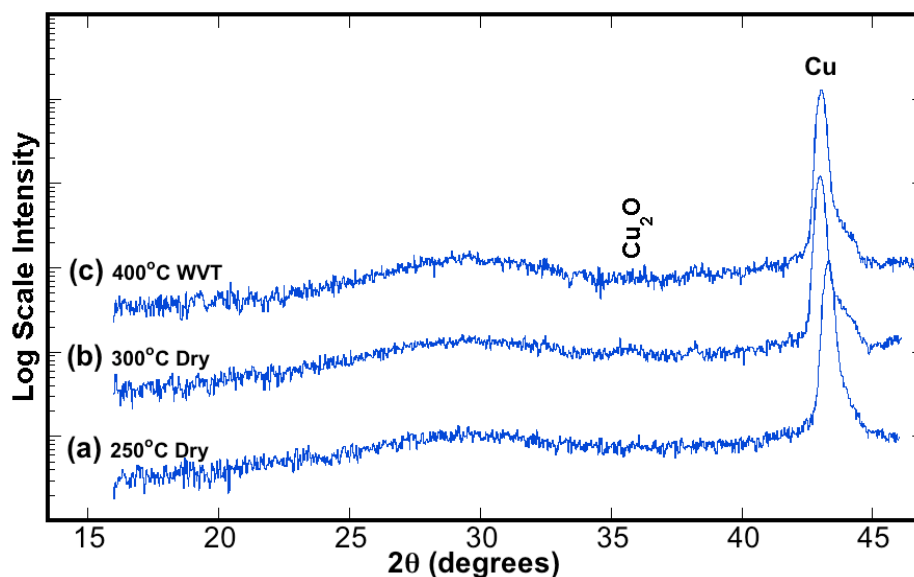


FIG 3-18 – XRD Analysis of Thermolysis Conditions for Acac Solution: *XRD data showing the gel state for acac solution derived films; (a) 250°C dry for 7.5 min, 4 layers, (b) 300°C dry for 7.5 min, 4 layers, (c) 400°C WVT for 15 min, 3 layers.*

are shown in Fig. 3-18. Samples processed in water vapor were found to crack during the fourth thermolysis step. Hence, WVT samples prepared for crystallization anneals contained only three layers. The samples that were only dried were heated on the hotplate for 7.5 min.

A comparison of the phase assemblage for crystallized films dried at 300°C and those thermolyzed in water vapor is given in Fig. 3-19. The water vapor thermolyzed samples show difficulty in crystallizing the perovskite phase and cracked during the annealing step (see Fig. 3-20) but contain minimal substrate oxidation. Comparatively, the 300°C dried samples consistently crystallize into the perovskite phase but contain substantial amounts of copper oxide. However, the 300°C dried samples have no visible cracks (Fig. 3-21). Initial electrical data was collected from these samples and is presented in the next section.

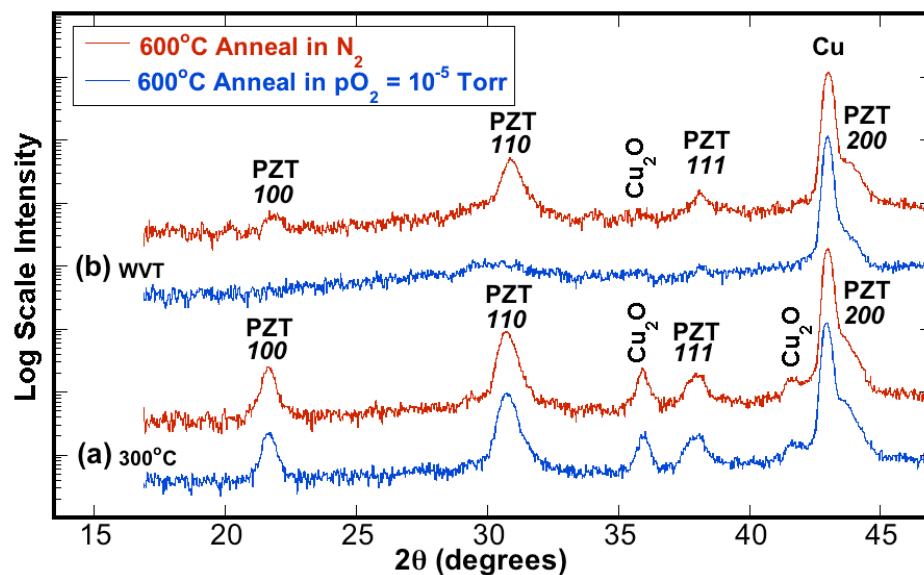


FIG 3-19 – Acac Solution Crystallization Behavior for WVT and 300°C Dried Films: XRD data collected for acac solution derived PZT films crystallized at 600°C in N₂ or 10⁻⁵ Torr pO₂ and thermolyzed with either (a) 300°C dry for 7.5 min or (b) 400°C WVT for 15 min.

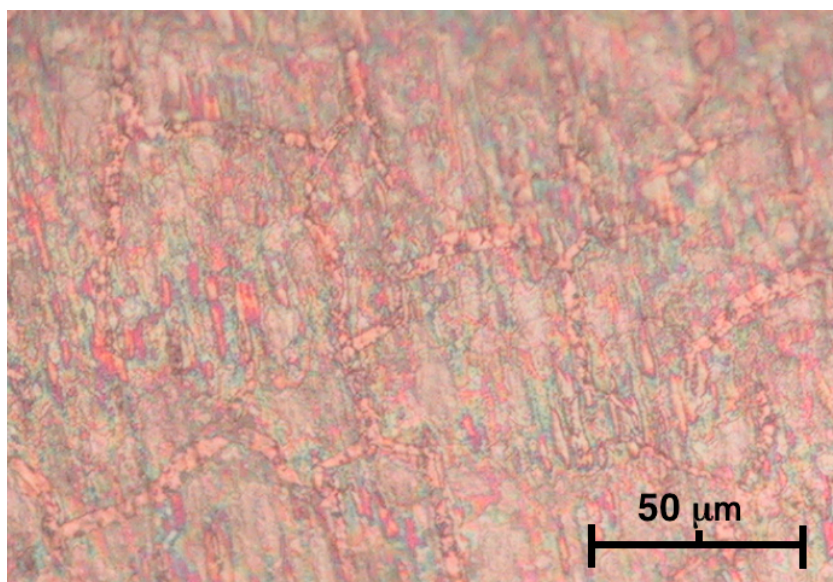


FIG 3-20 – Micrograph of WVT Acac Derived PZT Film Annealed in N₂: Optical microscopy image showing cracking in an acac solution derived 3-layer PZT film prepared with WVT and crystallized at 600°C in N₂. (Sample corresponds to the XRD pattern in Fig. 3-19b).

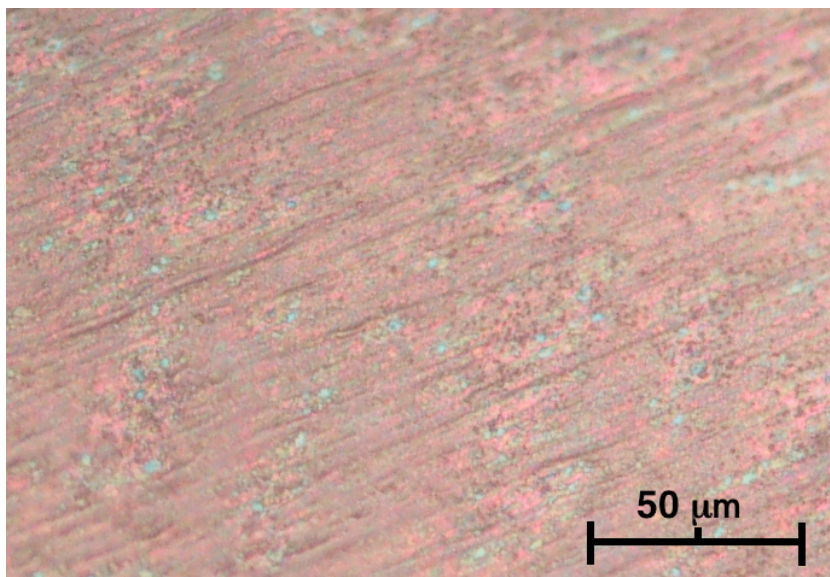


FIG 3-21 – Micrograph of 300°C Dried Acac Derived PZT Film: *Optical microscopy image showing acac solution derived 4-layer PZT film prepared with 300°C dry and crystallized at 600°C in nitrogen. (Sample corresponds to the XRD pattern in Fig. 3-19a).*

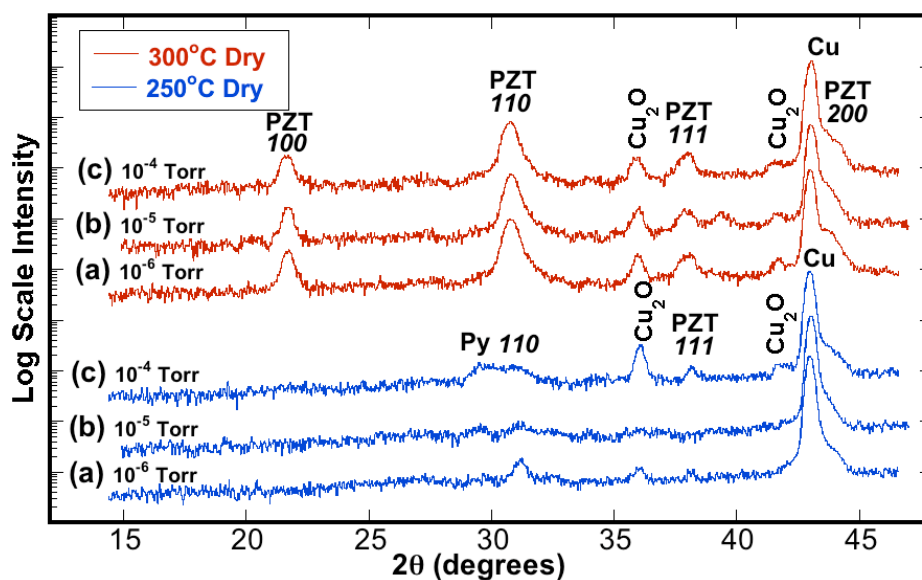


FIG 3-22 – Effect of pO_2 and Drying Temperature on Acac Derived PZT Films: *XRD data showing acac solution derived PZT films dried at 250°C and 300°C and then crystallized at 600°C in varying oxygen partial pressures; (a) 10^{-6} Torr pO_2 (b) 10^{-5} Torr pO_2 (c) 10^{-4} Torr pO_2 .*

In an attempt to reduce the amount of substrate oxidation, the drying temperature was reduced to 250°C. Unfortunately, as the data in Fig. 3-22 illustrates, this modification predominantly served to frustrate the crystallization of the perovskite phase. This figure also indicates that changes in the crystallization atmosphere for the 300°C dried samples had negligible impact on the final amount of substrate oxidation.

3.5.2 Electrical Data from Acac Derived PZT Films on Copper Foils:

This author's first recording of electrical properties from PZT thin films deposited directly on copper foils were measured on uncracked films derived from the acac solution chemistry. An example of the C-V behavior for such films is shown in Fig. 3-23.

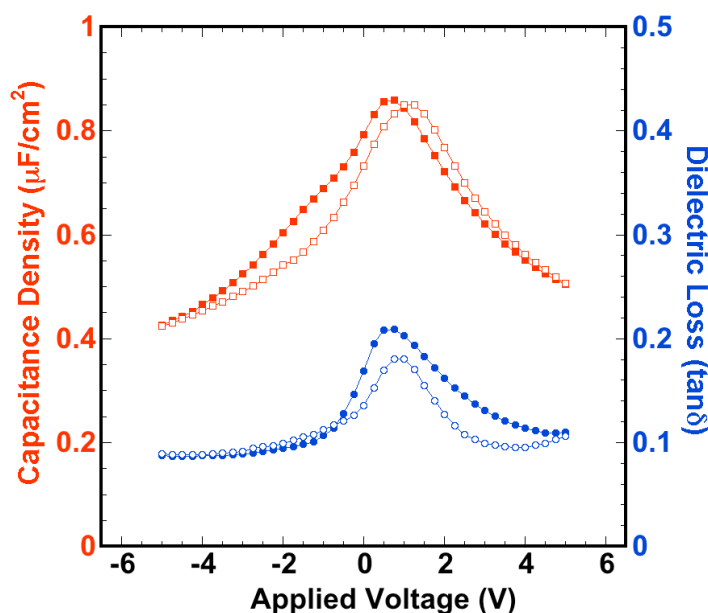


FIG 3-23 – Dielectric Tunability Data for Acac Solution Derived PZT Film on Cu: Plot of capacitance density and dielectric loss vs. applied voltage at 1 MHz & 25°C for acac solution derived 4-layer sample dried at 300°C for 7.5 min and fired at 600°C in a 10^{-5} Torr pO_2 vacuum atmosphere. (Sample corresponds to the data shown in Figs. 3-19a and 3-21).

This data unmistakably exhibits a hysteretic character and has a dielectric tunability of ~50%. The peaks in the dielectric loss appear indicative of domain wall motion. However, the magnitude of $\tan\delta$ is unacceptable for devices. Moreover, dielectric breakdown occurs at a mere 5 V. These deficiencies are certainly the result of the substantial copper oxide present in this system.

3.5.3 Implications of Acac Solution Chemistry Investigation:

The current data suggests that during thermolysis acac chelated films undergo a different decomposition route than EC films. The WVT data indicates that acac ligands may be difficult to hydrolyze in a non-oxidizing atmosphere. Thus, prior to crystallization these WVT films probably contain a significant organic fraction and an insufficient M-O-M network. During crystallization, either the organic fraction frustrates perovskite formation (Fig. 3-19b) or large cracks (Fig. 3-20) appear because the skeletal network lacks enough rigidity to maintain film connectivity during the volume shrinkage. This condition of strong acac chelation and high oligomer transparency is consistent with observations made by other groups [116].

In comparison, acac films that are processed at 300°C on the hotplate undergo sufficient pyrolysis to remove the chelating ligands and form a M-O-M network. Furthermore, unlike the EC solution, acac-chelated films undergo a different pyrolysis route, which appears to preclude Pb precipitation. A possible explanation may be that the Pb cation becomes acac chelated similar to the transition metal cations; however, spectroscopic evidence would be necessary to validate this claim. Regardless, upon crystallization these acac gels retain the necessary balance of compliance and stiffness to allow for proper densification without crack formation. Unfortunately, the 300°C pyrolysis condition is incompatible with the substrate and leads to massive copper oxidation. Attempts to lower the pyrolysis temperature only serve to increase the organic fraction and frustrate perovskite crystallization.

Thus, despite not achieving the ultimate goal of PZT directly on copper without an interfacial layer, this investigation reveals that changing the B-site cation chelating ligand

can influence the extent of organic removal and the PZT crystallization route. Because of its lower volatilization temperature and different crystallization route, acac-modified films can be processed without cracking. However, because acac strongly chelates with the metal cations, its removal on the hotplate requires a temperature that is incompatible with the copper substrate. Thus, a weaker chelating agent with volatility similar to acac is necessary to obtain organic extraction conditions that are compatible with a copper substrate.

4. Development of a CSD Process for Synthesizing Device Quality PZT Films on Copper Surfaces

Based on the conclusions of Chapter 3, a processing route that relies on a solution chemistry with an easily hydrolysable chelating agent—specifically acetic acid—is pursued in this chapter. To improve the quality of the PZT material and accelerate process development, a suitable, well-characterized solution chemistry is chosen from the literature. After reviewing this chosen solution chemistry, this chapter describes the systematic development of film processing parameters that prevent oxidation of the copper substrate while circumventing crack propagation in the PZT film. PZT films processed directly on copper substrates under these conditions are shown to exhibit ferroelectric responses comparable to examples of well-prepared material in the literature.

4.1 The Inverted Mixing Order PZT Solution Chemistry:

The inverted mixing order (IMO) PZT solution chemistry developed by R. W. Schwartz and colleagues during the early 1990s at Sandia National Laboratories ideally fits the needs of this thesis. First, extensive work has been published concerning this solution chemistry and its effects on the resulting PZT microstructure and electrical properties. Second, optimized conditions have been determined for preparing PZT material from this solution with device-quality properties. Third, it is synthesized using a simple hybrid sol-gel method with acetic acid chelation. This section will review the relevant work on IMO CSD PZT films as well as describe the exact methodology adopted for use in this thesis.

4.1.1 Previous Characterization of IMO Derived PZT Thin Films:

In 1992 Schwartz *et al.* reported that PZT films synthesized from a hybrid sol-gel solution prepared using an inverted mixing order (IMO) exhibited superior phase assemblage, dielectric properties, and ferroelectric response compared to films prepared from a sequential precursor addition (SPA) solution, despite both solutions having

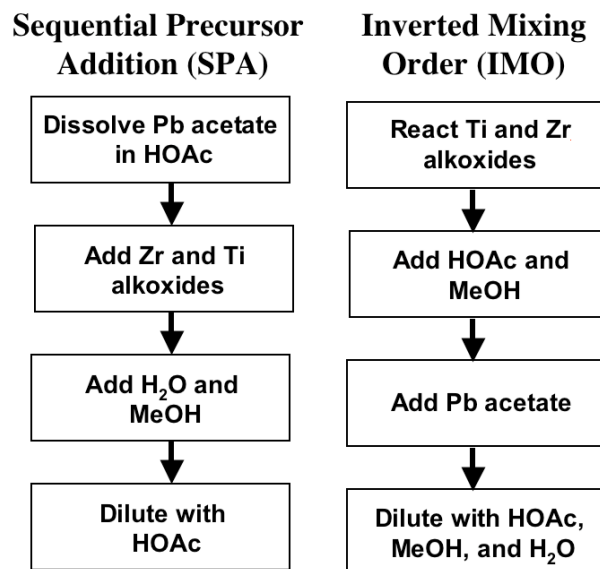


FIG 4-1 – Comparison of SPA and IMO Solution Preparation Procedures: *Flow charts for PZT solution synthesis using different mixing orders [117, 118].*

extremely similar chemistries [118, 119]. (See Fig. 4-1 for differences in solution preparation). Plan view SEM [118] and cross-sectional view TEM [119] revealed that films prepared using the SPA solution contained a surface layer of large, rosette-shaped perovskite grains in a residual pyrochlore matrix with an underlying columnar perovskite structure. In contrast, IMO derived films had a predominantly columnar perovskite structure with little pyrochlore. Because the IMO films contained a perovskite phase assemblage with less grain boundary density, its dielectric and ferroelectric properties were superior. The dielectric constant for IMO derived films was twice that of the SPA films and the P-E loops showed better saturation and squareness—indicative of less leakage and less domain wall pinning.

An FTIR investigation revealed that greater amounts of esterification occur during SPA solution preparation relative to IMO solution synthesis [118]. Since water is a byproduct of esterification, it is suggested that precursors become more hydrolyzed, pyrolysis temperature is reduced, and surface nucleation is facilitated [98].

FTIR data also suggests that the acetic acid in these solutions completely replaces the alkoxide ligands to form oxo acetate precursor species [118, 119]. This hypothesis was further investigated by NMR examinations of dried solution powders. Without solvent, the NMR detection of only acetate ligands verified the full chelation [117, 118].

Continued esterification is believed to age the solution and influence the film's final microstructure. The solution lifetime—or the amount of time over which a solution can be used to deposit film's of similar quality—is approximately 10 to 15 days [116, 120]. As the solution ages, increasing amounts of surface nucleation events are observed, forming large spherical perovskite grains on top of the interface-nucleated columnar structure. These microstructural changes degrade the reproducibility of the dielectric / ferroelectric properties [120]. FTIR and NMR studies of the solution and precursor species indicate that as the solution ages, metal cations lose acetate ligands and oligomerize into larger precursors. As a consequence, the precursors pack less efficiently in the gel and the green-body film thickness is observed to increase with solution age. However, if films are prepared from aged solutions with less layers, the microstructure is observed to replicate that of a fresh solution. Hence, it is concluded that only the thickness, and not the intrinsic change in precursor structure, affects the film's final microstructure [120].

Two methods have been identified for maintaining reproducible properties from aged solutions. One method is vacuum distillation of solutions—removing all volatile constituents and leaving an unreactive precursor powder*. Films processed from 200-day old powders redissolved in an appropriate solvent have been shown to exhibit microstructures and properties comparable to fresh solutions [120]. Alternatively, the chelating agent acetylacetonone (acac) can be added to aged solutions immediately prior to deposition [116]. Spectroscopy studies indicate that acac is a stronger chelating agent than acetic acid and replaces HOAc as a chelating ligand for B-site cations. The higher pyrolysis temperature of acac increases the barrier to nucleation, thereby reducing surface nucleation. Acac to PZT molar ratios of 1:1 and 2:1 minimize surface nucleation while

* Powders must be stored under inert or dry atmospheres (< 25% humidity).

molar additions of 3:1 eliminate this nucleation event. Because this grain boundary is eliminated near the surface, films prepared with acac additions have improved ferroelectric and dielectric response in MIM geometries, even in comparison to unaged IMO solutions. However, the acac-modified solution ages quickly—as verified by FTIR spectroscopy—and within ~2.5 hrs precursors contain too many acac ligands. Upon pyrolysis, these highly transparent precursors consolidate but fail to form an adequate M-O-M network to withstand the volume shrinkage of drying and crystallization. Consequently, these films crack [116].

4.1.2 IMO Solution Preparation:

The acetic acid chelation PZT solution chemistry used in the current experiments is modeled after the inverted mixing order (IMO) process described by Schwartz and Assink [117]. The premise of this chemistry is to first react the B-site precursors and then dissolve the Pb source (Fig. 4-1). To begin, appropriate molar ratios of zirconium propoxide (2.331 mL, 0.0052 mol Zr) and titanium isopropoxide (1.417 mL, 0.0048 mol Ti) were reacted in a dry environment for 5 or 10 min. (Note that the titanium source was always added to the zirconium source.) All reactions were carried out in an open beaker and stirred at 500 rpm. The humidity of the environment is crucial since reactions with water (hydrolysis/condensation) may influence the precursor structure. Humidity levels below 20% were found to be favorable. After reacting the precursors, 2.31 mL of glacial acetic acid (99.99+% purity, Sigma-Aldrich)—a 4:1 molar ratio with the B-site cations—was added for chelation. After 6 min, 5 mL of MeOH was added to quench the reaction. Currently, these steps are believed to be crucial in influencing the final solution behavior.

After stirring for 5 min, the solution was removed from the dry environment and placed on a 90°C hotplate. Lead acetate trihydrate (4.362 g, 0.0115 mol Pb) was added and stirring (500 rpm) was continued for 16 min. The heat was then turned off and 5 mL of MeOH was added. After 2 min, 2.5 mL of acetic acid was added; then 2 min later 5 mL of MeOH; followed by an additional 2.5 mL of acetic acid 2 min later. The solution was stirred for another 5 min, and then 3 mL of distilled H₂O was added drop by drop. The

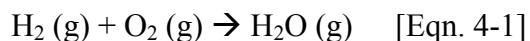
final solution was designed to be about 0.4 M in concentration. Films spun from pure IMO solutions were prepared within 15 days of initial solution synthesis to limit the effects of solution aging. In some experiments, acac was added to the IMO solution. For such situations, a ratio of 3 moles of acac to 1 mole of PZT was mixed immediately prior to deposition as is recommended by Schwartz *et al.* [116].

4.2 Procedures for PZT Thin Film Preparation:

The procedures for processing PZT thin films from the IMO solution are similar to those used in Chapter 3. The solution was deposited through a 0.2 μm filter and spun at 3000 rpm for 30 seconds on an 18 μm thick Cu foil. A 20 second spin time was also investigated. The foil was then immediately dried on the hotplate at between 200°C and 325°C for 2.5 to 7.5 min. Standard procedures were a 250°C dry for 5 min. In some cases the drying step was followed by a 400°C thermolysis step in the 2-inch diameter controlled atmosphere tube furnace for 15 min. Atmospheric conditions consisted of flowing nitrogen or flowing forming gas (1% H₂ + 99% N₂). Gases were flowed through an unheated water bubbler at ~1 slm. Prior to thermolysis, the sample was held in the closed atmosphere tube furnace for 5 min to allow the atmosphere to reach steady state. The samples were also left in the atmosphere to cool. These spinning/drying/thermolizing processes were repeated until the desired film thickness was reached—typically 4 or 5 layers.

After the gel was processed to its desired thickness, the film was crystallized in the same controlled atmosphere tube furnace. Again the sample was held in the desired atmosphere for 5 min before entering the hot-zone, and after firing it was allowed to cool in the same atmosphere. The annealing profile typically included a ramp from an initial temperature of ~200°C-300°C to a final temperature of 650°C; it was held at 650°C for 30 min and then immediately removed from the hot-zone. This furnace profile was modeled after the conditions reported by Schwartz *et al.* [118]. Final annealing temperatures of 600°C and 700°C were also investigated. Crystallization atmospheres consisted of flowing nitrogen, flowing forming gas or a mixture of nitrogen and forming gas. The

nitrogen/forming gas mixture was utilized to control the oxygen partial pressure via Le Chatelier's principle and the following reaction:



Using this mixture at 650°C, the oxygen partial pressure was maintained at 1.3×10^{-14} Torr (1.7×10^{-17} atm) and monitored with a solid-state oxygen sensor. At this temperature, this oxygen partial pressure is sufficient to reduce Cu_2O to Cu metal.

4.3 Investigation of Process Parameters:

From the previous research of Schwartz and colleagues, it was determined that high-quality PZT can be obtained from the IMO solution if a 300°C hotplate step followed by a 650°C anneal in air is used. Unfortunately, from the previous work discussed in Chapter 3, these conditions are expected to be too aggressive for the copper substrate. Thus, this section investigates a range of drying temperatures and annealing conditions to determine a process window that is also compatible with the copper substrate.

Note that this section discusses a hypothesis concerning the decomposition of gel organics as a source of copper substrate oxidation. In a later section, the validity of this hypothesis will be discussed and contrasted with a competing hypothesis. However, because this hypothesis was used to direct the investigation of processing parameters, it is included in this section to elucidate the methodology of this research.

4.3.1 Drying Temperature:

An XRD series of 4-layer samples dried for 5 minutes at different temperatures is presented in Fig. 4-2. This data shows a similar trend to films processed with EC and acac solutions. If drying is performed below ~250°C, then copper oxidation is mitigated. If the drying temperature is raised above ~250°C, the substrate oxidizes during the drying step. Since the premise of this work assumes that thermodynamic equilibrium will not be

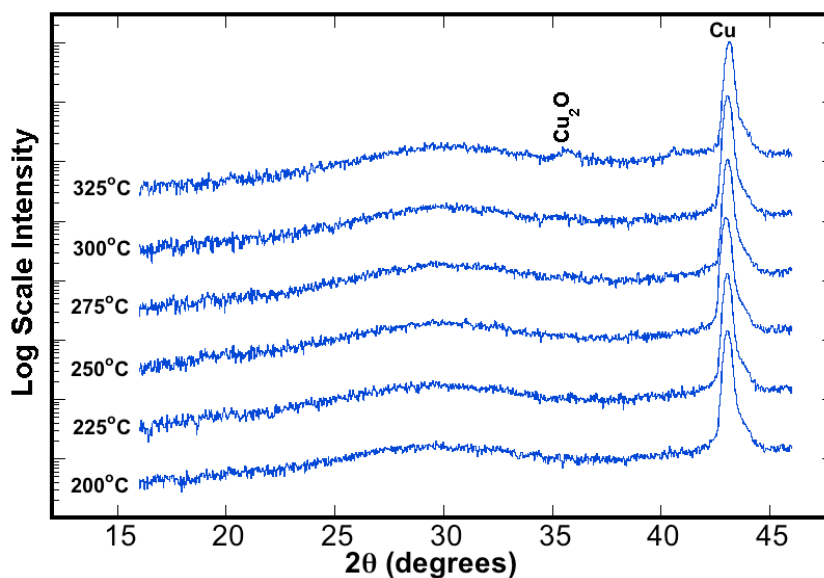


FIG 4-2 – XRD Analysis of Substrate Oxidation During Drying of IMO Derived Gels: XRD patterns indicating the amount of Cu_2O present after drying 4-layer IMO PZT gels at varying temperatures (200°C to 325°C) for 5 min.

reached in the final annealing step, it is crucial to maintain a process that never allows Cu_2O to form. Thus, it is determined that a drying step of $\leq 250^\circ\text{C}$ is necessary to avoid substrate oxidation.

4.3.2 Crystallization Atmosphere:

The drying series was crystallized at 650°C under three different flowing atmospheric conditions: (1) reagent grade nitrogen, (2) forming gas and nitrogen mixture (1.3×10^{-14} Torr pO_2), and (3) pure forming gas. The XRD results of this study are presented in Figs. 4-3 to 4-5. Samples annealed in N_2 and at 1.3×10^{-14} Torr pO_2 (Figs. 4-3 and 4-4) have similar phase assemblages—particularly in the amount of Cu_2O at each drying temperature. This observation led to the initial hypothesis that substrate oxidation is not only a function of atmospheric O_2 content but also the oxygen content of the organics. An atmosphere of 1.3×10^{-14} Torr pO_2 at 650°C cannot oxidize Cu metal (see Fig. 1-16).

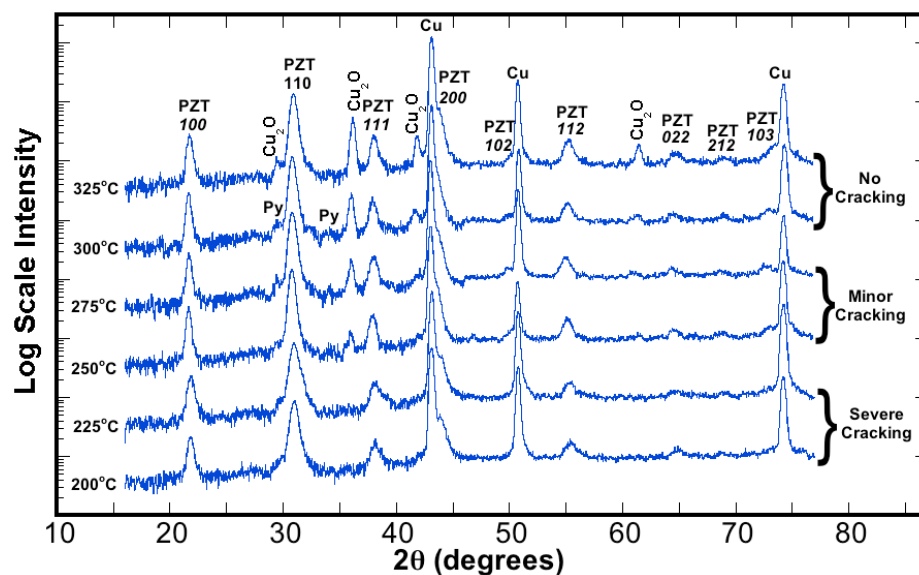


FIG 4-3 – XRD Analysis of IMO Drying Series Crystallized in Nitrogen: XRD scans that show the drying series (Fig. 4-2) crystallized at 650°C in flowing nitrogen.

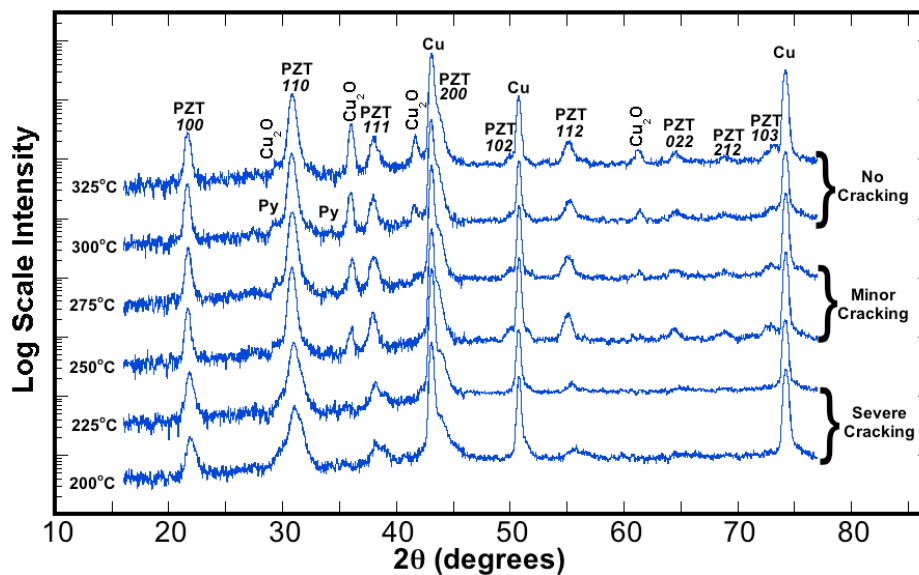


FIG 4-4 – XRD Analysis of IMO Drying Series Crystallized in $pO_2 = 1.3 \times 10^{-14}$ Torr: XRD scans that show the drying series (Fig. 4-2) crystallized at 650°C in a controlled pO_2 environment of 1.3×10^{-14} Torr, which is sufficient to reduce Cu_2O to Cu metal.

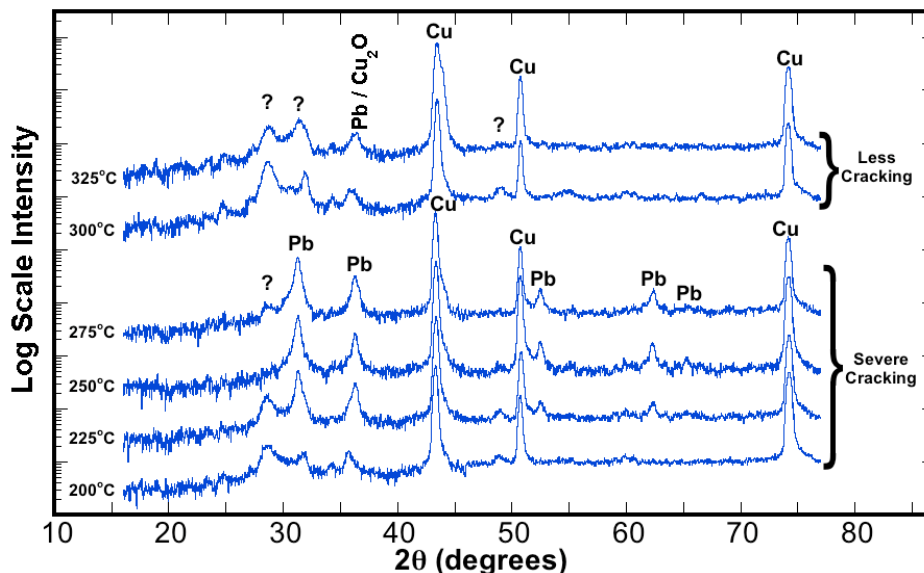


FIG 4-5 – XRD Analysis of IMO Drying Series Crystallized in Forming Gas: *XRD scans that show the drying series (Fig. 4-2) crystallized at 650°C in an atmosphere of flowing forming gas containing 3% H₂.*

Accordingly, the samples annealed at 1.3×10^{-14} Torr pO₂ are expected to exhibit less substrate oxidation than those annealed in N₂. However, the data suggests that both atmospheres result in equivalent amounts of oxidation. This observation led to the hypothesis that organic decomposition is a source of substrate oxidation. Also note that the presence of Cu₂O in Fig. 4-4 verifies the assumption that thermodynamic equilibrium cannot be reached in the PZT/Cu system for standard annealing conditions (650°C, 30 min).

The second metric that must be evaluated is film cracking. Again, the N₂ and 1.3×10^{-14} Torr pO₂ annealed samples exhibit a similar behavior. Both of these sets of films show a reduction in film cracking with increasing drying temperature. This decrease in cracking is demonstrated in Fig. 4-6. In this system, cracking is believed to primarily be a result of insufficient consolidation of the gel prior to crystallization. Extraction of residual acetate ligands may also contribute. Both of these problems, though, are expected to improve with increasing drying temperature, which is consistent with the observed results.

Interestingly, the severely cracked films (200°C and 225°C dry) have undetectable levels of Cu_2O despite having large cracks that expose the substrate to the atmosphere. This observation appears to support the hypothesis that the atmosphere is not the primary source of substrate oxidation.

Finally, the samples crystallized in pure forming gas (3% H_2 , balance N_2) completely lack the proper phase assemblage (Fig. 4-5) and are severely crack (Fig. 4-7). However, this experiment does provide evidence that this system, like the EC chemistry, can exhibit Pb metal reduction / precipitation. However, in this case Pb has only precipitated under extremely reducing conditions. Proper identification of the other phase(s) present is currently unclear. Possible matches are a Pb/Zr/Ti pyrochlore/fluorite structure or a form of PbO (Litharge).

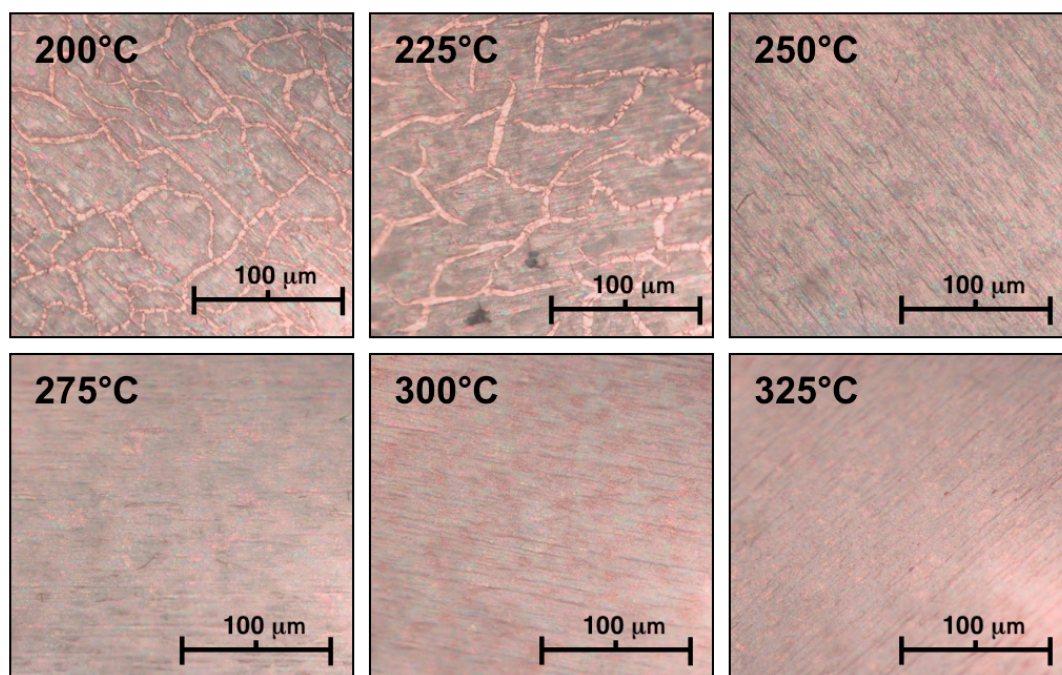


FIG 4-6 – Micrographs of PZT Films Dried at Various Temperature and Crystallized in Nitrogen: *Optical micrographs showing PZT films from the IMO drying series that were crystallized in nitrogen (correspond to the XRD patterns in Fig. 4-3).*

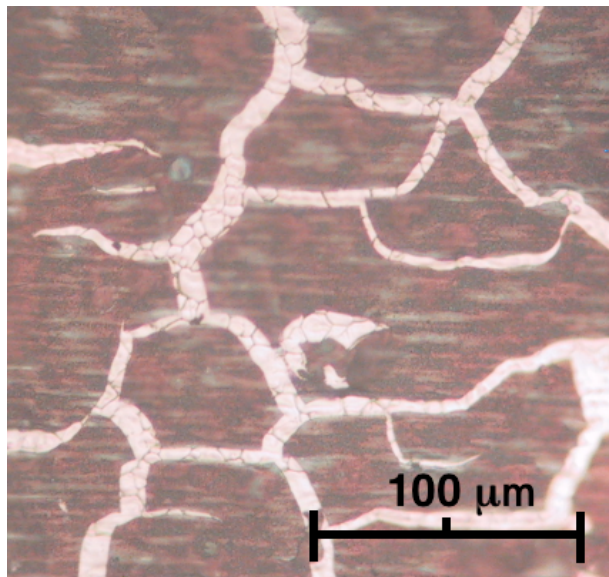


FIG 4-7 – Micrograph of PZT Film Crystallized in Forming Gas: *Optical microscopy image showing an IMO PZT film that was dried at 250°C and crystallized in forming gas. This image is representative of the severe cracking observed when films were crystallized in this atmosphere.*

4.3.3 Investigation of Thermolysis Conditions:

Based on the hypothesis that substrate oxidation is attributed to organic decomposition, a thermolysis step was introduced to more completely remove the organic constituents prior to crystallization. In the previous section, the removal of the organics in a single step (i.e. during the crystallization anneal) is believed to trap many of the organics near the interface during decomposition, thereby facilitating copper oxidation. Alternatively, if organic removal were to occur on a thin enough layer, the lower concentration of organic species and their proximity to the atmosphere may encourage volatilization relative to substrate interaction.

To investigate this supposition, two samples were prepared: (1) 250°C dry / 400°C thermolysis in N₂ on every layer and (2) 250°C dry / 400°C thermolysis in 1% H₂ forming gas on every layer. Both of these samples were then crystallized at 650°C in flowing N₂.

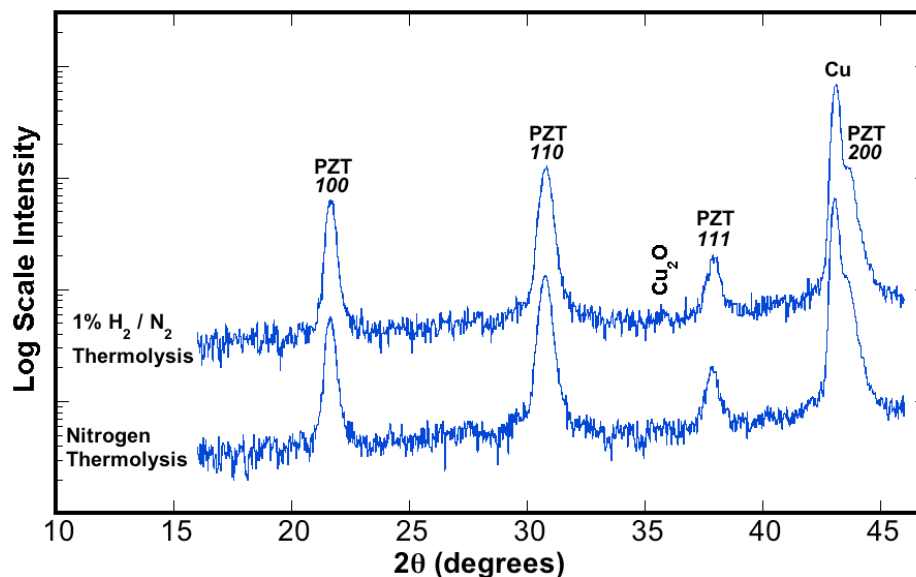


FIG 4-8 – XRD Comparison of PZT on Cu Samples Thermolyzed in N_2 and 1% H_2 / N_2 : XRD scans showing the reduction in Cu_2O formation that occurs when a $400^\circ C$ thermolysis step is included in the processing of 4 layer IMO PZT films. These films were crystallized in flowing nitrogen at $650^\circ C$.

The XRD analysis of these crystallized samples is given in Fig. 4-8. As this data indicates, the thermolysis step has resolved the problem of substrate oxidation—the 111 Cu_2O reflection is virtually undetectable in both of these samples.

Despite this success, electrical data could still not be collected from these samples. Most of the investigated electrodes were shorted. A few ($< 10\%$) showed some response at zero bias but quickly broke down with the application of a small dc voltage ($< 5V$). These results appear to indicate a cracking problem. However, an optical microscopy investigation was not conclusive in determining the existence of significant cracking. The image shown in Fig. 4-9 demonstrates the possibility of 5 to 10 μm sized cracks, but even these defects appear infrequently. This experiment was repeated three times with similar result. Thus, currently it is believed that some form of micro-cracking is occurring in these films. This conclusion is consistent with the fine cracks observed in Fig. 4-6 for films dried at $250^\circ C$. The thermolysis step may provide some additional structural relaxation in the gel, but it is reasonable to expect that the associated gel consolidation remains

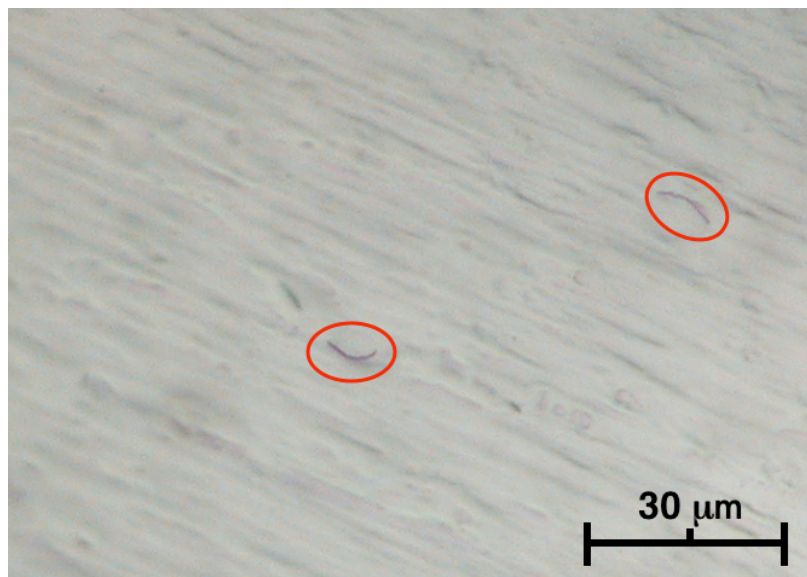


FIG 4-9 – Micrograph of Cracking in Completely Thermolyzed IMO PZT Films: *Optical microscopy image showing the existence of minor cracking in 5 layer IMO films prepared using a 250°C dry and 400°C thermolysis on each layer. Image taken on a platinized region to enhance cracking contrast.*

inadequate to completely alleviate film cracking. Thus, this data may be more evidence to support the hypothesis that the gel consolidation necessary to relieve cracking upon crystallization is primarily determined by the hotplate step.

4.4 The 2 + 3 Composite Gel Architecture:

The previous section's exploration of process parameters reveals that copper oxidation can be minimized for IMO derived films when a $\leq 250^\circ\text{C}$ hotplate dry and a thermolysis step are employed. Unfortunately, such films continue to exhibit minor cracking problems. In this section a composite gel architecture is implemented to realize the reduced Cu_2O formation from thermolyzed layers while gaining increased gel consolidation through the use of higher drying temperatures on subsequent layers.

4.4.1 Implementation of 2 + 3 Method:

Thermolysis of IMO PZT gels fails to resolve cracking problems associated with a 250°C drying step. Gel consolidation is hypothesized to be essentially completed by the end of the drying step. This assumes that gel consolidation completely depends on solution chemistry, spinning conditions, and drying parameters. This assumption is somewhat rationalized by previous reports that the solvent and acetate ligands are removed by 300°C [98]. The thermolysis condition is believed to remove any remaining organic species and stiffen the gel network through increased M-O-M bond formation. If the volume change upon crystallization is large, then sufficient stresses to crack the densifying film can result. Although cracking was not explicitly discussed in their work, the above reasoning may explain why Schwartz and colleagues routinely dry IMO-derived films at temperatures $\geq 300^\circ\text{C}$.

To resolve this cracking issue, a composite gel architecture is devised. In this scheme, initial layers are dried and thermolyzed to gain the advantage of an oxide free interface, while subsequent layers are only dried at a favorable consolidation temperature (300°C) to reduce total volume shrinkage and minimize stresses during crystallization. For the standard fresh IMO solution and normal spinning conditions, two thermolyzed layers were found to be sufficient to maintain interface integrity; oxidation occurred for one thermolyzed layer (Fig. 4-10). Two or three additional dried layer eliminated cracking; however, cracking reinitiated with a fourth dried layer. Thus, a 2 + 3 layer approach was deemed optimal—two 250°C dried / 400°C thermolyzed layers followed by three 300°C dried layers. Crystallization was carried out at 650°C in flowing nitrogen. Note that although a full solution aging study has yet to be completed, current data suggests that at a solution age of ≥ 6 days, the film becomes too thick and 2 + 3 layer films prepared from pure IMO solutions crack upon crystallization. However, for the same solution, a 2 + 2 layer film was uncracked.

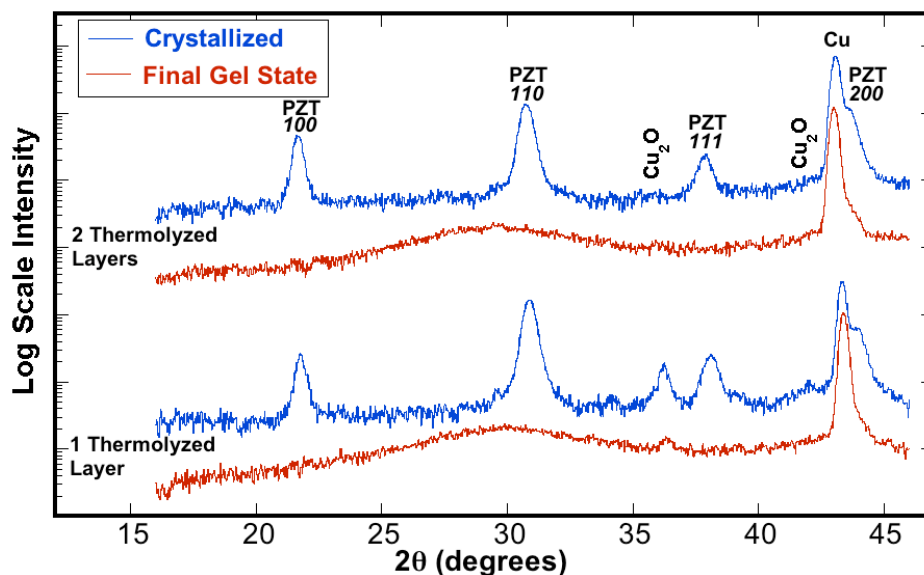


FIG 4-10 – XRD Comparison of 1 + 4 Process to 2 + 3 Process: *XRD data showing the difference in substrate oxidation as a result of using 1 thermolyzed layer vs. 2 thermolyzed layers.*

To verify that chelating agent selection is an important component in the success of the composite gel architecture, the 2 + 3 layer method was implemented with the EC solution. Results are displayed in Fig. 4-11. Not surprisingly, XRD does not detect Cu_2O . However, the films are cracked (Fig. 4-12). Again, this cracking is probably a result of the inability to successfully hydrolyze / volatilize the alkanolamine chelating agents prior to crystallization. This result confirms the importance of solution chemistry selection when designing a processing route for depositing PZT on copper.

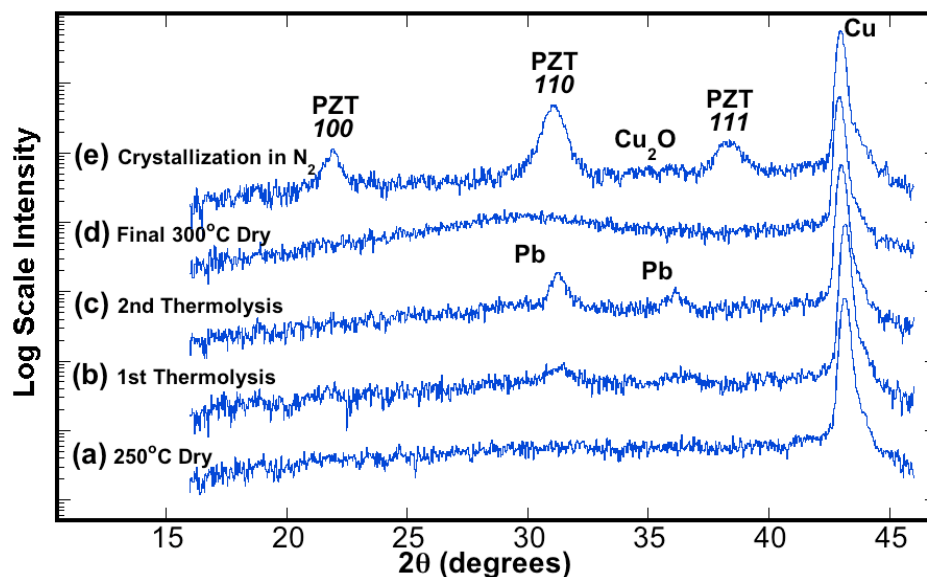


FIG 4-11 – Phase Development in EC Derived Films Using the 2 + 3 Methodology: XRD scans showing the phase development in a PZT film when the 2 + 3 layer method is applied to the EC solution chemistry; (a) 250°C dry, (b) 1st pyrolysis at 450°C in forming gas, (c) 2nd pyrolysis, (d) after final dry (5th layer), (e) crystallized in flowing N₂ at 650°C.

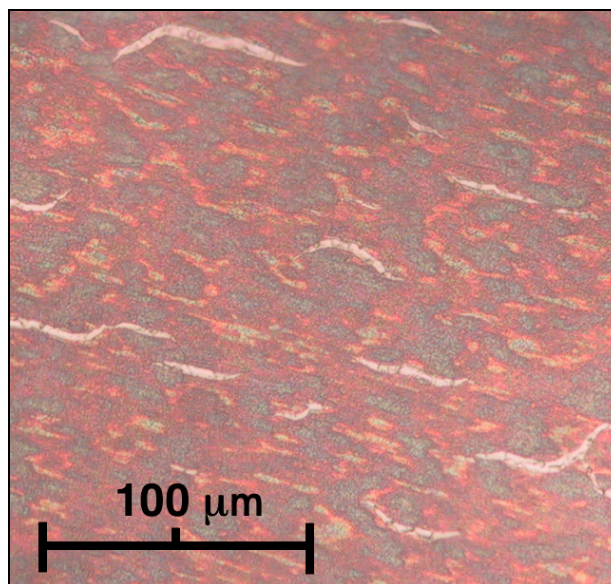


FIG 4-12 – Micrograph of 2 + 3 Processed PZT Film Using the EC Solution Chemistry: Optical microscopy image showing the cracking that occurs in EC derived PZT films that are processed via the 2 + 3 layer method.

4.4.2 Electrical Data from 2 + 3 Processed PZT Films on Copper Foils:

Dielectric and polarization measurements were conducted on PZT films prepared on copper foils using the 2 + 3 layer approach with a subsequent anneal at 650°C in flowing N₂. Note that the electrical data presented in this section was collected using the same film that underwent XRD analysis in Fig. 4-10. Fig. 4-13 demonstrates the dielectric tunability of this film at 10 kHz and room temperature. At this frequency the tunability is ~58% over an applied field of ~200 kV/cm. The relative permittivity peaks at ~800. The dielectric loss remains below 5% at all fields and drops to below 2% in the intrinsic regime. These tan δ values approach device-quality and help to verify the integrity of the PZT/Cu interface. Furthermore, these dielectric values are comparable to the dielectric constant of 835 and dielectric loss value of 3% originally reported by Schwartz *et al.* for IMO PZT films prepared on platinized silicon [118]. The similarity in dielectric constant provides confidence that these measurements are truly of a PZT film rather than a PZT film in series with a low dielectric constant interfacial layer, which would reduce the observed permittivity through the series capacitance law.

Dispersion data along with C-V loops taken at each decade are presented in Fig. 4-14. The permittivity has ~18% dispersion over three decades (1 kHz to 1 MHz) and neither the permittivity nor the dielectric loss exhibit space charge contributions. Furthermore, C-V loops exhibit good saturation across this frequency range with low dielectric losses (< 5%) at high applied fields. This saturating permittivity is indicative of an intrinsic response. If a poor PZT/Cu interface existed with active electronic defects, the dielectric response would be artificially enhanced and saturation would not be expected. Moreover, these electronic defects could cause unwanted leakage currents, especially at lower frequencies, and result in high dielectric loss at high fields. Thus, this performance is further evidence of high film quality.

A polarization hysteresis loop for a 2 + 3 processed IMO PZT film is shown in Fig. 4-15. These P-E loops exhibit high-field saturation, indicative of a high-quality ferroelectric film. Furthermore, the measured remanent polarization of 26 $\mu\text{C}/\text{cm}^2$ is

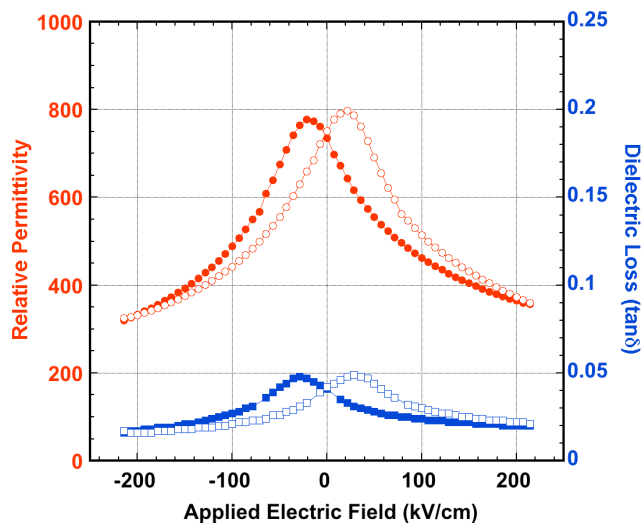


FIG 4-13 – Dielectric Tunability of a 2 + 3 Layer Processed IMO PZT Film on Copper: Plot of ϵ' and $\tan\delta$ vs. applied electric field obtained at 10kHz and room temperature for an IMO derived PZT film deposited directly on a copper foil.

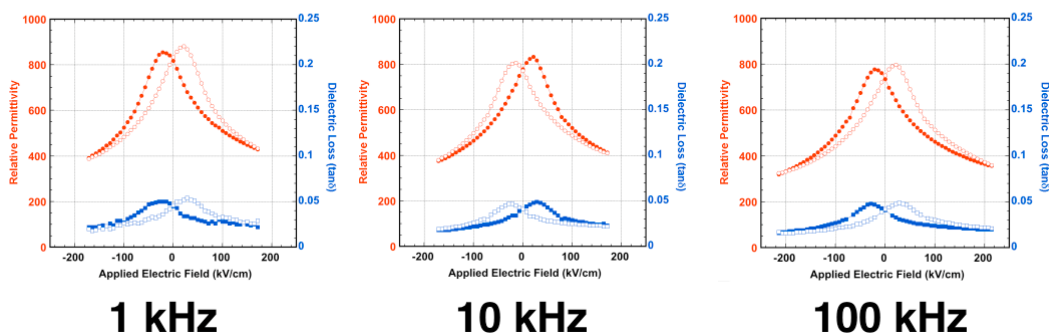
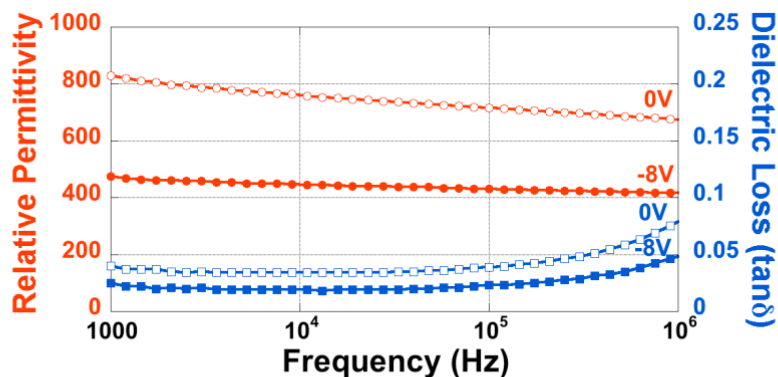


FIG 4-14 – Dielectric Dispersion of a 2 + 3 Layer Processed IMO PZT Film on Copper: Dispersion plot taken at room temperature for an IMO derived PZT film deposited directly on a copper foil taken at zero bias and $-8V$. C-V loops at varying frequencies are also included.

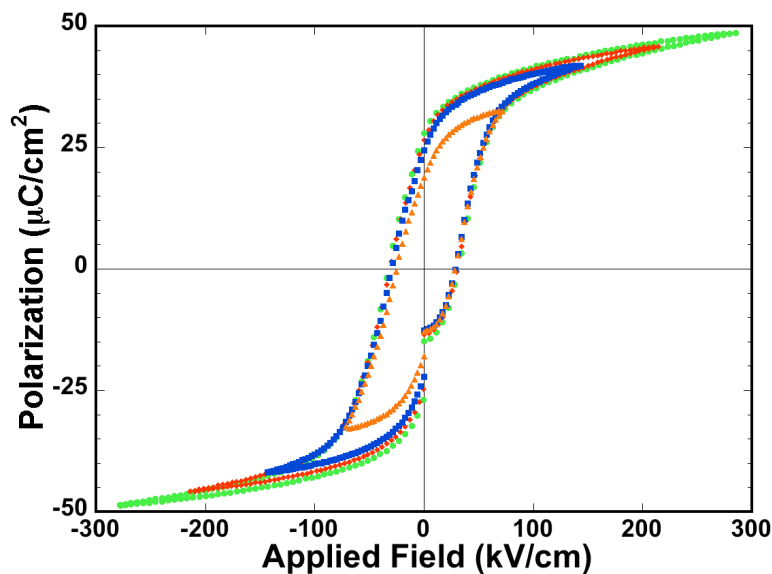


FIG 4-15 – Ferroelectric Response of a 2 + 3 Layer Processed IMO PZT Film on Copper: Plot of P - E loop taken at 100 Hz for an IMO derived PZT film deposited directly on a copper foil.

equivalent to the value of $26 \mu\text{C}/\text{cm}^2$ reported by Schwartz *et al.* for similar IMO-derived PZT films on platinized silicon [118]. The coercive field for this material is approximately 30 kV/cm, which is 30% less than the value of 43 kV/cm reported by Schwartz *et al.*

As a final metric, an IMO derived PZT film was prepared on a platinized silicon substrate. A 4 layer, 300°C dried sample was prepared (5 layers cracked) and crystallized at 650°C in flowing nitrogen conditions to mimic the PZT on Cu conditions. A comparison of the polarization response for the film on platinized silicon to that of a 2 + 3 layer processed PZT film on a copper foil is presented in Fig. 4-16. As this figure demonstrates, the response of the PZT is similar for both substrates. This similarity validates the impressive quality of this PZT/Cu system.

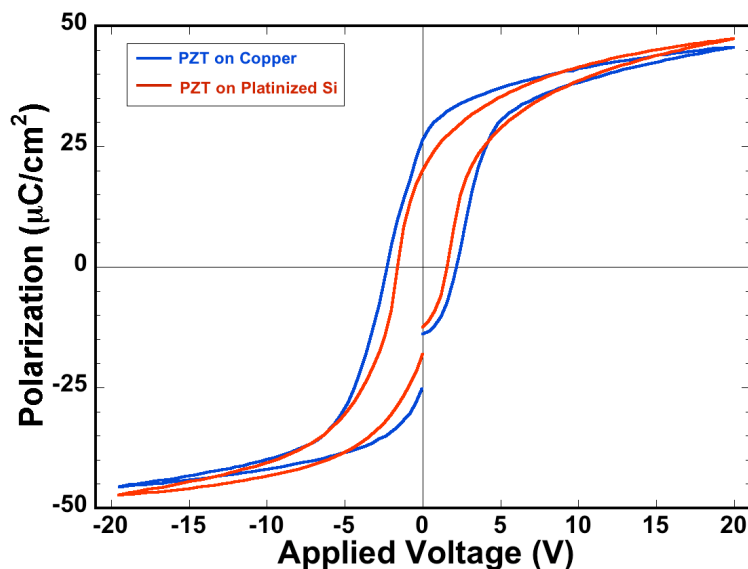


FIG 4-16 – Comparison of Ferroelectric Response from PZT Films Prepared on Cu and Si: *P-E loops taken from PZT films prepared from the same IMO solution on a copper foil and a platinized silicon substrate. Both films were crystallized in a N_2 atmosphere.*

4.4.3 Reproducibility and Attempts to Expand Processing Window:

To date, the results of the 2 + 3 process with an IMO film have been replicated thrice with completely separate solutions. A comparison of the P-E responses for each of these films is given in Fig. 4-17. This result indicates that the 2 + 3 methodology is a repeatable process; the variations in polarization response may reflect differences in solution age, Zr/Ti ratio, or errors in measuring the electrode area.

Despite this promising result, reliability of the process remains an issue. Although most (80-90%) electrodes ($\sim 200 \mu\text{m}$ diameter) from a 2 + 3 layer processed film will exhibit a reasonable electrical response at zero bias, a comparatively smaller fraction (5-20%) will show acceptable response at high fields. Furthermore, optimal electrical data is often concentrated in certain regions of the film, seemingly indicating a variation in the processing conditions across the sample surface. These observations indicate an uncontrolled process variable. Currently, the initial layer / drying step is under suspicion.

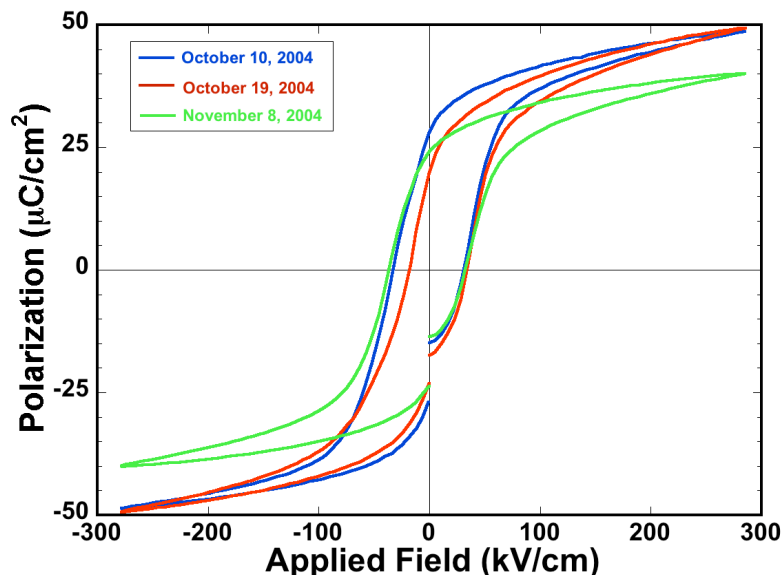


FIG 4-17 – Ferroelectric Response Comparison Showing Reproducibility of 2 + 3 Layer Process: *Three different PZT films on Cu deposited from different batches of IMO solution and prepared using the 2 + 3 layer method. The dates simply indicate when each sample was prepared.*

After a 250°C dry the film often has a non-uniform color / appearance. Although this may simply be thickness variations, it may also indicate spatial changes in film / substrate interaction. An example of this distinctive change upon a 250°C dry is illustrated in Fig. 4-18.

The success of the 2 + 3 layer approach indicates that controlling the interface relies on controlling the processing of the initial layer(s). If a proper interface can be formed initially, it is likely that the successive layers / processing steps will have little impact on the final interfacial quality. Thus, attempts have been made to homogenize the film's appearance after this first drying step. Various parameters have been investigated including:

- (1) Lowering the 2-layer drying temperature to 200°C, 225°C and 240°C
- (2) Drying the first two layers for only 2.5 min
- (3) Drying the first two layers in an open air tube furnace at 300°C for 5 min

- (4) Eliminating the drying step for the first two layers and only thermolyzing at 400°C in forming gas
- (5) Spinning at 3000 rpm for only 20 s.

All of these approaches appeared to give a more uniform initial layer; however, each of these films cracked upon crystallization. Hence, from these investigations it has been concluded that the 250°C drying step is a critical parameter within a very narrow process window. Above this critical temperature substrate oxidation will occur while below this temperature the gel fails to sufficiently consolidate and cracking results. The small variations in drying across the hotplate surface may be sufficient to cause instability during this critical step and lead to the observed reliability issues. In Section 4.5.2, an AFM investigation of film microstructure will reveal residual micro-cracking in films dried at 250°C. Currently, this lack of reliability due to this micro-cracking remains a key technological challenge.

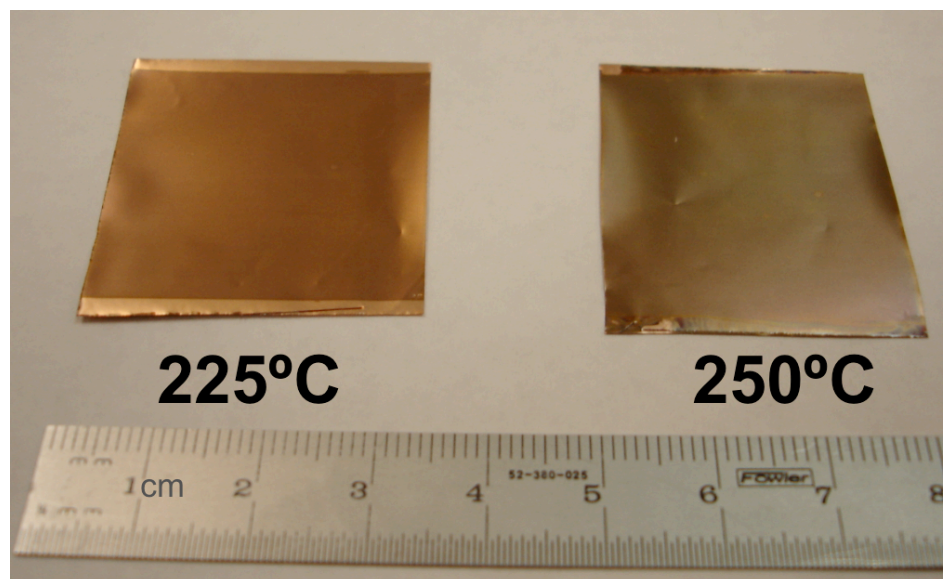


FIG 4-18 – Photograph Comparing Gel/Cu Appearance After Initial Drying Step: Photograph showing a 1-layer IMO derived gel dried for 5 min on a copper foil at two different temperatures: 225°C and 250°C.

These observations have a secondary implication; they provide strong evidence to support the hypothesis that gel consolidation is primarily determined by the end of the drying step. Both lowering the drying temperature by 10°C and reducing the spinning time by 10 s led to cracking despite still thermolyzing at 400°C. Even direct thermolysis at 400°C led to cracks. Thus, the instantaneous heating provided by a hotplate appears to be necessary for proper gel consolidation to occur.

4.5 Incorporation of Acac into IMO Solutions:

As mentioned previously, the addition of acac to the IMO solution is believed to temporarily separate oligomerized precursors. By decreasing the steric volume of these precursors, layer thickness is reduced, thereby reversing the effects of solution aging [116]. Because cracking events have been observed for PZT films prepared via the 2 + 3 method on copper foils past solution ages of 6 days, the addition of acac to these aged solutions was investigated as a means to extend useful solution lifetime.

4.5.1 Samples Prepared for Acac Investigation:

Two PZT films prepared on copper foil substrates are compared in this investigation. The first film was prepared from a 1-day old IMO solution. The second film was prepared from the same solution after it had aged for 30 days. Prior to deposition, acac (3 mol acac : 1 mol PZT) was reacted with the 30-day old solution for 2 minutes. An XRD analysis of the two films is presented in Fig. 4-19. The film prepared from the acac modified solution appears to have a detectable amount of Cu_2O ; however, as subsequent sections demonstrate the possible presence of this oxide has not strongly impacted this film's electrical performance. Most importantly, though, the acac-modified films did not crack during crystallization, verifying this ligand's "regenerative" ability.

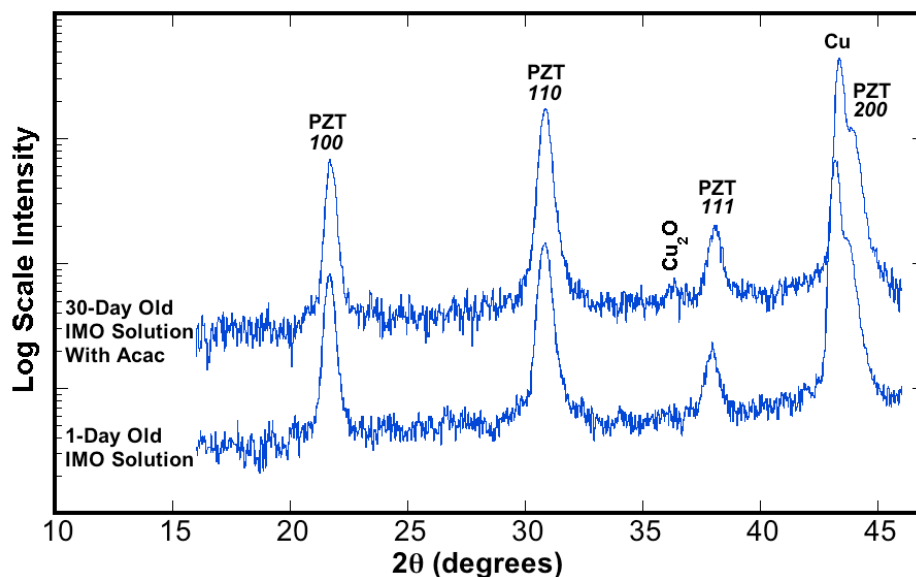


FIG 4-19 – XRD Comparison of PZT Films Prepared from a Fresh IMO Solution and a 30-Day Old Acac-Chelated Solution: *Two XRD scans showing PZT films prepared on Cu foils using the 2 + 3 method; the bottom pattern is from a film prepared with a 1-day old IMO solution while the top scan is from a 30-day old solution that was modified with acac.*

4.5.2 Microstructural Comparison:

An SEM image is shown in Fig. 4-20 indicating the columnar structure of these PZT thin films. Columnar grains are typically observed in PZT thin films since nucleation is most favorable at the electrode surface. From this image the film thickness is determined to be $\sim 0.7 \mu\text{m}$. Films on platinized silicon are $\sim 450 \text{ nm}$ thick at 5 layers [120].

Fig. 4-21 shows AFM images of PZT film surfaces prepared using (a) a fresh solution and (b) a 30-day old, acac-modified solution. The film prepared from the fresh solution has columnar grain diameters of 40 nm and surface nucleated grains are not detected. This is somewhat smaller than the grain size of 100-200 nm reported by Schwartz *et al.* for similarly prepared PZT films on platinized silicon [98, 120]. The aged, acac-modified solution appears to have a bi-modal grain size distribution. The smaller grains (40-60 nm) are similar to those observed in the unaged solution; the larger grains are 80-100 nm in diameter. These larger grains may be surface nucleated.

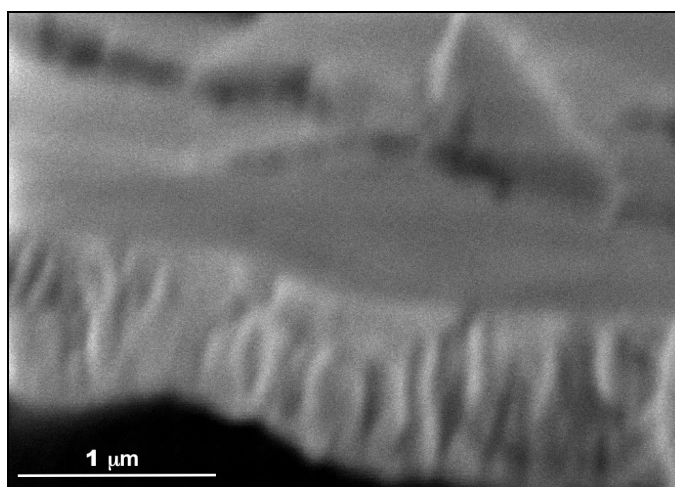


FIG 4-20 – SEM Image of IMO Derived PZT Film: *SEM micrograph showing a section of the cross-section of a PZT film that was forcibly removed from the copper surface.*

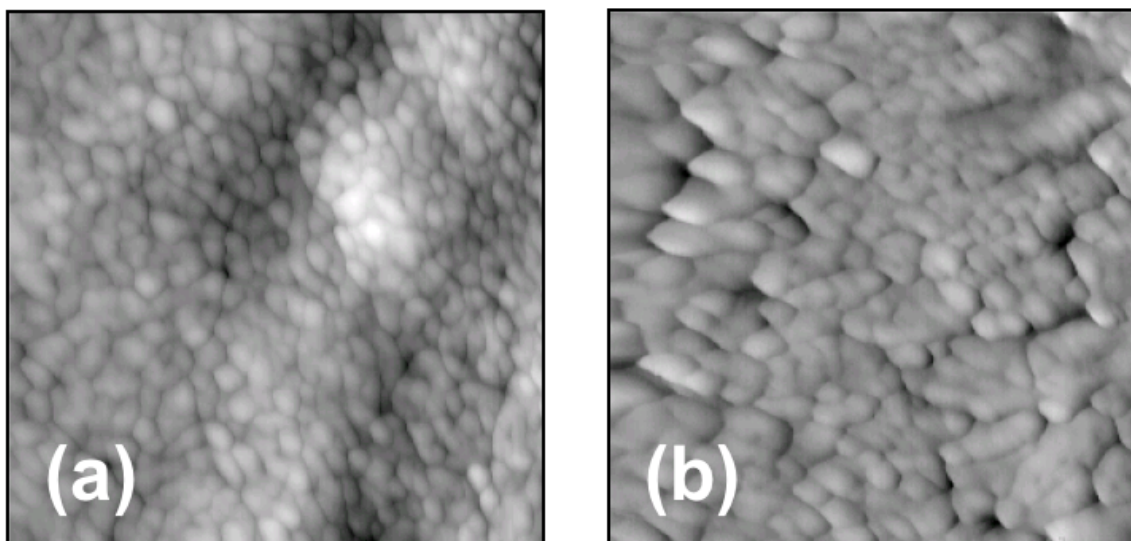


FIG 4-21 – AFM Images of IMO and Acac-Modified PZT Films: *AFM micrographs of PZT film surface (1 μm x 1 μm) illustrating the difference between (a) a 1-day old IMO solution and (b) a 30-day old, acac-modified solution. Both samples were annealed at 650°C in nitrogen.*

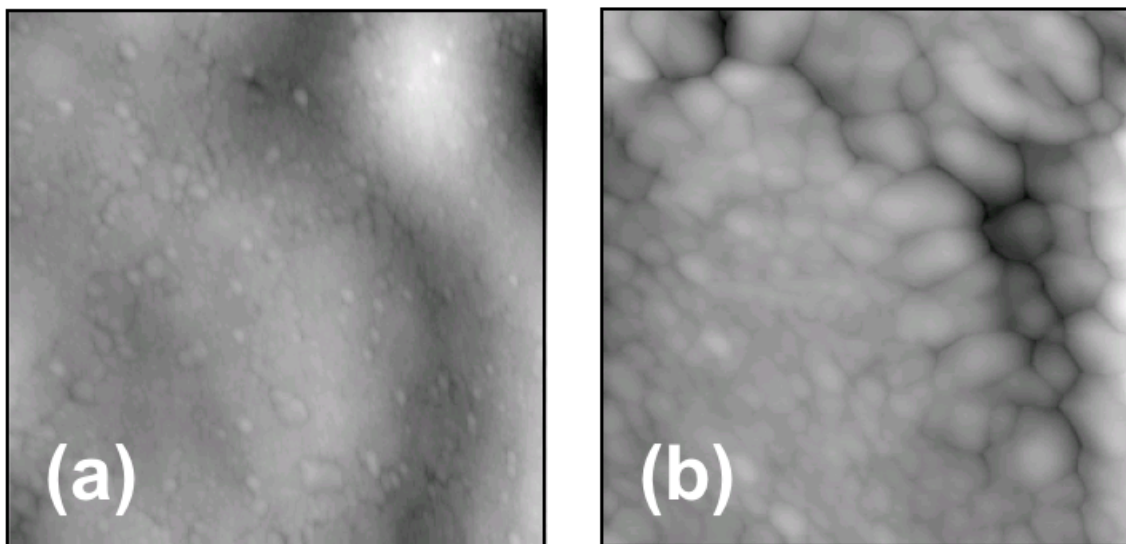


FIG 4-22 – AFM Images Acac-Modified PZT Film Crystallized at 700°C: *AFM micrographs of PZT film surface for a 30-day old IMO solution modified with acac that was crystallized at 700°C. (a) scan size of 3 μm x 3 μm ; (b) scan size of 1 μm x 1 μm .*

Fig. 4-22 shows AFM images of PZT films processed from aged, acac-modified solutions that were crystallized at 700°C. Image (a) definitively illustrates the occurrence of surface nucleated grains. The higher resolution image (b) again indicates a bimodal grain size distribution with small columnar grains of 40-60 nm diameter and larger surface nucleated grains of 80-120 nm diameter.

These results suggest that the addition of acac is not as effective in eliminating surface nucleation events in films prepared on copper from aged solutions as was reported for PZT films deposited on platinized silicon [116, 120]. Two possible explanations are offered. First, the films prepared on copper appear to be intrinsically thicker than those on platinized silicon probably due to the substrate's roughness. For this solution chemistry, xerogel thickness primarily determines the frequency of surface nucleation [120]. A second explanation may be the difference in thermolysis conditions. This difference may increase the free energy of the xerogel structure, thereby increasing the driving force for surface nucleation.

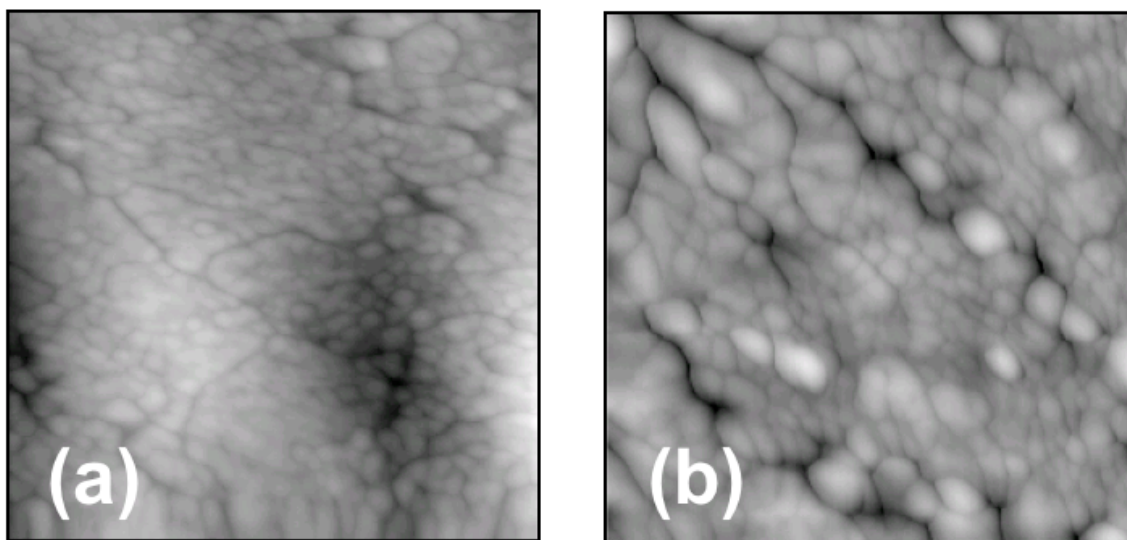


FIG 4-23 – AFM Images Illustrating Micro-cracking in PZT Films: *A F M* micrographs ($1\ \mu\text{m} \times 1\ \mu\text{m}$) of PZT films deposited on copper foils using the 2 + 3 method: (a) from a fresh IMO solution crystallized at 650°C and (b) from a 30-day old solution modified with acac and fired at 700°C .

AFM analysis also reveals that PZT films synthesized using the 2 + 3 composite gel architecture still contain residual micro-cracking problems. An illustration of such cracking is given in Fig. 4-23. These cracks are probably the primary source for the film's poor electrical reliability.

4.5.3 Dielectric Comparison:

A comparison of the PZT films' dielectric tunability is given in Figs. 4-24 and 4-25. These figures indicate that the film deposited from a fresh IMO solution has a tunability of 64% compared to only 60% for the acac-modified film. In contrast, the dielectric loss is lower for the acac-modified film. However, both films exhibit excellent high-field saturation and have similar intrinsic permittivities. These features suggest comparable film quality with perhaps less extrinsic contributions in the acac-modified films. This difference in response may reflect the difference in film microstructure.

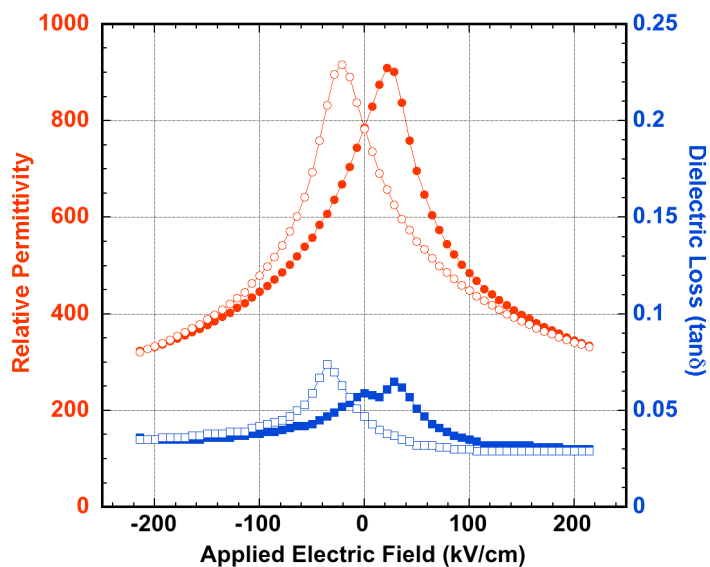


FIG 4-24 – Dielectric Tunability of PZT Film on Cu from 1-Day Old IMO Solution: Plot of ϵ' and $\tan\delta$ vs. applied electric field obtained at 10kHz and room temperature for a PZT film deposited with a 1-day old IMO solution.

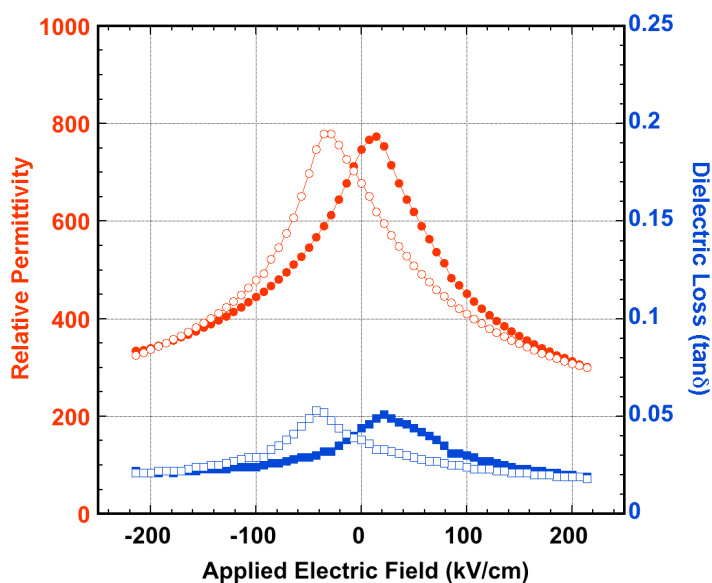


FIG 4-25 – Dielectric Tunability of PZT Film on Cu from Aged IMO Solution with Acac Chelation: Plot of ϵ' and $\tan\delta$ vs. applied electric field obtained at 10kHz and room temperature for a PZT film deposited from a 30-day old IMO solution that has been modified with acac.

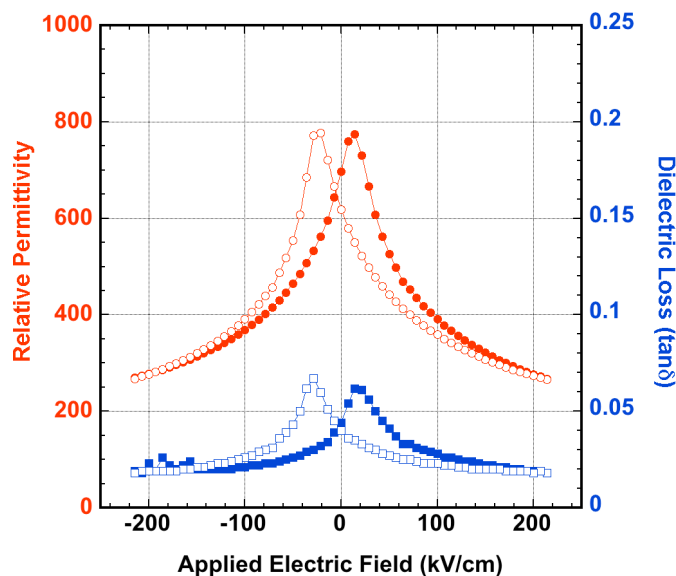


FIG 4-26 – Dielectric Tunability of PZT Films on Cu Crystallized at 700°C: Plot of ϵ' and $\tan\delta$ vs. applied electric field obtained at 10kHz and room temperature for a PZT film deposited from a 30-day old IMO solution that has been modified with acac and then crystallized at 700°C in nitrogen.

Finally, the dielectric response for the acac-modified film crystallized at a higher temperature of 700°C is presented in Fig. 4-26. The tunability of this film is 66% with intrinsic losses of below 2% and improved high-field saturation.

4.5.4 Ferroelectric Comparison:

A comparison of the ferroelectric response for PZT films derived from the fresh IMO solution to those prepared with the 30-day old acac-chelated solution is shown in Fig. 4-27. These P-E loops have comparable remanent polarizations ($\sim 33 \mu\text{C}/\text{cm}^2$) and coercive fields ($\sim 40 \text{ kV}/\text{cm}$). Both films exhibit impressive polarization saturation.

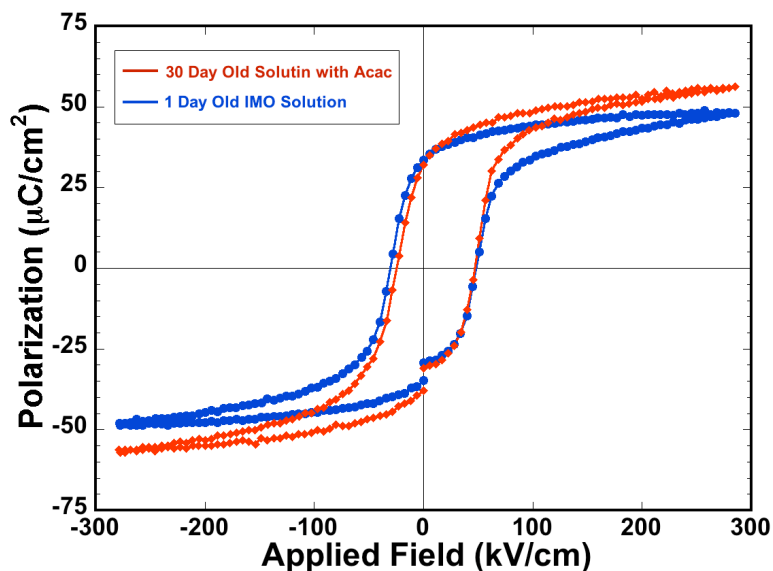


FIG 4-27 – Comparison of Ferroelectric Response from PZT Films Prepared with IMO and Acac Modified Solution Chemistries: *P-E loops collected from PZT films deposited on copper foils prepared using a fresh IMO solution and an aged IMO solution with acac chelation.*

4.5.5 Investigation of Leakage Current in Acac-Modified PZT Films on Copper

A leakage current measurement taken from the PZT film prepared on copper using the aged IMO solution with acac chelation is displayed in Fig. 4-28. Schwartz *et al.* have reported leakage values of $\sim 10^{-6}$ A/cm² (5% excess Pb) and $\sim 10^{-8}$ A/cm² (20% excess Pb) at 62 kV/cm for PZT films synthesized with IMO solutions on platinized silicon [121]. At this field, the leakage current for this PZT film on copper is approximately 5×10^{-6} A/cm². Although this leakage is one to two orders of magnitude larger than Schwartz *et al.*'s values, it should be noted that these reference films were annealed in ambient air. Thus, they probably contain less oxygen vacancies, which act as electron donors and increase PZT conductivity. Additionally, these copper foils have significantly more surface roughness than typical platinized silicon substrates; these surface asperities could locally reduce film thickness and increase leakage currents.

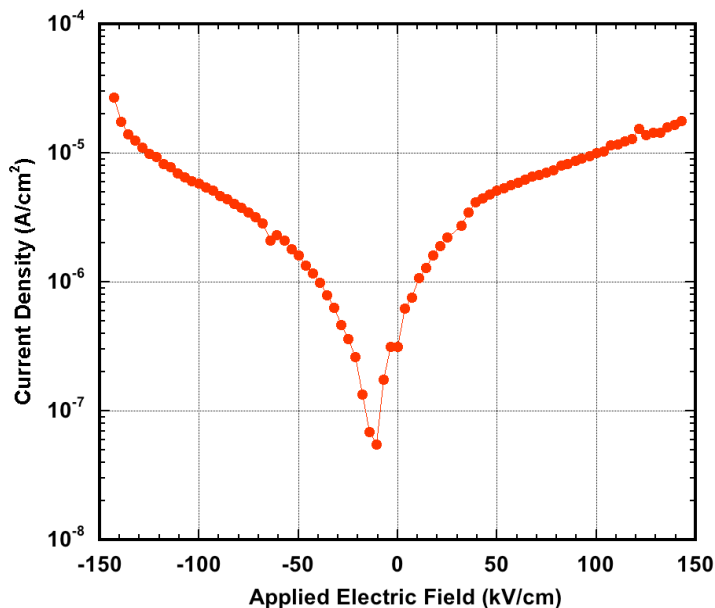


FIG 4-28 – Leakage Current Measurement of PZT Film on Copper Foil: Measurement of leakage current as a function of applied DC voltage for a PZT film prepared directly on a copper foil using the 30-day old IMO solution with acac chelation.

4.5.6 Investigation of Ferroelectric Fatigue in Acac-Modified PZT Films on Copper:

A sample of the acac-modified PZT film prepared on a copper foil was electrically fatigued; the results of this experiment are presented in Figs. 4-29 and 4-30. The fatigue plot (Fig. 4-29) and the tilting of the P-E loop (Fig. 4-30) resemble classic behavior for electrically fatigued PZT films on silicon with metallic bottom electrodes. The P_r drops by about 33% over 9 decades ($30.5 \text{ } \mu\text{C}/\text{cm}^2$ to $20.5 \text{ } \mu\text{C}/\text{cm}^2$) while the coercive field increases by 26% ($48.6 \text{ kV}/\text{cm}$ to $61.4 \text{ kV}/\text{cm}$). This increase in E_c along with the decrease in polarization loop saturation may indicate physical damage to the film and increased leakage currents. However, by annealing the sample above the Curie point (450°C for 7 min in $p\text{O}_2 = 1.3 \times 10^{-14} \text{ Torr}$), about 87% of the P_r was recovered ($29.2 \text{ } \mu\text{C}/\text{cm}^2$) as shown in Fig. 4-31. This ability to recover 87% of the virgin polarization response provides confidence that the observed cycling behavior is primarily a result of true ferroelectric fatigue and not simply AC degradation. Warren *et al.* reported a similar polarization

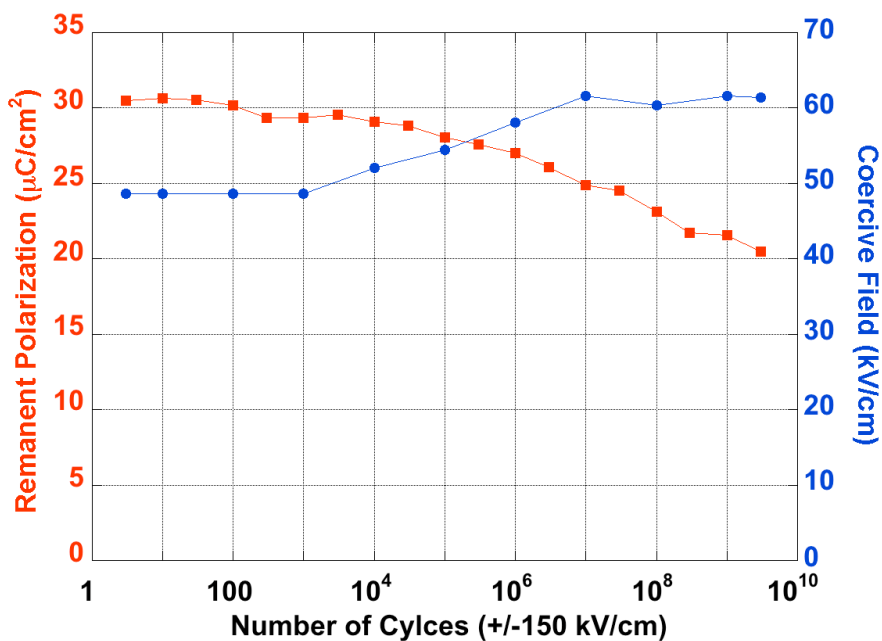


FIG 4-29 – Ferroelectric Fatigue Characteristics of PZT Film Prepared on Copper: Plot of P_r and E_c as a function of electrical cycling.

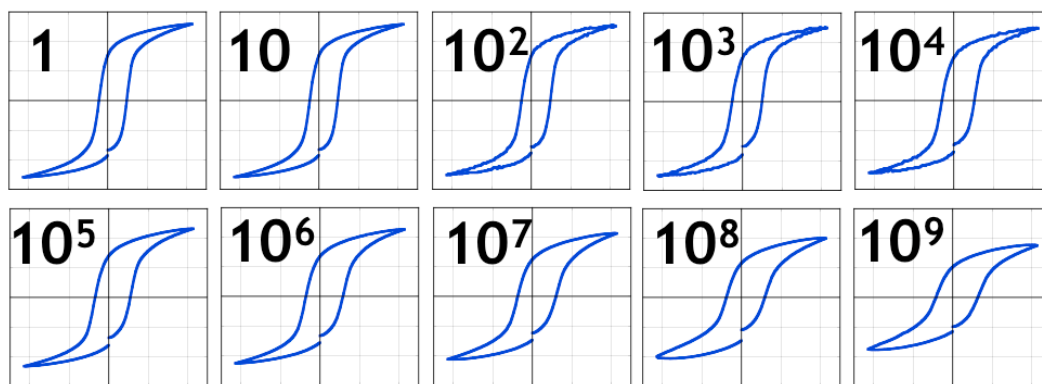


FIG 4-30 – P-E Response of PZT Film on Copper as Fatiguing Occurs: Plots of P - E loops during each decade of fatigue (number indicates the number of cycles). Axes have values of ± 20 V and ± 50 $\mu\text{C}/\text{cm}^2$.

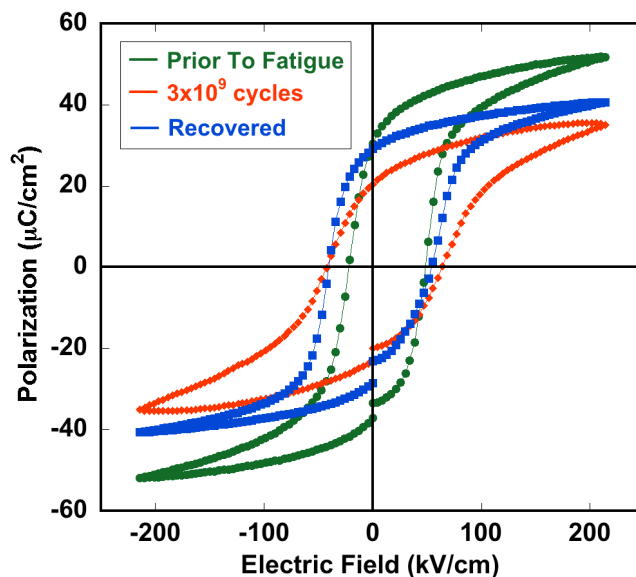


FIG 4-31 – Comparison of Fatigued and Recovered Ferroelectric Responses for a PZT Film on Copper: *P-E loops showing the difference in ferroelectric response of virgin PZT film, fatigued PZT film, and PZT film after a recovery anneal.*

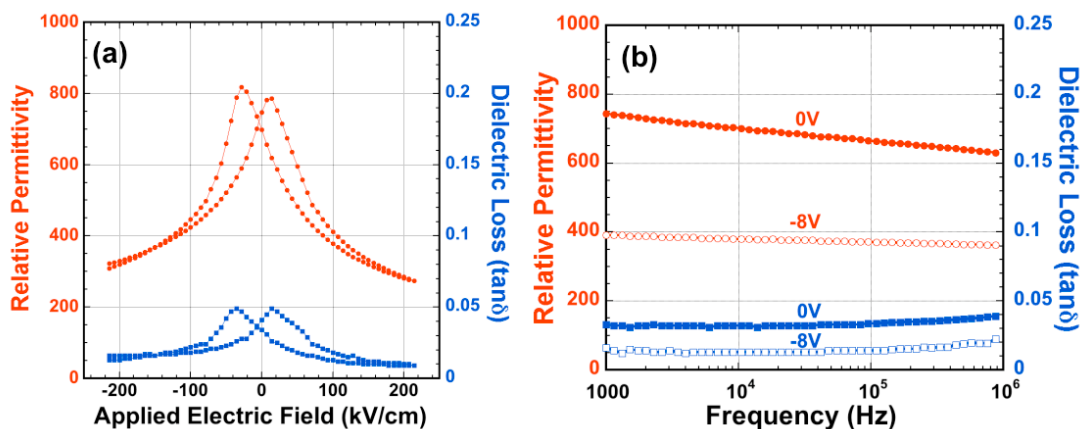


FIG 4-32 – Dielectric Response of PZT Film After Fatiguing and Recovery Anneal: *Dielectric measurements showing (a) the dielectric tunability and (b) the dielectric dispersion of a PZT film after fatiguing and undergoing a recovery anneal.*

recovery (~86%) using optical stimulation on IMO derived PZT films deposited on platinized silicon that had also been fatigued for 10^9 cycles [42]. To further verify the quality of this recovered sample, dielectric tunability and dispersion data was also collected post recovery anneal. This data is plotted in Fig. 4-32 and further substantiates the PZT electrical integrity.

4.6 Evaluation of Crystallographic Orientation, Film Stresses, and Domain Structure in PZT Films:

As discussed in Chapter 1, the ferroelectric and dielectric properties of PZT films can be affected by crystalline anisotropy as well as stress-induced domain orientation. This section will briefly discuss these topics as they relate to the PZT films prepared on copper foils via the 2 + 3 layer method. This discussion can perhaps provide insight into why these PZT films fail to have a dielectric constant greater than 1000, but exhibit remanent polarizations exceeding $30 \text{ } \mu\text{C}/\text{cm}^2$.

4.6.1 Texturing of PZT Films Deposited on Copper Foils:

XRD evidence suggests the existence of a 100 texturing in many of the PZT films deposited on copper substrates. For many of the 2 + 3 processed films, the 100 reflection exhibits a relative intensity much greater than predicted by the powder pattern. For instance, in Fig. 4-19 the 100 reflection is ~57% the intensity of the 110 reflection. This is more than twice the expected intensity of ~20% for a randomly oriented structure (see appendix). In contrast, the 111 reflection is about 16% as intense as the 100 ; this value is comparable to the 15% relative intensity expected for random orientations. Furthermore, patterns from the GADDS XRD detector reveal a surface normal orientation in \square for the 100 reflection (see Fig. 4-33).

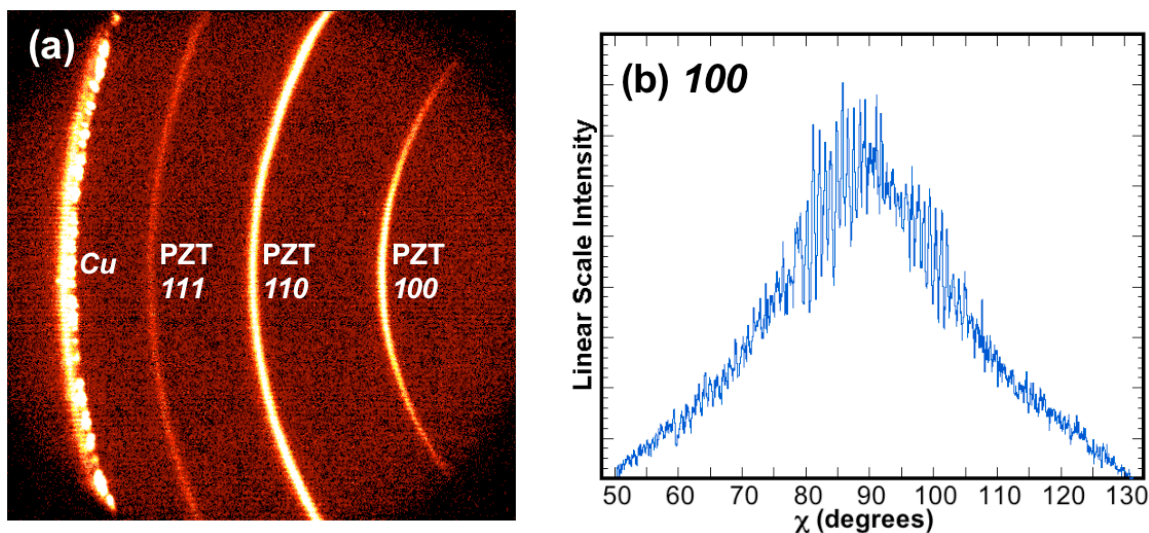


FIG 4-33 – XRD Evidence for the Texturing of PZT Films on Copper Foils: *XRD data showing the (a) GADDS area detector scan of a PZT film deposited on copper and (b) a plot of intensity vs. χ for the 100 reflection.*

This orientation relationship may be indicative of the PZT film's nucleation/growth behavior. To achieve its columnar microstructure, the perovskite film nucleates at the copper surface. Unlike platinumized silicon substrates, which often contain textured Pt electrodes that can provide a template for *111* nucleation, the copper substrates have randomly oriented grains. Thus, although the reducing thermolysis conditions may have decreased pyrochlore stability, a *111* texture is not induced as was observed by Reaney *et al.* [32]. Alternatively, the observed *100* texturing likely results from the perovskite growth habit [30, 32]; *100* oriented nuclei can dominate during growth since the 00ℓ face has the lowest bond density / surface energy.

4.6.2 Existence of Stress in PZT Films Deposited on Copper Foils:

Depositing thin films on thin metal foils provides a unique opportunity for qualitatively evaluating the amount / direction of film stress, since foils are often observed to curl in response to stresses in the film. This type of evaluation mechanism is much more challenging to assess in rigid substrate systems.

During thermolysis foils are commonly observed to curl up, indicating tensile stresses in the film as a result of volume shrinkage and gel stiffening. In contrast, foils often appear to straighten during the three drying layers, possibly indicating some form of stress relief. Directly after annealing the film, the foil again shows substantial upwards curling due to the volume shrinkage that has transpired during crystallization. However, as the sample cools, the foil can be observed to “uncurl” itself. This uncurling indicates larger substrate contraction relative to the film, which is consistent with the thermal expansion coefficient mismatch of the PZT/Cu system ($CTE_{Cu} = 17 \text{ ppm}/^{\circ}\text{C}$ [21], $CTE_{PZT} = 6.7 \text{ ppm}/^{\circ}\text{C}$ (paraelectric) ; $2 \text{ ppm}/^{\circ}\text{C}$ (ferroelectric) [27]). This mismatch places the PZT film in compression, which favors *c domains*.

4.6.3 Domain Structure in PZT Films Deposited on Copper Foils:

PZT films deposited on copper foils were analyzed with piezo-response force microscopy (PFM) to investigate the domain structure. These PFM results are presented in Fig. 4-34. The topography of this acac-modified, 700°C fired PZT film is shown in images (a) and (b). Images (c) and (d) show the piezo-response maps for an unpoled film sampled with a field $< E_c$. The phase image, which represents the polarization orientation, appears to indicate a random distribution of *a* and *c domains*. If the gray regions are *a domains*, then this data appears to contradict the stress induced domain structure predicted in the previous section and suggests no preferred domain alignment in the unpoled state. However, these gray regions may also represent grains with *c domains* that contain a 180° domain wall. Currently, a conclusive interpretation is not possible. The amplitude signal indicates that downward oriented *c domains* (bright regions in the phase map) are more piezo-active than upward oriented *c domains*.

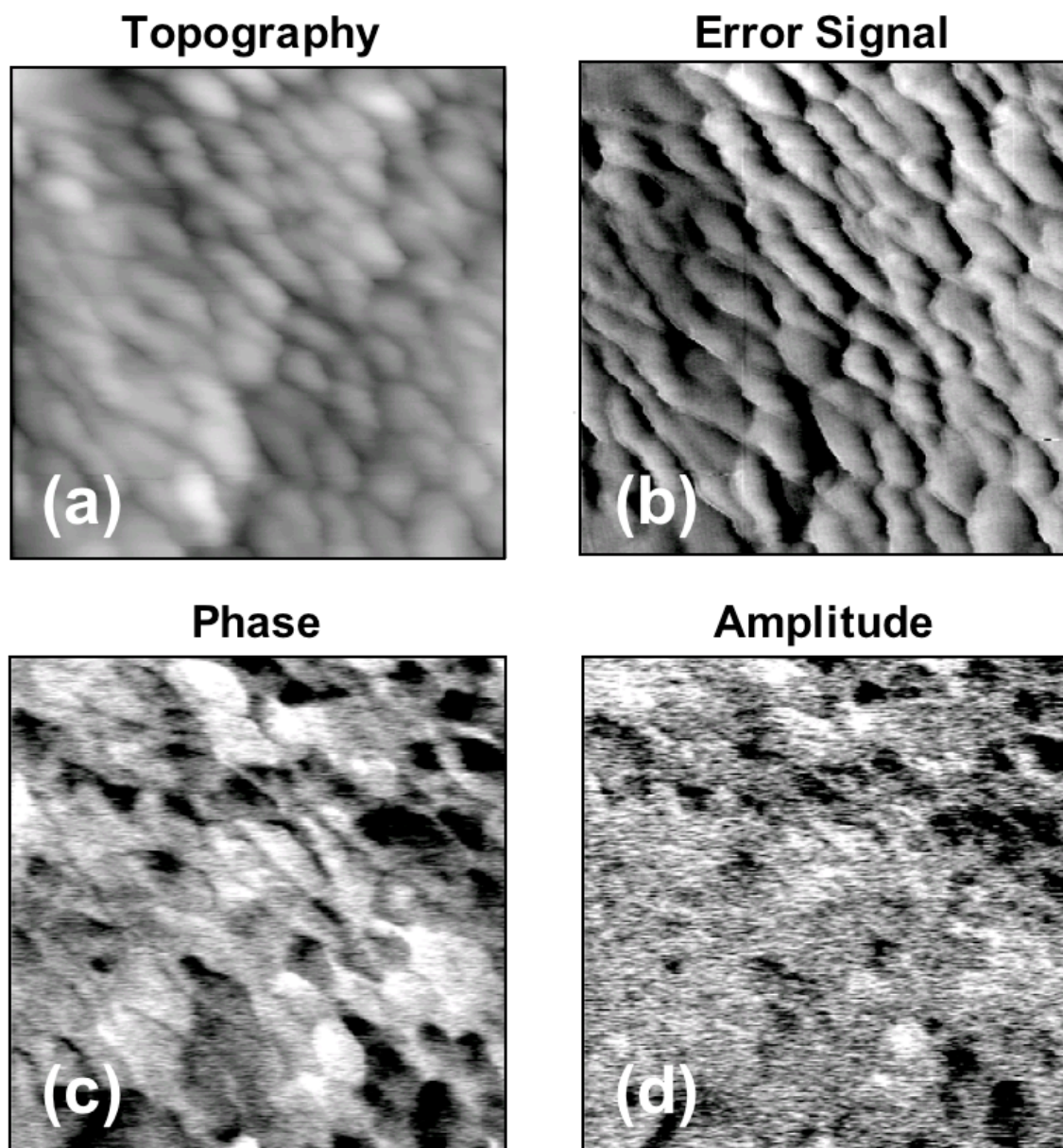


FIG 4-34 – AFM and PFM Images Illustrating the Domain Structure in PZT Films Prepared on Copper Foils: *Scanning probe microscopy images ($1 \mu\text{m} \times 1 \mu\text{m}$) of a PZT film prepared from a 30-day old, acac-modified solution deposited on a copper foil and crystallized at 700°C in nitrogen: (a) topography map; (b) topography error signal; (c) domain phase map; (d) domain amplitude. Bright and dark regions in the phase map indicate top-to-bottom and bottom-to-top *c* domain polarization orientations respectively; gray regions are probably *a* domains.*

4.7 Hypotheses for the Success of the 2 + 3 Layer Process:

Although the success of the 2 + 3 layer process in resolving film cracking issues has been established in this thesis, a complete understanding of how this process avoids copper oxidation has not been well addressed. An understanding of this process could be beneficial in applying this technology to other base metal substrates. Hence, this section examines the current understanding of this problem.

4.7.1 Re-evaluating Oxidation During Crystallization:

It is instructive to re-analyze data originally presented in Sections 4.3.1 and 4.3.2 for PZT gels processed from an IMO solution and simply dried on a hotplate prior to crystallization. According to the data originally presented in Figs. 4-2, 4-3, and 4-4, films crystallized in N₂ and 1.3x10⁻¹⁴ Torr pO₂ show increasing copper oxidation during the crystallization step as a function of drying temperature. This behavior is demonstrated in Fig. 4-35. An explanation for why drying temperature dramatically impacts the substrate oxidation process during crystallization is not intuitively obvious. From the optical microscopy investigation, it was revealed that drying temperature determines gel consolidation; films dried at higher temperatures are denser and less prone to cracking. Thus, it is hypothesized that the gel density also influences the oxidation process during crystallization.

Two explanations are proposed. First, as gel density increases, it is expected that the xerogel structure will more effectively trap oxidizing species (such as unpyrolyzed organics, water molecules, or adsorbed oxygen) near the interface. Films dried at higher temperature will therefore be more likely to oxidize the copper during crystallization; this explanation supports the “organic oxidation source” hypothesis. A second explanation may be that the denser and more networked structure of films dried at higher temperatures inhibits precipitation of a second phase—Pb/PbO—to act as an oxidation barrier. However, at lower drying temperatures, such a phase has not been detected. Thus, this explanation appears less likely.

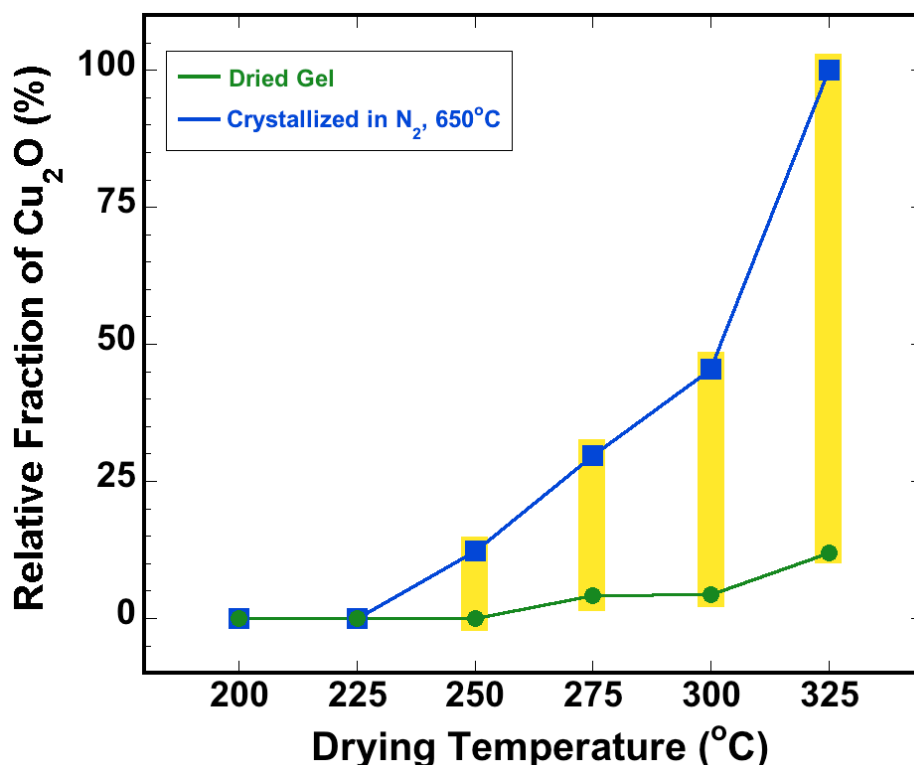


FIG 4-35 – Evaluation of Copper Oxidation During Crystallization of Dried Films: Plot of normalized Cu_2O XRD peak intensity for films prepared from an IMO solution and simply dried prior to crystallization. The yellow bars represent the amount of substrate oxidation that occurs upon the crystallization step.

4.7.2 Investigation of the 2 + 3 Process's Success in Avoiding Copper Oxidation:

In an attempt to better understand why the 2 + 3 layer approach is successful, the phase evolution of this approach was monitored by XRD. The results of this experiment for both a standard 2 + 3 processed film and a second film where a 300°C dry was employed during the first two layers, is reported in Figs. 4-36 and 4-37. Fig. 4-37 demonstrates that substrate oxidation is encouraged by the initial 300°C dry. Subsequent

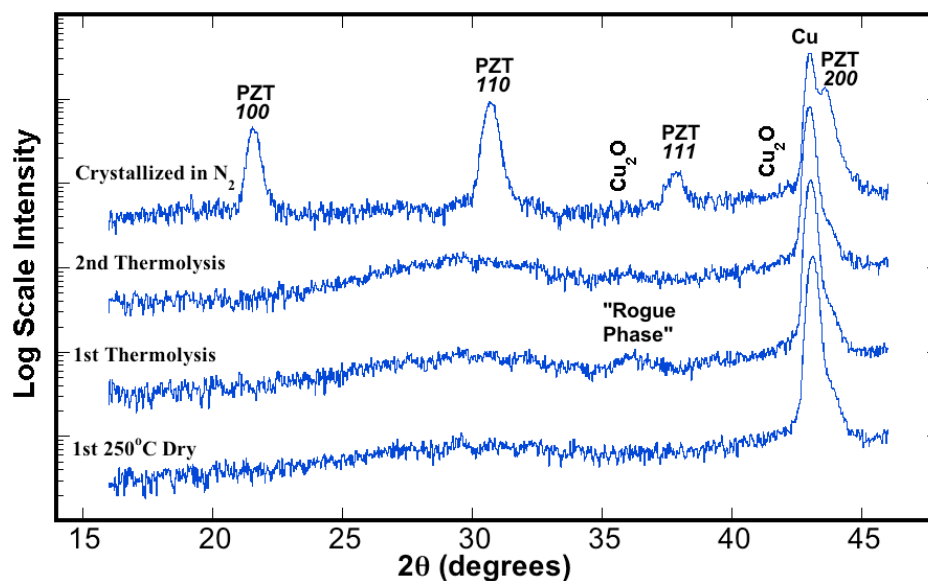


FIG 4-36 – Phase Evolution in 2 + 3 Layer Process Using a 250°C Dry: *XRD scans showing the phase evolution in a 2 + 3 layer processed film using standard conditions.*

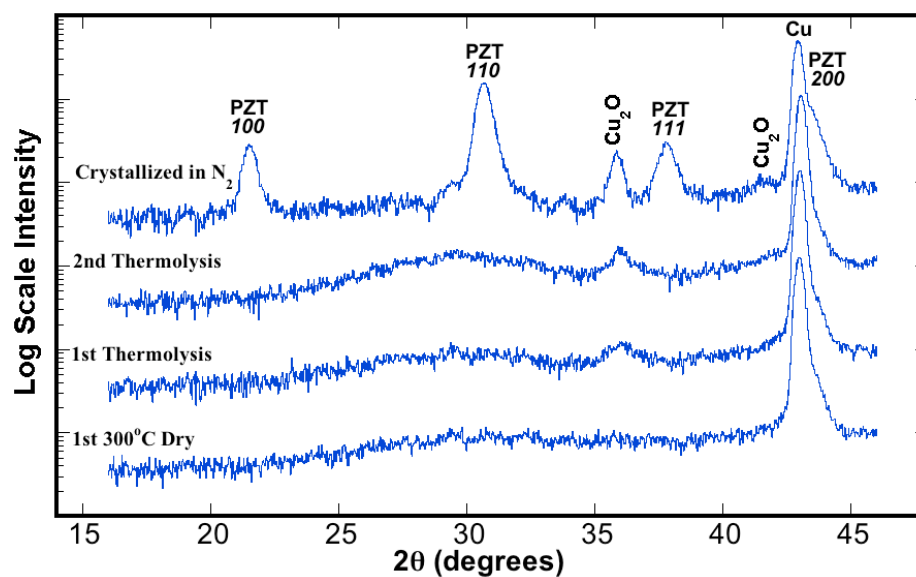


FIG 4-37 – Phase Evolution in 2 + 3 Layer Process Using a 300°C Dry: *XRD scans showing the phase evolution in a 2 + 3 layer processed film using a 300°C dry on the first two layers.*

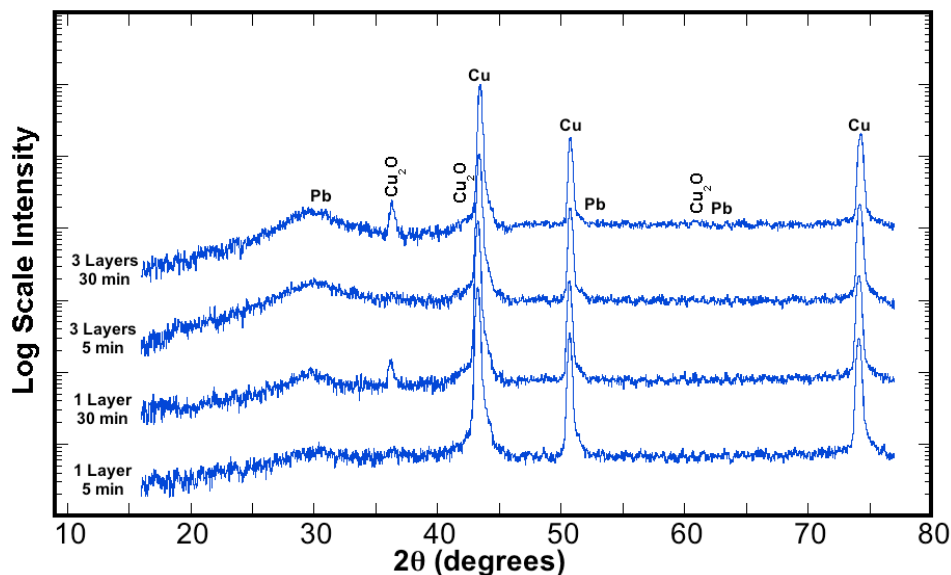


FIG 4-38 – Attempts to Form Intermediate During Thermolysis of IMO Films: *XRD scans showing IMO gels that were thermolyzed for either 5 min or 30 min in an attempt to better form the intermediate phase.*

processing steps only serve to perpetuate this oxidation. Alternatively, the specimen initially dried at 250°C (Fig. 4-36) develops a similar rogue phase during the first thermolysis, but it subsequently disappears upon further processing. This data suggests that a transient intermediate phase may play a role in the success of the 2 + 3 process. Such an intermediate could act as an internal oxidation barrier and sustain the integrity of the gel/Cu interface prior to crystallization.

One possible explanation may be Pb precipitation, similar to the EC solution chemistry. However, failure to detect the *111* Pb reflection at ~31° contradicts this hypothesis. Furthermore, Pb precipitation has only been observed to occur in the IMO system for the extreme circumstances of crystallizing in pure forming gas (Fig. 4-5). The well-networked gel expected for IMO films likely impedes the process of Pb precipitation.

In an attempt to further clarify this situation, samples were prepared to enhance this transient phase's crystallinity / quantity. Two samples were prepared: (1) a 1 layer IMO deposited film dried at 250°C and (2) a 3 layer IMO deposited film dried at 250°C. These samples were then thermolyzed in flowing forming gas at 400°C for 5 min and 30 min. A

longer and a shorter time were investigated to either enhance the crystallinity/reaction or reduce the phase's volatilization respectively. The XRD results are presented in Fig. 4-38. The reflection at 36°C appears to be enhanced with increasing film thickness and thermolysis time. However, other reflections have not definitively emerged. Thus, an exact identification remains ambiguous.

4.7.3 Discussion of Hypotheses for Cu₂O Reduction in 2 + 3 Layer Processed Films:

Originally, the hypothesis of organic decomposition reactions / products being a source of substrate oxidation was conjectured [122]. This hypothesis is somewhat supported by the observed oxidation of dried films in low pO₂ conditions (Figs. 4-3, 4-4).

An alternative explanation is that the substrate oxidation is simply undetectable prior to annealing due to poor crystallinity of the Cu₂O phase. Thus, the success of implementing the thermolysis step may not lie in the removal of organic species but rather some reaction that occurs in the gel during thermolysis. One possibility is that continued condensation reactions make the M-O-M network more impermeable to oxygen diffusion, allowing the gel to act as an internal barrier to substrate oxidation during subsequent processing. Another possible explanation is the formation of a protective transient phase during thermolysis as was indicated in the previous section. Lead is an interesting possibility because it has complete solid insolubility with copper and could act as a protective sheath (see phase diagram in the Appendix). This appears to be the mechanism active when films are synthesized with EC solutions. Unfortunately, the current work for the IMO solution chemistry has uncovered minimal evidence to suggest a similar Pb precipitation mechanism in IMO derived films. Thus, currently, a complete understanding of why the 2 + 3 layer process is successful at minimizing substrate oxidation does not exist.

5. Conclusions and Future Work

As indicated in Chapter 1, this thesis has focused on relationships between the processing and structure of a materials system. By developing an understanding of this relationship, a new processing approach has been devised for the fabrication of CSD PZT thin films directly on copper surfaces. This final chapter reviews the key innovations used to develop this process and highlights the most technologically significant results. The chapter concludes with some suggestions for future investigations.

5.1 Conclusions:

Compatibility between Pb-containing complex oxides (like PZT) and base metals is challenging because conventional gas phase / condensed phase equilibrium processing is complicated by a narrow process window and the susceptibility of Pb to volatilization. As a result, this thesis has developed a new methodology for depositing sol-gel PZT films on base metal substrates. In this scheme, an understanding of CSD processing science was utilized to design procedures for synthesizing high-quality PZT thin films in intimate contact with base metals without unwanted interfacial reactions. Using this new approach, 52/48 PZT films prepared directly on copper foil substrates have demonstrated dielectric and ferroelectric properties comparable to similar films deposited on semiconductor-grade, single-crystal substrates with noble metal or conductive oxide electrodes. This advancement is important because economically it lowers the barrier to ferroelectric thin film mass production. Furthermore, it provides new technological opportunities including flexible electronic devices, low-resistivity interconnects, and homogeneous integration with strong ferromagnets.

5.1.1 Investigations of Organic Removal:

Removal of the gel's organic constituents, particularly the chelating ligands, has been identified as a critical parameter in achieving PZT/Cu compatibility. Difficulty arises in achieving extraction conditions that are mutually consistent with avoiding copper oxidation and widespread film cracking. These constraints proved extremely difficult to

overcome in alkanolamine chelated solutions. Strong chelation strength and low volatility made proper removal of alkanolamine ligands challenging—often leading to film cracking or poor crystallization of the perovskite phase. By applying a water vapor thermolysis step, which enhances ligand hydrolysis, improvements were made; however, cracking could never be totally eliminated without sacrificing interfacial quality. Metallic Pb precipitation was also observed for this solution chemistry and is believed to be a critical factor in successfully minimizing substrate reactions in this system.

By switching the solution chemistry to a lower-volatility, less strongly bound chelating ligand (acetic acid), immediate reductions in the extent of film cracking were observed. Water vapor atmospheres were no longer needed to facilitate organic removal. To resolve remaining cracking issues, a composite gel architecture was developed in which initial CSD layers were processed in conditions consistent with maintaining interface integrity. Subsequent layers were deposited using conditions that improved gel consolidation and avoided crack formation. Although these latter layers were processed under more aggressive conditions, the primary layers acted as an internal buffer to protect the underlying copper surface. Using this composite gel architecture in conjunction with an acetic acid chelated solution chemistry, crack-free PZT films were prepared on copper surfaces with quantities of interfacial reaction products below the detection limits of XRD.

5.1.2 Technological Importance of PZT Thin Films on Copper:

This thesis has demonstrated PZT thin films on copper surfaces with dielectric and ferroelectric properties that surpass all previously published data for PZT on base metal substrates. The values reported in this thesis are comparable to PZT films of similar solution chemistry deposited on conventional platinized silicon substrates. Dielectric constants of 700-800 with $\tan \delta$ values between 0.02 and 0.05 have been reported over a frequency range of 1 kHz to 1 MHz. Voltage dependent dielectric measurements exhibited definitive hysteretic responses with dielectric tunabilities in excess of 60% and well-saturated high-field behavior. Leakage current measurements revealed reasonable DC

conductivity ($\sim 10^{-5}$ A/cm² at 8V), especially for an undoped ferroelectric processed in a reducing environment.

These PZT films also exhibited classical ferroelectric responses. P-E loops displayed remanent polarizations of 33 $\mu\text{C}/\text{cm}^2$ and coercive fields of ~ 40 kV/cm. When electrically cycled, these films demonstrated typical fatigue behavior—lower remanent polarizations and a loss in P-E loop squareness. However, these properties could be recovered by annealing above the Curie point, further verifying the high quality of these PZT films. Thus, these films are believed to be a true breakthrough in the fabrication of ferroelectric PZT thin films on base metal surfaces; unlike previous processes, the films described in this thesis have properties that are competitive with PZT thin films processed on standard noble metal or conductive oxide electrodes.

5.2 Possibilities for Future Investigations:

A critical requirement for the future development of this technology is in improving the reliability of the films. The primary focus must be on resolving the remaining cracking issues. The solution to this problem will probably come from a better understanding of the sol-gel system; particularly by making changes to the solution chemistry that will improve gel consolidation. Because this solution has been optimized for PZT quality and not to meet the needs of a base metal substrate, it is expected that the solution chemistry can still be improved. Modifying oligomer structure by varying reaction times, water content, and solution pH may impact gel consolidation and improve residual micro-cracking problems. A complete study of solution aging effects is also necessary to define the exact lifetime of IMO solutions for 2 + 3 layer processing as well as the specific impacts of acac additions with solution age.

Additionally, a more complete study of the PZT/Cu interface is necessary, including a TEM investigation. A better understanding of this interface and how the processing of the initial layer affects interfacial quality is believed to be essential in furthering the development of this technology. Of correlated interest is the possibility of Pb acting as an oxidation barrier for copper surfaces. If this hypothesis is correct, it may

be possible to engineer this mechanism into other solution chemistries and materials systems.

For device applications, it will be necessary to achieve lower leakage currents. Since DC leakage is believed to be primarily associated with electronic conduction mechanisms, three options are suggested: (1) employ a re-oxidizing anneal to eliminate oxygen vacancy donors, (2) dope the material to compensate for ionic defects, and (3) optimize the amount of excess lead to minimize defect concentrations associated with PbO volatility.

Finally, additional characterization of these PZT films is suggested, particularly in respect to their piezoelectric properties. Piezoelectric measurements are necessary to evaluate this system for many technological applications. In addition, the flexible foil substrate offers a unique opportunity for understanding the effects of strain on piezoelectric, ferroelectric, and dielectric properties.

6. Appendix

6.1 Procedures for Data Collection:

X-ray diffraction (XRD) data was collected on a Bruker AXS D-5000 x-ray diffractometer equipped with a GADDS area detector operated at 40 kV / 30 mA. Typical scans were collected for 15 min except for texturing data, which was collected for 2 hours to improve signal strength in the θ plot. The powder diffraction file cards used to identify relevant phases are included in this appendix (Fig. 6-1). Families of planes in the pseudo-cubic perovskite phase could not be resolved with the Bruker diffractometer, so PZT peaks have been labeled using a single reflection notation.

Optical microscopy was used to evaluate cracking of films. Scanning electron microscopy (SEM) was utilized to image cross-sectional microstructure. A Hitachi S-3200N thermal emission microscope was operated at 5 kV to capture these images. Samples were prepared for cross-sectional imaging by slicing samples with razor blades. Regions that were tore up from the surface were found to provide sufficient quality to assess the cross-sectional microstructure. Atomic force microscopy (AFM) was employed to evaluate film microstructure. A CP Research Thermomicroscope AFM was operated in contact mode to collect this data. This microscope was also utilized for the piezo-response force microscopy (PFM) data. PFM imaging was accomplished by contacting the back side of the copper foil to ground and sampling the film through the AFM tip with a driving AC voltage of 1.5 V (RMS) and 12 kHz.

Platinum top electrodes were sputter deposited through a shadow mask and used to make electrical measurements on MIM capacitor structures. The typical electrode size was 220 μm in diameter. Dielectric measurements (tunability and dispersion) were collected using an HP 4192A impedance analyzer. The sampling AC voltage was always kept at 0.05 V. Electrode area was measured by optical microscopy. Film thickness was determined by SEM and found to be ~ 700 nm for a 2 + 3 layer processed film. Leakage current measurements were taken on a Keithley 617 electrometer. These I-V sweeps were conducted between -10 V and $+10$ V in 0.25 V intervals with 10 s relaxation times.

Ferroelectric properties (P-E hysteresis loops and fatigue testing) were measured with an RT-66A ferroelectrics tester. Hysteresis loops were collected using a 100 kHz sampling voltage. To fatigue the samples, an HP33120A function generator was used to apply a 100 kHz square wave pulse with a +/-10 V amplitude.

6.2 Powder Diffraction Cards

Copper (#4-836)		
Reflection	2 θ (°)	Int (%)
111	43.3	100
200	50.5	46
220	74.2	20

Lead (#4-686)		
Reflection	2 θ (°)	Int (%)
111	31.3	100
200	36.3	50
220	52.2	31
311	62.1	32
222	65.2	9
400	77.0	2

Cu ₂ O (#5-667)		
Reflection	2 θ (°)	Int (%)
110	29.6	9
111	36.4	100
200	42.3	37
211	52.5	1
220	61.3	27
310	69.6	1
311	73.5	17

Pb ₂ Ti ₂ O ₆ (#26-142)		
Reflection	2 θ (°)	Int (%)
111	14.6	25
311	28.3	50
222	29.6	100
400	34.3	55
331	37.6	40
511	45.2	20
440	49.5	55
531	52.0	20
533	58.1	8
622	58.8	45
444	61.7	14
551	63.9	6
731	69.3	8

PZT 52/48 (#33-784)		
Reflection	2 θ (°)	Int (%)
001	21.4	9
100	22.0	12
101	30.9	100
110	31.4	100
111	38.3	15
002	43.6	9
200	44.9	16
102	49.4	5
201	50.4	6
210	53.4	5
112	54.7	12
211	55.5	24
022	64.4	9
220	65.4	5
003	67.8	2
212	68.9	6
221	69.6	6
103	72.2	6
013	74.0	9

CuO (#41-254)		
Reflection	2 θ (°)	Int (%)
110	32.5	8
002	35.4	60
-111	35.5	100
200	38.9	100
-112	46.3	3
-202	48.7	25
020	53.5	7
202	58.3	12
-113	61.5	16
022	65.8	12
-311	66.3	14
113	67.9	9
220	68.1	14
311	72.4	6
004	75.0	6

FIG 6-1 – Powder Diffraction Cards Used in Phase Identification: *Reproduction of powder diffraction cards showing the reflection, 2 θ value, and relative intensity for various phases investigated in this thesis.*

6.3 Cu-Pb Phase Diagram:

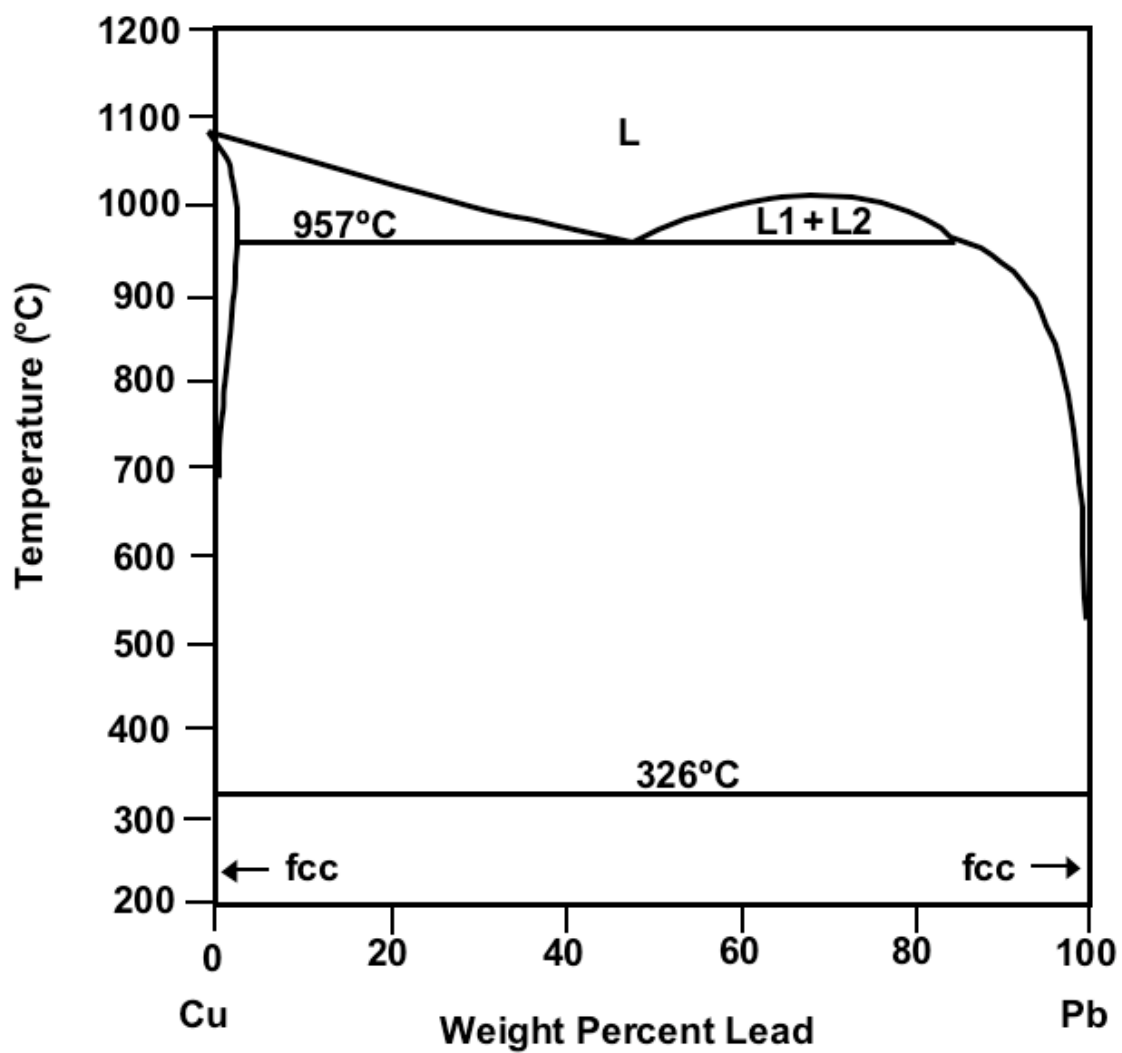


FIG 6-2 – Cu-Pb Binary Phase Diagram: *Binary phase diagram for Pb and Cu from ref: [123].*

7. References

- [1] J. Valasek, "Piezo-electric and allied phenomena in Rochelle salt." *Phys. Rev.* **17** 475 (1921).
- [2] B. Jaffe, W. R. Cook and H. Jaffe, *Piezoelectric Ceramics*. Academic Press, New York (1971).
- [3] G. H. Haertling, "Ferroelectric ceramics: History and technology." *J. Am. Ceram. Soc.* **82** [4] 797 (1999).
- [4] P. R. Coursey and K. G. Brand, "Dielectric constants of some titanates." *Nature*. **157** [3984] 297 (1946).
- [5] S. Miyake and R. Ueda, "On polymorphic change of BaTiO₃." *J. Phys. Soc. Jpn.* **1** [JUL-] 32 (1946).
- [6] B. M. Vul and I. M. Goldman, "Dielectric constants of titanates of the metals of the second group." *Doklady Akademii Nauk SSSR*. **46** 154 (1945).
- [7] E. Wainer, "High titania dielectrics." *T. Electrochem. Soc.* **89** 331 (1946).
- [8] A. von Hippel, R. G. Breckenridge, F. G. Chesley and L. Tisza, "High dielectric constant ceramics." *Ind. Eng. Chem.* **38** [11] 1097 (1946).
- [9] B. M. Vul and I. M. Goldman, "Dielectric constant of barium titanate as a function of strength of an alternating field." *Doklady Akademii Nauk SSSR, Seriya A.* **49** 177 (1945).
- [10] H. D. Megaw, "Crystal structure of barium titanate." *Nature*. **155** [3938] 484 (1945).
- [11] H. P. Rooksby, "Compounds of the structural type of calcium titanate." *Nature*. **155** [3938] 484 (1945).
- [12] B. Jaffe, R. S. Roth and S. Marzullo, "Piezoelectric properties of lead zirconate-lead titanate solid-solution ceramics." *J. Appl. Phys.* **25** [6] 809 (1954).

- [13] A. J. Moulson and J. M. Herbert, *Electroceramics: Materials, Properties, Applications*. Chapman and Hall, New York (1997).
- [14] Y. Xu, *Ferroelectric Materials and Their Applications*. North-Holland, New York (1991).
- [15] J. C. Burfoot and G. W. Taylor, *Polar Dielectrics and Their Applications*. University of California Press, Berkeley (1979).
- [16] D. Damjanovic, "Ferroelectric, dielectric and piezoelectric properties of ferroelectric thin films and ceramics." *Rep. Prog. Phys.* **61** [9] 1267 (1998).
- [17] A. R. West, *Basic Solid State Chemistry*. 2nd ed. John Wiley and Sons, New York (1999).
- [18] D. C. Lupascu, *Fatigue in ferroelectric ceramics and related issues*. Springer, New York (2004).
- [19] J. Nath, D. Ghosh, J.-P. Maria, A. I. Kingon, W. Fathelbab, P. D. Franzon and M. B. Steer, "An electronically-tunable microstrip bandpass filter using thin-film barium strontium titanate (BST) varactors." *IEEE Transactions of Microwave Theory and Technology*. **53** [9] (2005).
- [20] A. K. Tagantsev, V. O. Sherman, K. F. Astafiev, J. Venkatesh and N. Setter, "Ferroelectric materials for microwave tunable applications." *J. Electroceram.* **11** [1-2] 5 (2003).
- [21] R. E. Newnham, *Properties of Materials*. Oxford Press, Oxford (2005).
- [22] E. Sawaguchi, "Ferroelectricity versus antiferroelectricity in the solid solutions of PbZrO_3 and PbTiO_3 ." *J. Phys. Soc. Jpn.* **8** [5] 615 (1953).
- [23] B. Noheda, D. E. Cox, G. Shirane, J. A. Gonzalo, L. E. Cross and S. E. Park, "A monoclinic ferroelectric phase in the $\text{Pb}(\text{Zr}_{1-x}\text{Ti}_x)\text{O}_3$ solid solution." *Appl. Phys. Lett.* **74** [14] 2059 (1999).
- [24] W. R. Buessem, L. E. Cross and A. K. Goswami, "Effect of two-dimensional pressure on the permittivity of fine-and coarse-grained barium titanate." *J. Am. Ceram. Soc.* **49** [1] 36 (1966).

- [25] S. S. Sengupta, S. M. Park, D. A. Payne and L. H. Allen, "Origins and evolution of stress development in sol-gel derived thin layers and multideposited coatings of lead titanate." *J. Appl. Phys.* **83** [4] 2291 (1998).
- [26] J. F. Shepard, Jr., S. Trolier-McKinstry, M. Hendrickson and R. Zeto, "The effects of biaxial stress on the ferroelectric characteristics of PZT thin films." p47 in *Materials for Smart Systems 2*. Materials Research Society Symposium Proceedings **459** (Boston, MA, December 2-5, 1996).
- [27] B. A. Tuttle, J. A. Voigt, T. J. Garino, D. C. Goodnow, R. W. Schwartz, D. L. Lamppa, T. J. Headley and M. O. Eatough, "Chemically prepared $\text{Pb}(\text{Zr},\text{Ti})\text{O}_3$ thin films: The effects of orientation and stress." p344 in *ISAF '92: Proceedings of the Eighth IEEE International Symposium on Applications of Ferroelectrics*. (Greenville, SC, Aug. 30 - Sept. 2, 1992).
- [28] C. K. Kwok and S. B. Desu, "Formation kinetics of $\text{PbZr}_x\text{Ti}_{1-x}\text{O}_3$ thin-films." *J. Mater. Res.* **9** [7] 1728 (1994).
- [29] P. Muralt, T. Maeder, L. Sagalowicz, S. Hiboux, S. Scalese, D. Naumovic, R. G. Agostino, N. Xanthopoulos, H. J. Mathieu, L. Patthey and E. L. Bullock, "Texture control of PbTiO_3 and $\text{Pb}(\text{Zr},\text{Ti})\text{O}_3$ thin films with TiO_2 seeding." *J. Appl. Phys.* **83** [7] 3835 (1998).
- [30] T. Tani, Z. Xu and D. A. Payne, "Preferred orientations for sol-gel derived PLZT thin layers." p269 in *Ferroelectric Thin Films III*. Materials Research Society Symposium Proceedings **310** (San Francisco, CA, April 13-16, 1993).
- [31] G. J. Willems, D. J. Wouters and H. E. Maes, "Influence of the Pt electrode on the properties of sol-gel PZT-films." *Microelectron. Eng.* **29** [1-4] 217 (1995).
- [32] I. M. Reaney, D. V. Taylor and K. G. Brooks, "Ferroelectric PZT thin films by sol-gel deposition." *J. Sol-Gel Sci. Techn.* **13** [1-3] 813 (1998).
- [33] G. R. Bai, I. F. Tsu, A. Wang, C. M. Foster, C. E. Murray and V. P. Dravid, "In situ growth of highly oriented $\text{Pb}(\text{Zr}_{0.5}\text{Ti}_{0.5})\text{O}_3$ thin films by low-temperature metal-organic chemical vapor deposition." *Appl. Phys. Lett.* **72** [13] 1572 (1998).
- [34] B. a. Tuttle, J. a. Voigt, D. C. Goodnow, D. L. Lamppa, T. J. Headley, M. O. Eatough, G. Zender, R. D. Nasby and S. M. Rodgers, "Highly oriented, chemically prepared $\text{Pb}(\text{Zr},\text{Ti})\text{O}_3$ thin-films." *J. Am. Ceram. Soc.* **76** [6] 1537 (1993).

- [35] B. H. Marks, "Ceramic dielectric materials." *Electronics*. **21** [8] 116 (1948).
- [36] M. C. McQuarrie and W. R. Buessem, "Aging effect in barium titanate." *American Ceramic Society Bulletin*. **34** 402 (1955).
- [37] D. Dimos, W. L. Warren and H. N. Al-Shareef, "Degradation mechanisms and reliability issues for ferroelectric thin films." in *Thin Film Ferroelectric Materials and Devices*. R. Ramesh: R. Ramesh. Kluwer, Boston (1997).
- [38] A. K. Tagantsev, I. Stolichnov, E. L. Colla and N. Setter, "Polarization fatigue in ferroelectric films: Basic experimental findings, phenomenological scenarios, and microscopic features." *J. Appl. Phys.* **90** [3] 1387 (2001).
- [39] R. Ramesh, W. K. Chan, B. Wilkens, H. Gilchrist, T. Sands, J. M. Tarascon, V. G. Keramidas, D. K. Fork, J. Lee and a. Safari, "Fatigue and retention in ferroelectric Y-Ba-Cu-O/Pb-Zr-Ti-O/Y-Ba-Cu-O heterostructures." *Appl. Phys. Lett.* **61** [13] 1537 (1992).
- [40] H. N. Al-Shareef, D. Dimos, T. J. Boyle, W. L. Warren and B. A. Tuttle, "Qualitative model for the fatigue-free behavior of SrBi₂Ta₂O₉." *Appl. Phys. Lett.* **68** [5] 690 (1996).
- [41] C. A. P. d. Araujo, J. D. Cuchiaro, L. D. Mcmillan, M. C. Scott and J. F. Scott, "Fatigue-free ferroelectric capacitors with platinum-electrodes." *Nature*. **374** [6523] 627 (1995).
- [42] W. L. Warren, D. Dimos, B. a. Tuttle, G. E. Pike, R. W. Schwartz, P. J. Clews and D. C. McIntyre, "Polarization suppression in Pb(Zr,Ti)O₃ thin-films." *J. Appl. Phys.* **77** [12] 6695 (1995).
- [43] W. L. Warren, B. a. Tuttle and D. Dimos, "Ferroelectric fatigue in perovskite oxides." *Appl. Phys. Lett.* **67** [10] 1426 (1995).
- [44] D. Dimos, W. L. Warren, M. B. Sinclair, B. a. Tuttle and R. W. Schwartz, "Photoinduced hysteresis changes and optical storage in (Pb,La)(Zr,Ti)O₃ thin-films and ceramics." *J. Appl. Phys.* **76** [7] 4305 (1994).
- [45] E. L. Colla, S. B. Hong, D. V. Taylor, A. K. Tagantsev, N. Setter and K. No, "Direct observation of region by region suppression of the switchable polarization (fatigue) in Pb(Zr,Ti)O₃ thin film capacitors with Pt electrodes." *Appl. Phys. Lett.* **72** [21] 2763 (1998).

- [46] E. L. Colla, A. L. Kholkin, D. Taylor, A. K. Tagantsev, K. G. Brooks and N. Setter, "Characterization of the fatigued state of ferroelectric PZT thin-film capacitors." *Microelectron. Eng.* **29** [1-4] 145 (1995).
- [47] E. L. Colla, I. Stolichnov, P. E. Bradely and N. Setter, "Direct observation of inversely polarized frozen nanodomains in fatigued ferroelectric memory capacitors." *Appl. Phys. Lett.* **82** [10] 1604 (2003).
- [48] E. L. Colla, D. V. Taylor, A. K. Tagantsev and N. Setter, "Discrimination between bulk and interface scenarios for the suppression of the switchable polarization (fatigue) in Pb(Zr,Ti)O₃ thin films capacitors with Pt electrodes." *Appl. Phys. Lett.* **72** [19] 2478 (1998).
- [49] A. K. Tagantsev, "Mechanisms of polarization switching in ferroelectric thin films." *Ferroelectrics*. **184** [1-4 Pt. 2] 79 (1996).
- [50] J. M. Herbert, "High permittivity ceramics sintered in hydrogen." *Transactions of the British Ceramic Society*. **62** [8] 645 (1963).
- [51] Y. H. Han, J. B. Appleby and D. M. Smyth, "Calcium as an acceptor impurity in BaTiO₃." *J. Am. Ceram. Soc.* **70** [2] 96 (1987).
- [52] H. Kishi, Y. Mizuno and H. Chazono, "Base-metal electrode-multilayer ceramic capacitors: Past, present and future perspectives." *Jpn. J. Appl. Phys. 1.* **42** [1] 1 (2003).
- [53] Y. Sakabe and T. Reynolds, "Base-metal electrode capacitors." *American Ceramic Society Bulletin*. **81** [10] 24 (2002).
- [54] I. Barin, O. Knacke and O. Kubaschewski, *Thermochemical Properties of Inorganic Substances*. Springer, New York (1973).
- [55] J. T. Dawley and P. G. Clem, "Dielectric properties of random and < 100 > oriented SrTiO₃ and (Ba,Sr)TiO₃ thin films fabricated on < 100 > nickel tapes." *Appl. Phys. Lett.* **81** [16] 3028 (2002).
- [56] J. T. Dawley, R. J. Ong and P. G. Clem, "Chemical solution deposition of < 100 >-oriented SrTiO₃ buffer layers on Ni substrates." *J. Mater. Res.* **17** [7] 1678 (2002).

- [57] J. Ihlefeld, B. Laughlin, A. Hunt-Lowery, W. Borland, A. Kingon and J. P. Maria, "Copper compatible barium titanate thin films for embedded passives." *J. Electroceram.* **14** [2] 95 (2005).
- [58] J. F. Ihlefeld, A. I. Kingon, W. Borland and J.-P. Maria, "Cu-compatible ultra-high permittivity dielectrics for embedded passive components." p145 in *Materials, Integration and Packaging Issues for High-Frequency Devices*. Materials Research Society Proceedings **783** (Boston, MA, December 1-3, 2003).
- [59] B. Laughlin, J. Ihlefeld and J.-P. Maria, "TEM and electrical analysis of sputtered barium strontium titanate (BST) thin films on flexible copper substrates." p301 in *Ferroelectric Thin Films XII*. Materials Research Society Proceedings **784** (Boston, MA, December 1-4, 2003).
- [60] R. J. Ong, J. T. Dawley and P. G. Clem, "Chemical solution deposition of biaxially oriented (Ba,Sr)TiO₃ thin films on < 100 > Ni." *J. Mater. Res.* **18** [10] 2310 (2003).
- [61] G. H. Yi, Z. Wu and M. Sayer, "Preparation of Pb(Zr,Ti)O₃ thin-films by sol-gel processing - Electrical, optical, and electro-optic properties." *J. Appl. Phys.* **64** [5] 2717 (1988).
- [62] G. Yi, M. Sayer, Z. Wu, C. K. Jen and J. F. Bussiere, "Piezoelectric lead zirconate titanate coatings on metallic wires." *Electron. Lett.* **25** [14] 907 (1989).
- [63] J. Y. Chen, Q. C. Xu, M. Blaszkiwicz, R. Meyer and R. E. Newnham, "Lead zirconate titanate films on nickel titanium shape memory alloys - SMARTIES." *J. Am. Ceram. Soc.* **75** [10] 2891 (1992).
- [64] X. P. Liu, C. G. Meng, D. Z. Yang and F. X. Chen, "New synthesis method to improve the properties of PbTiO₃/NiTi composite film." *Materials & Design.* **21** [6] 517 (2000).
- [65] P. G. Mercado and a. P. Jardine, "Smart thin-film TiNi/piezoelectric heterostructures." *J. Vac. Sci. Technol. A.* **13** [3] 1017 (1995).
- [66] H. C. Pan, H. L. Tsai and C. C. Chou, "Low-temperature preparation of PbZrTiO₃/TiNi/Si heterostructures by laser annealing." *Integr. Ferroelectr.* **46** 163 (2002).

- [67] K. Saegusa, "Preparation and electrical properties of sol-gel derived lead zirconate titanate glass-ceramic thin films on metal foil substrates." *Jpn. J. Appl. Phys. I.* **36** [11] 6888 (1997).
- [68] G. Q. Zhang, Q. Zou, P. Sun, X. Mei and H. E. Ruda, "Influence of nitrogen annealing on electrical properties of lead zirconate titanate thin film deposited on titanium metal foil." *Mater. Lett.* **58** [5] 706 (2004).
- [69] Q. Zou, H. E. Ruda and R. N. Sodhi, "TiO_x interlayer characterization for sol-gel derived Pb(Zr, Ti)O₃ thin films on titanium foil." *J. Mater. Sci.-Mater. El.* **13** [10] 601 (2002).
- [70] Q. Zou, H. E. Ruda and B. G. Yacobi, "Improved dielectric properties of lead zirconate titanate thin films deposited on metal foils with LaNiO₃ buffer layers." *Appl. Phys. Lett.* **78** [9] 1282 (2001).
- [71] Q. Zou, H. E. Ruda, B. G. Yacobi, K. Saegusa and M. Farrell, "Dielectric properties of lead zirconate titanate thin films deposited on metal foils." *Appl. Phys. Lett.* **77** [7] 1038 (2000).
- [72] T. Kim, A. I. Kingon, J. P. Maria and R. T. Crosswell, "Ca-doped lead zirconate titanate thin film capacitors on base metal nickel on copper foil." *J. Mater. Res.* **19** [10] 2841 (2004).
- [73] J. P. Maria, K. Cheek, S. Streiffer, S. H. Kim, G. Dunn and A. Kingon, "Lead zirconate titanate thin films on base-metal foils: An approach for embedded high-permittivity passive components." *J. Am. Ceram. Soc.* **84** [10] 2436 (2001).
- [74] J. R. Cheng, W. Y. Zhu, N. Li and L. E. Cross, "Electrical properties of sol-gel-derived Pb(Zr_{0.52}Ti_{0.48})O₃ thin films on a PbTiO₃-coated stainless steel substrate." *Appl. Phys. Lett.* **81** [25] 4805 (2002).
- [75] R. W. Schwartz, "Chemical solution deposition of perovskite thin films." *Chem. Mater.* **9** [11] 2325 (1997).
- [76] B. A. Tuttle and R. W. Schwartz, "Solution deposition of ferroelectric thin films." *MRS Bull.* **21** [6] 49 (1996).
- [77] M. Huffman, "Liquid source misted chemical deposition (LSMCD) - A critical review." *Integr. Ferroelectr.* **10** [1-4] 39 (1995).

- [78] R. W. Schwartz, T. Schneller and R. Waser, "Chemical solution deposition of electronic oxide films." *Cr. Chim.* **7** [5] 433 (2004).
- [79] S. J. Lockwood, R. W. Schwartz, B. A. Tuttle and E. V. Thomas, "Solution chemistry optimization of sol-gel processed PZT thin films." p275 in *Ferroelectric Thin Films III*. Materials Research Society Symposium Proceedings **310** (San Francisco, CA, April 13-16, 1993).
- [80] C. J. Brinker and G. W. Scherer, *Sol-Gel Science: The Physics and Chemistry of Sol-Gel Processing*. Academic Press, New York (1990).
- [81] C. J. Brinker, A. J. Hurd and K. J. Ward, "Fundamentals of sol-gel thin-film formations." p223 in *Ultrastructure Processing of Advanced Ceramics*. Proceedings of the Third International Conference on Ultrastructure Processing of Ceramics, Glasses and Composites (San Diego, CA, February 23-27, 1987).
- [82] R. W. Schwartz, J. A. Voigt, T. J. Boyle, T. A. Christenson and C. D. Buchheit, "Control of thin film processing behavior through precursor structural modifications." *Ceramic Engineering and Science Proceedings*. **16** [5] 1045 (1995).
- [83] T. Schneller and R. Waser, "Chemical solution deposition of ferroelectric thin films - State of the art and recent trends." *Ferroelectrics*. **267** 293 (2002).
- [84] N. Solayappan, L. D. McMillan, C. A. P. DeAraujo and B. Grant, "Second generation liquid source misted chemical deposition (LSMCD) technology for ferroelectric thin films." *Integr. Ferroelectr.* **18** [1-4] 127 (1997).
- [85] M. D. Losego and S. Trolier-McKinstry, "Mist deposition of micron-thick lead zirconate titanate films." p553 in *Ferroelectric Thin Films XII*. Materials Research Society Symposium Proceedings **784** (Boston, MA, December 1-4, 2003).
- [86] L. E. Scriven, "Physics and applications of dip coating and spin coating." p717 in *Better Ceramics Through Chemistry 3*. Materials Research Society Symposium Proceedings **121** (Reno, NV, April 5-8, 1988).
- [87] S. S. Sengupta, L. Ma, D. L. Adler and D. a. Payne, "Extended x-ray-absorption fine-structure determination of local-structure in sol-gel-derived lead titanate, lead zirconate, and lead-zirconate-titanate." *J. Mater. Res.* **10** [6] 1345 (1995).

- [88] C. D. E. Lakeman and D. a. Payne, "Sol-gel processing of electrical and magnetic ceramics." *Mater. Chem. Phys.* **38** [4] 305 (1994).
- [89] D. W. Schaefer and K. D. Keefer, "Fractal aspects of ceramic synthesis." p277 in *Better Ceramics Through Chemistry 2*. Materials Research Society Symposium Proceedings **73** (Palo Alto, CA, April 15-19, 1986).
- [90] B. B. Mandelbrot, *The Fractal Geometry of Nature*. Freeman, San Francisco (1982).
- [91] G. W. Scherer, "Drying mechanics of gels." p225 in *Better Ceramics Through Chemistry 2*. Materials Research Society Symposium Proceedings **73** (Palo Alto, CA, April 15-19, 1986).
- [92] G. W. Scherer, "Physics of drying." p179 in *Ultrastructure Processing of Advanced Materials*. Proceedings of the 4th International Conference on Ultrastructure Processing of Ceramics, Glasses, and Composites (Tucson, AZ, February 20-24, 1989).
- [93] H. Darcy, *Les Fontaines Publiques de la Ville de Dijon*. Libraire des Corps Impériaux des Ponts et Chaussées, Paris (1856).
- [94] G. W. Scherer, "Theory of drying gels." p295 in *Ultrastructure Processing of Advanced Ceramics*. Proceedings of the Third International Conference on Ultrastructure Processing of Ceeramics, Glasses and Composites (San Diego, CA, February 23-27, 1987).
- [95] a. G. Evans, M. D. Drory and M. S. Hu, "The cracking and decohesion of thin-films." *J. Mater. Res.* **3** [5] 1043 (1988).
- [96] P. M. Glaser and C. G. Pantano, "Effect of the H₂O/TEOS ratio upon the preparation and nitridation of silica sol-gel films." *J. Non-Cryst. Solids.* **63** [1-2] 209 (1984).
- [97] P. R. Coffman, C. K. Barlingay, A. Gupta and S. K. Dey, "Structure evolution in the PbO-ZrO₂-TiO₂ sol-gel system: Part II—Pyrolysis of acid and base-catalyzed bulk and thin film gels." *J. Sol-Gel Sci. Techn.* **6** [1] 83 (1996).
- [98] R. W. Schwartz, J. A. Voigt, B. A. Tuttle, D. A. Payne, T. L. Reichert and R. S. DaSalla, "Comments on the effects of solution precursor characteristics and thermal processing conditions on the crystallization behavior of sol-gel derived lead zirconate titanate thin films." *J. Mater. Res.* **12** [2] 444 (1997).

- [99] W. D. Kingery, H. K. Bowen and D. R. Uhlmann, *Introduction to Ceramics*. 2nd ed. John Wiley and Sons, New York (1976).
- [100] J. L. Keddie, P. V. Braun and E. P. Giannelis, "Interrelationship between densification, crystallization, and chemical evolution in sol-gel titania thin-films." *J. Am. Ceram. Soc.* **77** [6] 1592 (1994).
- [101] C. J. Brinker, G. W. Scherer and E. P. Roth, "Sol-gel-glass: II. Physical and structural evolution during constant heating rate experiments." *J. Non-Cryst. Solids.* **72** [2-3] 345 (1985).
- [102] D. R. Uhlmann, L. Klein, P. I. K. Onorato and R. W. Hopper, "The formation of lunar breccias: Sintering and crystallization kinetics." *Geochimica et Cosmochimica Acta, Supplement.* **6** [Proc. Lunar Sci. Conf., 6th, 1975, Vol. 1] 693 (1975).
- [103] R. W. Schwartz, J. A. Voigt, C. D. Buchheit and T. J. Boyle, "Densification and crystallization of zirconia thin films prepared by sol-gel processing." p145 in *Ferroic Materials: Design, Preparation, and Characteristics*. Ceramic Transactions **43** (Honolulu, HI, November 7-12, 1993).
- [104] J. L. Keddie and E. P. Giannelis, "Effect of heating rate on the sintering of titanium-dioxide thin-films - Competition between densification and crystallization." *J. Am. Ceram. Soc.* **74** [10] 2669 (1991).
- [105] J. Fukushima, K. Kodaira and T. Matsushita, "Preparation of ferroelectric PZT films by thermal-decomposition of organometallic compounds." *J. Mater. Sci.* **19** [2] 595 (1984).
- [106] K. D. Budd, S. K. Dey and D. A. Payne, "The effect of hydrolysis conditions on the characteristics of lead titanate gels and thin films." p711 in *Better Ceramics Through Chemistry 2*. Materials Research Society Symposium Proceedings **73** (Palo Alto, CA, April 15-19, 1986).
- [107] a. P. Wilkinson, J. S. Speck, a. K. Cheetham, S. Natarajan and J. M. Thomas, "In-situ x-ray-diffraction study of crystallization kinetics in $\text{PbZr}_{1-x}\text{Ti}_x\text{O}_3$ (PZT, $x=0.0, 0.55, 1.0$)." *Chem. Mater.* **6** [6] 750 (1994).

- [108] M. J. Lefevre, J. S. Speck, R. W. Schwartz, D. Dimos and S. J. Lockwood, "Microstructural development in sol-gel derived lead zirconate titanate thin films: The role of precursor stoichiometry and processing environment." *J. Mater. Res.* **11** [8] 2076 (1996).
- [109] A. Seifert, F. F. Lange and J. S. Speck, "Epitaxial-growth of PbTiO_3 thin-films on (001) SrTiO_3 from solution precursors." *J. Mater. Res.* **10** [3] 680 (1995).
- [110] S. H. Kim, D. J. Kim, J. Hong, S. K. Streiffer and A. I. Kingon, "Imprint and fatigue properties of chemical solution derived $\text{Pb}_{1-x}\text{La}_x(\text{Zr}_y\text{Ti}_{1-y})_{1-x/4}\text{O}_3$ thin films." *J. Mater. Res.* **14** [4] 1371 (1999).
- [111] T. Kim, Ph. D. Thesis. *Lead Zirconate Titanate (PZT) Based Thin Film Capacitors for Embedded Passive Applications*. North Carolina State University, Raleigh (2003).
- [112] L. H. Jimison, J. F. Ihlefeld and J.-P. Maria, Unpublished (2003).
- [113] K. Kitaoka, K. Takahara, H. Kozuka and T. Yoko, "Sol-gel processing of transparent PLZT((Pb,La)(Zr,Ti) O_3) fibers." *J. Sol-Gel Sci. Techn.* **16** [1-2] 183 (1999).
- [114] K. Kato, "Low-temperature synthesis of $\text{SrBi}_2\text{Ta}_2\text{O}_9$ ferroelectric thin films through the complex alkoxide method: Effects of functional group, hydrolysis and water vapor treatment." *Jpn. J. Appl. Phys. I.* **37** [9B] 5178 (1998).
- [115] H. Suzuki, M. B. Othman, K. Murakami, S. Kaneko and T. Hayashi, "Low-temperature processing of ferroelectric $\text{Pb}(\text{Zr}_{0.53}\text{Ti}_{0.47})\text{O}_3$ thin film from molecular-designed alkoxide precursor solution." *Jpn. J. Appl. Phys. I.* **35** [9B] 4896 (1996).
- [116] R. W. Schwartz, R. A. Assink, D. Dimos, M. B. Sinclair, T. J. Boyle and C. D. Buchheit, "Effects of acetylacetone additions on PZT thin film processing." p377 in *Ferroelectric Thin Films IV*. Materials Research Society Symposium Proceedings **361** (Boston, MA, Nov. 29-Dec. 2, 1994).
- [117] R. A. Assink and R. W. Schwartz, " ^1H and ^{13}C NMR investigations of $\text{Pb}(\text{Zr,Ti})\text{O}_3$ thin-film precursor solutions." *Chem. Mater.* **5** [4] 511 (1993).
- [118] R. W. Schwartz, B. C. Bunker, D. B. Dimos, R. A. Assink, B. A. Tuttle, D. R. Tallant and I. A. Weinstock, "Solution chemistry effects in lead zirconate titanate thin-film processing." *Integr. Ferroelectr.* **2** [1-4] 243 (1992).

- [119] R. W. Schwartz, R. A. Assink and T. J. Headley, "Spectroscopic and microstructural characterization of solution chemistry effects in PZT thin film processing." p245 in *Ferroelectric Thin Films II*. Materials Research Society Symposium Proceedings **243** (Boston, MA, December 2-4, 1991).
- [120] T. J. Boyle, D. Dimos, R. W. Schwartz, T. M. Alam, M. B. Sinclair and C. D. Buchheit, "Aging characteristics of a hybrid sol-gel $\text{Pb}(\text{Zr},\text{Ti})\text{O}_3$ precursor solution." *J. Mater. Res.* **12** [4] 1022 (1997).
- [121] D. Dimos, R. W. Schwartz and S. J. Lockwood, "Control of leakage resistance in $\text{Pb}(\text{Zr},\text{Ti})\text{O}_3$ thin-films by donor doping." *J. Am. Ceram. Soc.* **77** [11] 3000 (1994).
- [122] M. D. Losego, L. H. Jimison, J. F. Ihlefeld and J.-P. Maria, "Ferroelectric response from lead zirconate titanate thin films prepared directly on low-resistivity copper substrates." *Appl. Phys. Lett.* **86** [17] 172906 (2005).
- [123] F. H. Hayes, H. L. Lukas, G. Effenberg and G. Petzow, "A thermodynamic optimization of the Cu-Ag-Pb system." *Z. Metallkd.* **77** [11] 749 (1986).